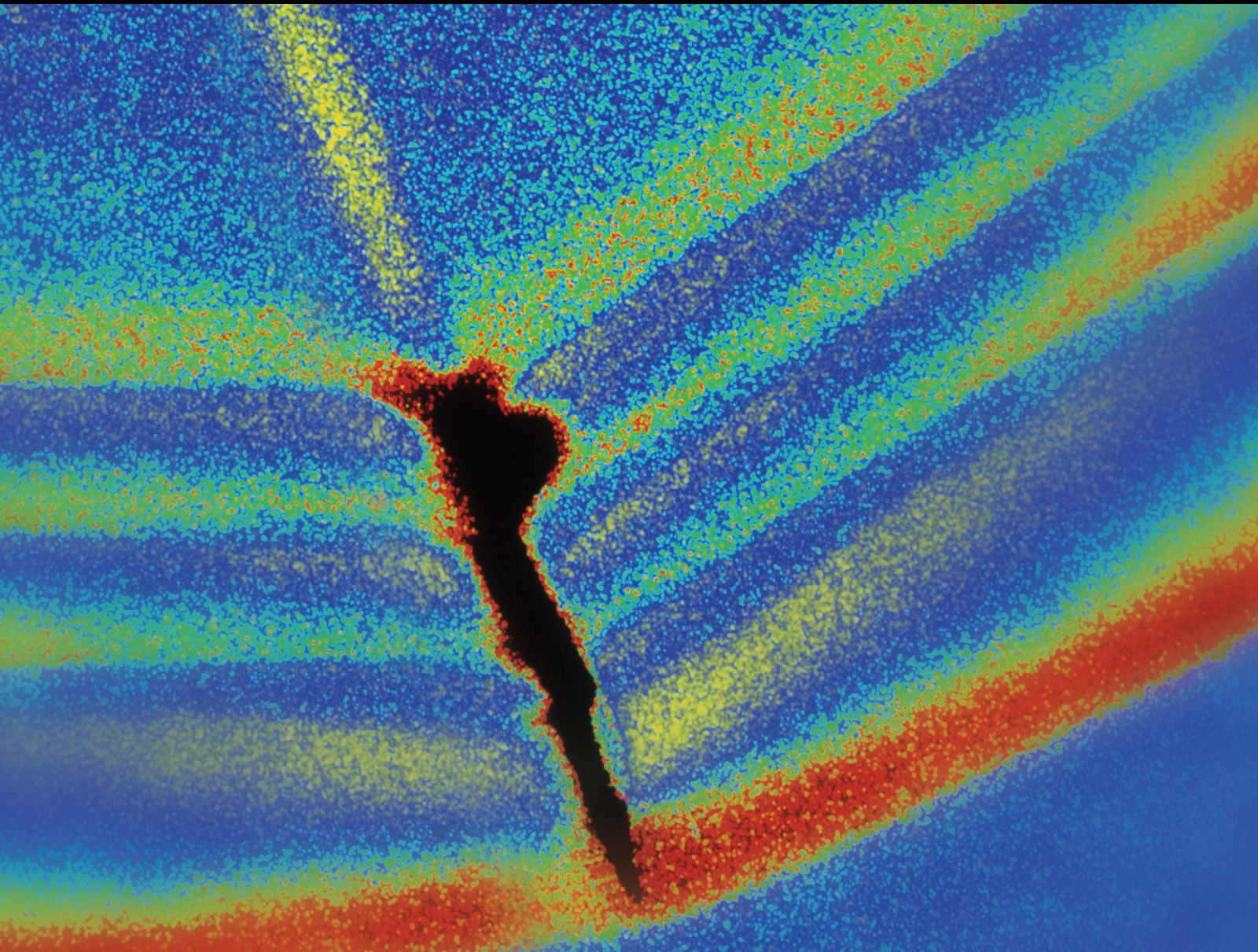


Performance-Based Shock and Vibration Engineering of Infrastructures 2021

Lead Guest Editor: S. Mahdi S. Kolbadi

Guest Editors: Angelo Marcelo Tuset, Wahyu Caesarendra, and Kim Hung Mo





**Performance-Based Shock and Vibration
Engineering of Infrastructures 2021**

Shock and Vibration

**Performance-Based Shock
and Vibration Engineering of
Infrastructures 2021**

Lead Guest Editor: S. Mahdi S. Kolbadi

Guest Editors: Angelo Marcelo Tuset, Wahyu
Caesarendra, and Kim Hung Mo



Copyright © 2021 Hindawi Limited. All rights reserved.

This is a special issue published in “Shock and Vibration.” All articles are open access articles distributed under the Creative Commons Attribution License, which permits unrestricted use, distribution, and reproduction in any medium, provided the original work is properly cited.

Chief Editor

Huu-Tai Thai , Australia


Associate Editors

Ivo Calìo , Italy
Nawawi Chouw , New Zealand
Longjun Dong , China
Farzad Ebrahimi , Iran
Mickaël Lallart , France
Vadim V. Silberschmidt , United Kingdom
Mario Terzo , Italy
Angelo Marcelo Tusset , Brazil

Academic Editors

Omid A. Yamini , Iran
Maher Abdelghani, Tunisia
Haim Abramovich , Israel
Desmond Adair , Kazakhstan
Manuel Aenlle Lopez , Spain
Brij N. Agrawal, USA
Ehsan Ahmadi, United Kingdom
Felix Albu , Romania
Marco Alfano, Italy
Sara Amoroso, Italy
Huaming An, China
P. Antonaci , Italy
José V. Araújo dos Santos , Portugal
Lutz Auersch , Germany
Matteo Aureli , USA
Azwan I. Azmi , Malaysia
Antonio Batista , Brazil
Mattia Battarra, Italy
Marco Belloli, Italy
Francisco Beltran-Carbajal , Mexico
Denis Benasciutti, Italy
Marta Berardengo , Italy
Sébastien Besset, France
Giosuè Boscato , Italy
Fabio Botta , Italy
Giuseppe Brandonisio , Italy
Francesco Bucchi , Italy
Rafał Burdzik , Poland
Salvatore Caddemi , Italy
Wahyu Caesarendra , Brunei Darussalam
Baoping Cai, China
Sandro Carbonari , Italy
Cristina Castejón , Spain

Nicola Caterino , Italy
Gabriele Cazzulani , Italy
Athanasios Chasalevris , Greece
Guoda Chen , China
Xavier Chimentin , France
Simone Cinquemani , Italy
Marco Civera , Italy
Marco Cocconcelli , Italy
Alvaro Cunha , Portugal
Giorgio Dalpiaz , Italy
Thanh-Phong Dao , Vietnam
Arka Jyoti Das , India
Raj Das, Australia
Silvio L.T. De Souza , Brazil
Xiaowei Deng , Hong Kong
Dario Di Maio , The Netherlands
Raffaella Di Sante , Italy
Luigi Di Sarno, Italy
Enrique Lopez Droguett , Chile
Mădălina Dumitriu, Romania
Sami El-Borgi , Qatar
Mohammad Elahinia , USA
Said Elias , Iceland
Selçuk Erkaya , Turkey
Gaoliang Fang , Canada
Fiorenzo A. Fazzolari , United Kingdom
Luis A. Felipe-Sese , Spain
Matteo Filippi , Italy
Piotr Fołga , Poland
Paola Forte , Italy
Francesco Franco , Italy
Juan C. G. Prada , Spain
Roman Gabl , United Kingdom
Pedro Galvín , Spain
Jinqiang Gan , China
Cong Gao , China
Arturo García García-Perez, Mexico
Rozaimi Ghazali , Malaysia
Marco Gherlone , Italy
Anindya Ghoshal , USA
Gilbert R. Gillich , Romania
Antonio Giuffrida , Italy
Annalisa Greco , Italy
Jiajie Guo, China

Amal Hajjaj , United Kingdom
Mohammad A. Hariri-Ardebili , USA
Seyed M. Hashemi , Canada
Xue-qiu He, China
Agustin Herrera-May , Mexico
M.I. Herreros , Spain
Duc-Duy Ho , Vietnam
Hamid Hosano , Japan
Jin Huang , China
Ahmed Ibrahim , USA
Bernard W. Ikuu, Kenya
Xingxing Jiang , China
Jiang Jin , China
Xiaohang Jin, China
MOUSTAFA KASSEM , Malaysia
Shao-Bo Kang , China
Yuri S. Karinski , Israel
Andrzej Katunin , Poland
Manoj Khandelwal, Australia
Denise-Penelope Kontoni , Greece
Mohammadreza Koopialipour, Iran
Georges Kouroussis , Belgium
Genadijus Kulvietis, Lithuania
Pradeep Kundu , USA
Luca Landi , Italy
Moon G. Lee , Republic of Korea
Trupti Ranjan Lenka , India
Arcanjo Lenzi, Brazil
Marco Lepidi , Italy
Jinhua Li , China
Shuang Li , China
Zhixiong Li , China
Xihui Liang , Canada
Tzu-Kang Lin , Taiwan
Jinxin Liu , China
Ruonan Liu, China
Xiuquan Liu, China
Siliang Lu, China
Yixiang Lu , China
R. Luo , China
Tianshou Ma , China
Nuno M. Maia , Portugal
Abdollah Malekjafarian , Ireland
Stefano Manzoni , Italy

Stefano Marchesiello , Italy
Francesco S. Marulo, Italy
Traian Mazilu , Romania
Vittorio Memmolo , Italy
Jean-Mathieu Mencik , France
Laurent Mevel , France
Letícia Fleck Fadel Miguel , Brazil
FuRen Ming , China
Fabio Minghini , Italy
Marco Miniaci , USA
Mahdi Mohammadpour , United Kingdom
Rui Moreira , Portugal
Emiliano Mucchi , Italy
Peter Múčka , Slovakia
Fehmi Najar, Tunisia
M. Z. Naser, USA
Amr A. Nassr, Egypt
Sundararajan Natarajan , India
Toshiaki Natsuki, Japan
Miguel Neves , Portugal
Sy Dzung Nguyen , Republic of Korea
Trung Nguyen-Thoi , Vietnam
Gianni Niccolini, Italy
Rodrigo Nicoletti , Brazil
Bin Niu , China
Leilei Niu, China
Yan Niu , China
Lucio Olivares, Italy
Erkan Oterkus, United Kingdom
Roberto Palma , Spain
Junhong Park , Republic of Korea
Francesco Pellicano , Italy
Paolo Pennacchi , Italy
Giuseppe Petrone , Italy
Evgeny Petrov, United Kingdom
Franck Poisson , France
Luca Pugi , Italy
Yi Qin , China
Virginio Quaglini , Italy
Mohammad Rafiee , Canada
Carlo Rainieri , Italy
Vasudevan Rajamohan , India
Ricardo A. Ramirez-Mendoza , Mexico
José J. Rangel-Magdaleno , Mexico

Didier Rémond , France
Dario Richiedi , Italy
Fabio Rizzo, Italy
Carlo Rosso , Italy
Riccardo Rubini , Italy
Salvatore Russo , Italy
Giuseppe Ruta , Italy
Edoardo Sabbioni , Italy
Pouyan Roodgar Saffari , Iran
Filippo Santucci de Magistris , Italy
Fabrizio Scozzese , Italy
Abdullah Seçgin, Turkey
Roger Serra , France
S. Mahdi Seyed-Kolbadi, Iran
Yujie Shen, China
Bao-Jun Shi , China
Chengzhi Shi , USA
Gerardo Silva-Navarro , Mexico
Marcos Silveira , Brazil
Kumar V. Singh , USA
Jean-Jacques Sinou , France
Isabelle Sochet , France
Alba Sofi , Italy
Jussi Sopanen , Finland
Stefano Sorace , Italy
Andrea Spaggiari , Italy
Lei Su , China
Shuaishuai Sun , Australia
Fidelis Tawiah Suorineni , Kazakhstan
Cecilia Surace , Italy
Tomasz Szolc, Poland
Iacopo Tamellini , Italy
Zhuhua Tan, China
Gang Tang , China
Chao Tao, China
Tianyou Tao, China
Marco Tarabini , Italy
Hamid Toopchi-Nezhad , Iran
Carlo Trigona, Italy
Federica Tubino , Italy
Nerio Tullini , Italy
Nicolò Vaiana , Italy
Marcello Vanali , Italy
Christian Vanhille , Spain




Dr. Govind Vashishtha, Poland
F. Viadero, Spain
M. Ahmer Wadee , United Kingdom
C. M. Wang , Australia
Gaoxin Wang , China
Huiqi Wang , China
Pengfei Wang , China
Weiqiang Wang, Australia
Xian-Bo Wang, China
YuRen Wang , China
Wai-on Wong , Hong Kong
Yuanping XU , China
Biao Xiang, China
Qilong Xue , China
Xin Xue , China
Diansen Yang , China
Jie Yang , Australia
Chang-Ping Yi , Sweden
Nicolo Zampieri , Italy
Chao-Ping Zang , China
Enrico Zappino , Italy
Guo-Qing Zhang , China
Shaojian Zhang , China
Yongfang Zhang , China
Yaobing Zhao , China
Zhipeng Zhao, Japan
Changjie Zheng , China
Chuanbo Zhou , China
Hongwei Zhou, China
Hongyuan Zhou , China
Jiaxi Zhou , China
Yunlai Zhou, China
Radoslaw Zimroz , Poland

Contents

Hydrodynamic Performance of A-Jacks Concrete Armor Units in Riverbeds around Downstream in Flip Buckets

Kamran Khalifehei , Gholamreza Azizyan, and Mahmood Shafai-Bajestan
Research Article (10 pages), Article ID 4497086, Volume 2021 (2021)


Experimental Investigation on the Ductility of Concrete Deep Beams Reinforced with Basalt-Carbon and Basalt-Steel Wire Hybrid Composite Bars

Mohammadamin Mirdarsoltany , Alireza Rahai , and Farzad Hatami 
Research Article (8 pages), Article ID 6866993, Volume 2021 (2021)



Free and Forced Vibration Characteristics Analysis of a Multispan Timoshenko Beam Based on the Ritz Method

Cong Gao, Fuzhen Pang, Haichao Li , Hongfu Wang, Jie Cui, and Jisi Huang
Research Article (18 pages), Article ID 4440250, Volume 2021 (2021)




Investigating the Effect of Viscous Yield Dampers on Concrete Structure Performance

Nima Marzban  and Parisa Esmailtabar Nesheli
Research Article (6 pages), Article ID 8489333, Volume 2021 (2021)

Performance Evaluation of CFRP Strengthened Corrosion-Proof Columns

Mohammadamin Mirdarsoltany , Alireza Rahai , and Mohammad Zaman Kabir
Research Article (14 pages), Article ID 8390088, Volume 2021 (2021)

Groundwater Single- and Multiobjective Optimization Using Harris Hawks and Multiobjective Billiards-Inspired Algorithm

AbdolGhafour Gerey , Amirpouya Sarraf , and Hassan Ahmadi 
Research Article (16 pages), Article ID 4531212, Volume 2021 (2021)

Research Article

Hydrodynamic Performance of A-Jacks Concrete Armor Units in Riverbeds around Downstream in Flip Buckets

Kamran Khalifehei ¹, Gholamreza Azizyan,¹ and Mahmood Shafai-Bajestan²

¹Department of Civil Engineering, University of Sistan and Baluchestan, Zahedan 987-98155, Iran

²Department of Hydraulic Structures, Faculty of Water Science Engineering, Shahid Chamran University of Ahvaz, Ahwaz, Iran

Correspondence should be addressed to Kamran Khalifehei; kamran.khalifehei@pgs.usb.ac.ir

Received 3 July 2021; Revised 28 July 2021; Accepted 5 August 2021; Published 12 August 2021

Academic Editor: S. Mahdi S. Kolbadi

Copyright © 2021 Kamran Khalifehei et al. This is an open access article distributed under the Creative Commons Attribution License, which permits unrestricted use, distribution, and reproduction in any medium, provided the original work is properly cited.

The jet flipped from flip buckets hits the dam's downstream side as a free jet with an immense amount of energy, leading to bed erosion. Erosion of river bed materials downstream of dams could affect the performance of dams or power plants by altering the tailwater depth, rendering proper designs of controlling structures or erosion reduction methods highly indispensable in this regard. Hence, the hydrodynamic performance of A-Jacks concrete armor units in controlling scour was examined in this study. A-Jacks armors are applicable as a flexible protection without environmental risks often for bed erosion control. The desirable functionality of A-Jacks armors depends on the flow hydrodynamic parameters such as velocity profile variations (U/U_B), the Reynolds stresses ($\tau_{u'w'}$ and $\tau_{v'w'}$), and the skin friction coefficient (C_f) created as a consequence of using A-Jacks armors on beds. The size of A-Jacks elements can have a role in increasing the flow turbulence to a certain depth so that after the impact of the flow with A-Jacks armor, the vortices' intensity as well as the shear stress affecting the bed gradually decreases. The results of the numerical model suggest that the surge in the flow turbulence energy dissipation downstream of flip buckets significantly mitigates the underlying conditions of scouring phenomena, which is evidence of A-Jacks armors' acceptable performance in scaling down scour depths.

1. Introduction

Use of A-Jacks concrete armor units represents one of the simplest and most practical systems protecting erodible beds. These six-legged elements are designed to create a solid material when the legs are interlocked. Hence, lighter elements than riprap are required. On the other hand, the ridges in piers and roughness formation cause the inlet jet flow to break down into smaller jets, and more importantly, the roughness leads to an increase in the shear force and energy dissipation. Furthermore, a part of the original jet infiltrates the elements and the bed, and it is likely to develop bed scour. Therefore, the number of layers placed on top of each other has an effect on scour depth as well [1]. A blend of A-Jacks armors and riprap could help reduce the scour dimensions. In such an occasion, the armors and the riprap will be smaller in size and also more convenient and

economic to implement. Figure 1 illustrates the design of A-Jacks armors and their use in river engineering and hydraulic engineering.

A-Jacks armors have been incorporated in marine structures such as breakwaters and coast protections. In addition to the extensive applications of these elements in marine structures, their use in controlling river bank erosions has also attracted much attention recently [2]. A review of the available resources indicates that only a highly limited number of studies have addressed A-Jacks armors from structural and hydraulic points of view in general. The hydraulic studies available on A-Jacks elements are very limited and related to protecting sea coasts, piers, and bridge abutments. One of the most important studies investigating, from the structural viewpoint, the elements' buckling under vertical static loads was carried out by Mickel [3].

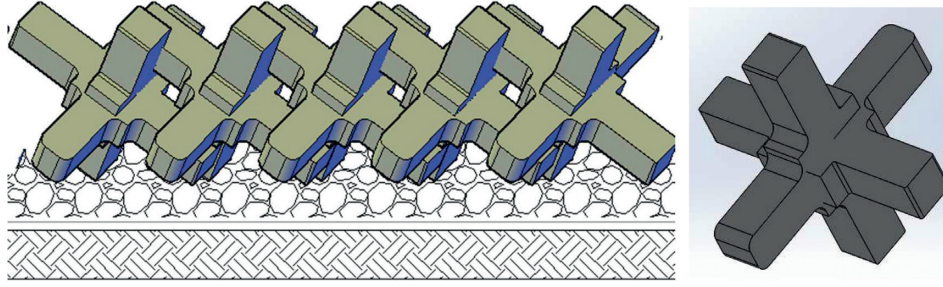


FIGURE 1: .Geometric shape of six-legged elements and an instance of A-Jacks armors' interlock.

Latta [4] also conducted other studies on six-legged concrete elements in hydraulic structures, and these studies include physical and numerical simulations of the elements, and analysis of the applied forces as well as the elements' stability.

As for the other hydrodynamic studies on A-Jacks armors, the two-step report put forth by the Soil and Water Conservation Bureau of the United States at Manly Hydraulics Laboratory could be stated as a study carried out with the purpose of comparing and assessing six-legged components against different breakwater components experimentally and modifying those designs [1]. In the experiments conducted by Thornton et al. on bridge pier scour hole control on a sand bed using A-Jacks armors, the decrease in the scour depth values after using these elements has been reported to be 70 to 95%, and for gaining more efficiency from these elements, use of geotextile filters with them has been recommended [2]. Zolghadr et al. demonstrated that installation of A-Jacks armors could control scouring at the trapezoidal crest up to 100%. Extensive research has been undertaken in Shahid Chamran University in order to examine application of six-legged elements for protecting the stilling basins' bed, indicating that a proper arrangement of these elements could reduce the stilling basin at length and the conjugate depth as well as scour depth downstream of the basins [5, 6]. Hosein Reza et al. applied the combined method of utilizing both riprap and six-legged elements as direct methods of controlling scour at a rectangular abutment. As reported in the results of their tests, the combined implementation of riprap and six-legged elements had a significant effect [7]. Khalifehei et al. investigated A-Jack armors' stability on the erodible bed downstream of flip buckets and proposed a design for these armors [8, 9].

In their studies, Nou et al. examined the efficiency of six-legged concrete elements in controlling scour downstream of flip bucket spillways by conducting experimental studies. Their work addresses sediment scour hole volume reduction with simultaneous presence of six-legged concrete elements, under the brand of A-Jack, and riprap downstream of a flip bucket spillway under different hydraulic conditions of the flow. The results suggest that an increase in the tailwater depth significantly mitigated scouring, and the simultaneous presence of the concrete element and riprap could cause up to 100% drop in the maximum scour volume among various

hydraulic conditions in comparison with that in the control test [10, 11].

A-Jacks advantages, such as their interlocking capability, their applicability in regions lacking appropriate rocks, and the possibility of vegetation's growing between the units, can help the armor's stability under certain conditions. On the other hand, the present study is deemed necessary as there have been no works available investigating the flow hydrodynamic parameters on these armors using numerical methods so far. Accordingly, this study embarks on simulation of A-Jacks armors implemented downstream of flip bucket spillways as a method of scouring control as a new and widely applicable topic in hydraulic engineering.

2. Theoretical Approach

The Flow3D model is applicable for analyzing unsteady 3D flows with a free surface and a complex geometry. The finite volume method is used in this numerical model in an orderly rectangular cell grid. Two methods have been used in this numerical model for geometric simulation. The first method is Volume of Fluid (VOF), which is incorporated to demonstrate the fluid behavior at the free surface. The second method is called Fractional Area/Volume Obstacle Representation (FAVOR), which is applied for simulation of surfaces and rigid volumes such as geometric boundaries [12–14].

The equations governing the fluid flow are extracted from the principles of mass conservation and momentum conservation and are represented as partial differential equations. The main equations for simulating the three-dimensional flow are three differential equations including the continuity and momentum equations in x , y , and z directions. The flow continuity equation is extracted from the principle of mass conservation and by writing the balance relation for a fluid element. The general continuity equation is presented as follows:

$$V_f \frac{\partial \rho}{\partial t} + \frac{\partial}{\partial x} (\rho u A_x) + \frac{\partial}{\partial y} (\rho v A_y) + \frac{\partial}{\partial z} (\rho w A_z) = 0, \quad (1)$$

where V_f is the fraction of volume to flow and ρ is the fluid density. Velocity components (u, v, w) are in x , y , and z directions. A_x is the fraction of free surface in x direction, and A_y and A_z are similarly fractions of surface in y and z directions.

The fluid's motion equations with velocity components (u, v, w) in three directions in coordinates, i.e., the Navier–Stokes equations, are presented as follows:

$$\begin{aligned} \frac{\partial u}{\partial t} + \frac{1}{V_F} \left(uA_x \frac{\partial u}{\partial x} + vA_y \frac{\partial u}{\partial y} + wA_z \frac{\partial u}{\partial z} \right) &= -\frac{1}{\rho} \frac{\partial p}{\partial x}, \\ \frac{\partial v}{\partial t} + \frac{1}{V_F} \left(uA_x \frac{\partial v}{\partial x} + vA_y \frac{\partial v}{\partial y} + wA_z \frac{\partial v}{\partial z} \right) &= -\frac{1}{\rho} \frac{\partial p}{\partial y}, \\ \frac{\partial w}{\partial t} + \frac{1}{V_F} \left(uA_x \frac{\partial w}{\partial x} + vA_y \frac{\partial w}{\partial y} + wA_z \frac{\partial w}{\partial z} \right) &= -\frac{1}{\rho} \frac{\partial p}{\partial z}, \end{aligned} \quad (2)$$

where $G_x, G_y,$ and G_z denote mass accelerations and $f_x, f_y,$ and f_z are viscosity accelerations.

The Flow3D numerical model is used for simulating transport, erosion, deposition, and static position of the nonadhesive sediments under the influence of the fluid flow. The sediment model of this numerical model uses two concentration fields: (1) floating nonadhesive sediments and (2) bed nonadhesive sediments.

Displacement and lifting of floating sediments with the fluid occur due to variations in the local pressure gradient. These floating nonadhesive sediments could be a result of the inlet flow containing floating particles or stem from bed erosion. Since bed sediments are restricted by the adjacent particles and cannot move easily, they can get in motion if they are converted into floating load as eroded particles at the interface between the bed and the fluid, and the floating load can convert into bed load in case the deposition velocity is higher than the bed erosion velocity [15, 16]. A part of the control volume, occupied by solid sediment particles, is denoted by f_s , and the rest made of accumulated fluid is defined by f_L ; therefore,

$$f_s + f_L = 1. \quad (3)$$

The floating load increases the real fluid viscosity. Such an increase lasts until the volume fraction of the solid particles reaches the limit of the volume fraction of viscosity. After that the increase in the floating load does not cause a higher viscosity but results in the particle's growing active in a solid manner. In this case, the average fluid viscosity is obtained as follows:

$$\mu^* = \mu_f \left(1 - \frac{\text{Min}(f_s, f_{sco})}{f_{sCR}} \right), \quad (4)$$

where μ_f represents the fluid viscosity and μ^* is the average viscosity of the critical fraction of nonadhesive sediments particles. The perceived density, $\bar{\rho}$, is assumed as a linear function of the sediments volume, where ρ_s and ρ_L are the apparent densities of the sediment and the fluid [17].

Drift is defined as sediment particles deposition under the influence of the drift forces affecting the sediment particle. In the sediment washing model in the Flow3D numerical model, the sediment particles are assumed spherical so that they are influenced by the fluid viscosity; hence, deposition is automatically calculated according to the following relation:

$$D_f = \frac{d_{50}^2 \times (\rho_s - \rho_L)}{18\mu}. \quad (5)$$

Therefore, the deposition velocity is obtained as follows:

$$\begin{aligned} u_{\text{drift}} &= D_f \times f_L \frac{\nabla P}{\bar{\rho}} \\ &= \frac{f_L \times d_{50}^2}{18\mu} \frac{\nabla P}{\bar{\rho}} (\rho_s - \rho_L), \end{aligned} \quad (6)$$

where $\nabla P/\bar{\rho}$ is defined as the gradient of mechanical potential or acceleration and is limited to 10 times the particle's weight, leading to elimination of numerical fluctuations in the amount of pressure. Near the fluid free surface, the value of $\nabla P/\bar{\rho}$ is replaced by g . The f_L coefficient is included in equation (6) because sedimentation is possible only with the presence of solid particles (sediment) [18, 19]. Therefore, if the control volume is filled with sediment, then $f_L = 0$ and thus $u_{\text{drift}} = 0$. The shear stress is active at the bed sediment level, which leads to erosion and displacement of nonadhesive sediments at bed surface. This erosion is a function of the fluid shear stress at surface, the critical shear stress, and the fluid and sediment densities. The critical Shields parameter represents the minimum shear stress required for lifting sediment particles from the interface between the fluid and the active bed.

$$\theta_{\text{cirt}} = \frac{\tau_{\text{crit}}}{g(\rho_L - \rho_s)d'}, \quad (7)$$

where θ_{cirt} is the critical Shields parameter and τ_{crit} denotes the minimum shear stress required along the bed to lift sediment particles. Elaborating on and describing this model is aimed to estimate and predict the amount of sediment flow eroded over the shared bed. To this end, the shear velocity parameter is defined for measuring the flow power in bed erosion [20, 21]. Hence, the rate of sediment lift from the bed could be presented as follows:

$$U_{\text{lift}} = \alpha n_s \sqrt{\frac{\tau - \tau_{\text{crit}}}{\bar{\rho}}}, \quad (8)$$

where n_s is the bed surface normal vector and α represents the dimensionless parameter which shows the possibility of sediment particles' being lifted from the bed, which is usually less than or equal to unity. In a static fluid, the internal friction angle of sediment particles determines the minimum slope at which sediment walls can be stable. A high internal friction angle of sediments, as in clay, implies stability of the wall at sharp slopes, and a low internal friction angle, as in sand, demonstrates a high inclination for slump and forward motion. At the downstream side of the hole, where sediments are piled up and make a bulk of sediments, the state of sediment position creates a horizontal angle which represents the internal friction angle. In the model, ξ denotes this angle. The natural angle of repose for sediments under different spatial and temporal conditions is calculated as follows:

$$\phi = \frac{n_{\text{interface}} \cdot g}{|g|}, \quad (9)$$

where $n_{\text{interface}}$ is equal to the surface normal vector and g is the acceleration of gravity. The critical shear stress which occurs at the sloped surface is calculated according to the following equation for each surface after the occurrence of scour or floating sediment transport at that surface:

$$\tau_{\text{crit}} = \tau_{\text{crit}}^0 \sqrt{1 - \frac{\sin^2 \phi}{\sin^2 \zeta}}. \quad (10)$$

Based on equation (10), when the natural slope of the sediment is equal to its internal friction angle ($\phi = \zeta$), the critical shear stress will be equal to zero, i.e., the bed surface undergoes erosion owing to any type of shear stress applied. In addition, when $\phi > \zeta$, then $\tau_{\text{crit}} < 0$, i.e., the sediments undergo erosion even when there is no shear stress. The above relation also indicates that as large as the sediment particles' internal friction angle becomes, the wall slope ($\tau_{\text{crit}} = 0$) must also grow large so that the scour or flushing hole wall undergoes erosion without the presence of shear stress (ϕ). Transport of the sediment floating in the system is stated by the convection-diffusion equation [22, 23].

$$U_j \frac{\partial c_s}{\partial x_j} - \omega_s \left(\frac{\partial c_s}{\partial z} \right) = \frac{\partial}{\partial x_j} \left(\Gamma \frac{\partial c_s}{\partial x_j} \right), \quad (11)$$

where c_s is the sediment concentration, Γ denotes the diffusion coefficient, and ω_s is the particles settling velocity as follows:

$$\omega_s = u_{\text{lift}} - u_{\text{drift}}. \quad (12)$$

As a result, equation (12) enters the solution according to the following:

$$\frac{\partial c_s}{\partial t} + u \cdot \nabla c_s = \Gamma \nabla^2 c_s - u_{\text{lift}} \cdot \nabla c_s - u_{\text{drift}} \cdot \nabla c_s. \quad (13)$$

The concentration of the floating sediment at the interface between nonadhesive sediments bed and water prior to the onset of flushing ($t = 0$) is obtained as follows:

$$C_{s0} = f_s * \rho. \quad (14)$$

The above relations and computational algorithm are used in the Flow3D numerical model in order to drain bed sediments. In the following numerical model, the flow hydrodynamic parameters will be addressed using the proposed theoretical approach. For geometric simulation, two strategies were applied in this numerical model. Volume of Fluid (VOF) is the initial method, which is used to demonstrate fluid dynamics at the free surface. The second method, known as FAVOR (Fractional Area/Volume Obstacle Representation), is used to simulate surfaces and rigid volumes such as geometric bounds.

3. Research Method

In every simulation carried out in this study, the 3D flow field has been solved using the RNG turbulence model. The

RNG model was developed using Renormalisation Group (RNG) methods by Yakhot et al. to renormalise the Navier–Stokes equations, to account for the effects of smaller scales of motion. In the standard k-epsilon model, the eddy viscosity is determined from a single turbulence length scale, so the calculated turbulent diffusion is that which occurs only at the specified scale, whereas in reality, all scales of motion will contribute to the turbulent diffusion. The RNG approach, which is a mathematical technique that can be used to derive a turbulence model similar to the k-epsilon, results in a modified form of the epsilon equation which attempts to account for the different scales of motion through changes to the production term [24, 25]. The reason for using this turbulence model can be attributed to its properties and advantages over models such as $k - \epsilon$. This model has been improved due to having one ϵ extra term for analyzing quickly strained flows and the flows over surfaces with numerous geometric variations and is greatly capable in transient flow simulations [26]. In addition, relying on the comparison made between turbulence models over spillways using Flow3D conducted by Yamini (2018), the RNG turbulence model has had more accurate results than other turbulence models, and it has therefore been used in the present work [27, 28]. In this simulation, the flow over ogee spillways was modeled using real model data, and it was analytically solved. In addition, the fluid, nonviscous and incompressible, and the air inlet with a density of 1.24 kg/m^3 and a shear stress rate of 0.0731 were taken into consideration.

It is noteworthy that there are 898,287 computational cells considered for this simulation. Different boundary conditions have been assumed per the most appropriate channel length behind the spill way as 1 meter long water prior to the ogee spillway and inside the dam reservoir. As for the size, the elements utilized in the study are categorized into six classes named A-Jacks 1 to A-Jacks 6, and A-Jacks 1 size is provided in Figure 2. The other elements have also been designed and considered in order with 20% larger dimensions. Further, the boundary conditions of the flow simulation over ogee spillways are defined in Figure 2. Different conditions have been considered to apply boundary conditions to the mesh block (Figure 2). As for the inflow, the flow rate is applied along with the flow depth (Q). Outflow conditions (O) are considered in terms of output. The wall boundary condition (W) is applied to the lateral walls. The boundary condition of the wall (W) is applied on the bottom of the mesh block, and the boundary condition of symmetry (S) is considered on the roof of the mesh block. grid as wall and symmetry, the bed and top for computational cells as, respectively, wall and symmetry.

The first step in a numerical model is model calibration. This means minimizing the effect of external factors and maintaining model conditions more similarly to a real-world situation. The present numerical model has been done based on the experimental model; hence, its calibration and validation have been carried out accordingly. The calibration of the numerical model with respect to simulation and boundary conditions is discussed here. It is necessary to achieve stable conditions in order to extract accurate values

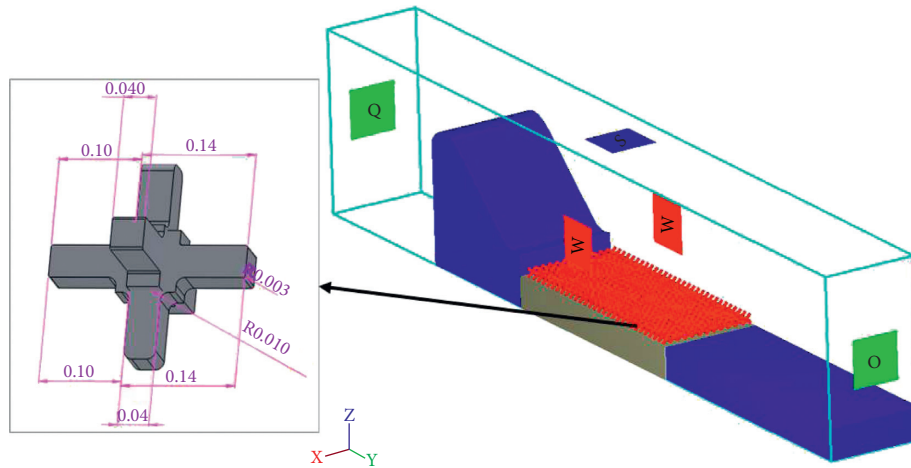


FIGURE 2: Boundary conditions applied to numerical modeling and geometric dimensions of A-Jacks 1 concrete block.

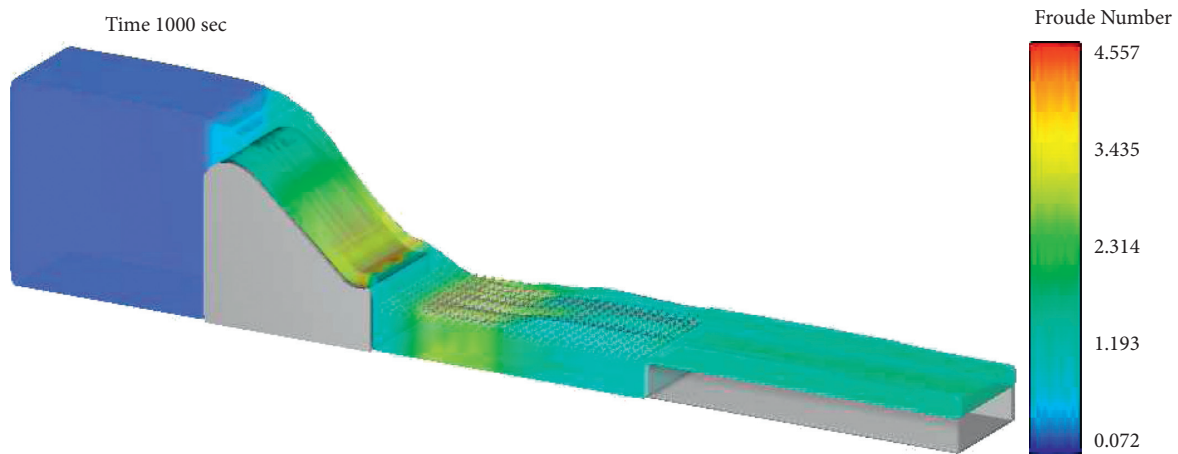


FIGURE 3: Flow development in the Flow3D numerical model.

from numerical or real-world model data. In the numerical model under investigation, the proper time for extracting the results from the model was considered 180 minutes after examining a number of models. Figure 3 illustrates how the flow passes over the spillway at different points in time. The flow becomes stable over the spillway and the downstream channel after 40 seconds.

At the onset of calculations for the numerical model ($T=0.0$ sec), the fluid height was introduced in correspondence with the experimental data intended for the model. With the beginning of calculations by the software ($T=1$ sec), the flow passes over a part of the ogee spillway. At $T=5$ sec, the flow is led out from the ogee spillway. At $T=10$ sec, the unsteadiness effect of the flow on the downstream channel is evident. Although the flow seems steady at $T=15-35$ sec, more careful attention to the differences in the fluid fraction contours at the upcoming times reveals that the flow becomes steady from $T=40$ sec. To ascertain the steadiness and equilibrium of the flow field over ogee spillways, the diagram on variations in the rate of flow passing inflow and outflow boundaries per time is presented, as in Figures 4 and 5, which indicate flow stability and steadiness after 40

seconds, which in turn confirms simulation stability. All analyzes of flow hydrodynamic parameters under stable flow conditions have been performed on a numerical model.

4. Results and Discussion

To study the effect of A-Jacks element sizes on the flow hydraulic parameters, 6 element sizes, whose geometric dimensions were increased by 20%, were placed on the erodible bed of the channel downstream of the ski-jump. Data collection stations are shown in Figure 6. The numerical model was run for each considering a constant flow rate, and the hydraulic parameters were analyzed. It should be noted that the hydraulic parameters for 9 downstream stations were evaluated as relative parameters (X/H).

Investigation of the flow velocity profile gains great significance in finding the pattern of the flow jet energy dissipation downstream of flip buckets. The profile variation trend from the onset of jet formation to the end of erodible locations indicates the manner of flow development and turbulence variations. In this section, after extraction of the numerical simulation results, a comparison of velocity

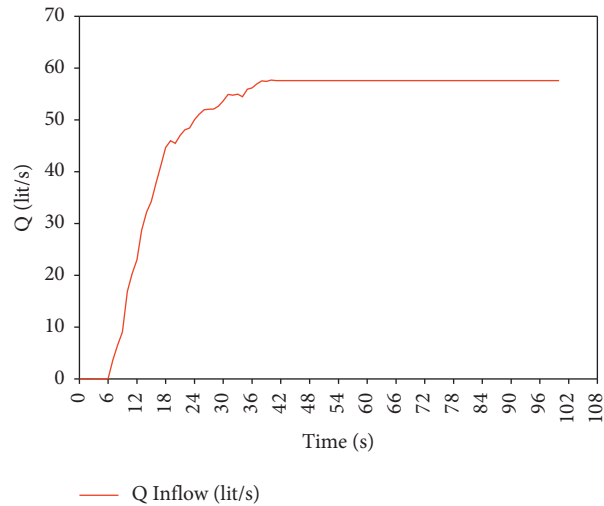


FIGURE 4: Flow rate variations at the inflow boundary in proportion to the time of running the numerical model.

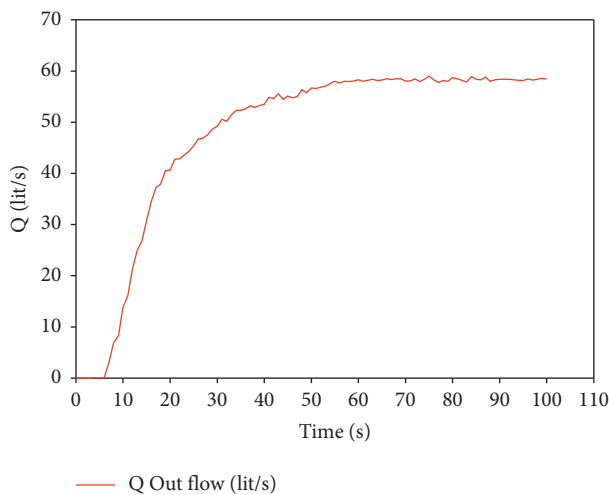


FIGURE 5: Flow rate variations at the outflow boundary in proportion to the time of running the numerical model.

profiles nondimensionalized in proportion to the flow velocity in the flip bucket (U/U_B) and for different stations with different sizes of A-Jacks element armors was provided.

As depicted in Figure 7, at station $X/L = 0$, which represents the flow jet point of inlet into the tailwater, variations in A-Jacks dimensions show little effect on velocity profiles. With the flow passing over the A-Jacks, the flow turbulence increases due to A-Jacks roughness. In other words, the roughness stemming from A-Jacks element's piers ($X/L = 0$) causes flow separation from bed and its return at station ($X/L = 1$). Presence of A-Jacks armors on bed generates a positive pressure gradient, leading to velocity reduction near the bed. Reduction in velocity gradients is highly evident for A-Jacks with larger dimensions, which indicates that the bed erodibility potential as a result of using larger armors could entail bed scour reduction. After the shear layer, velocity variations become almost constant towards the water surface, as seen in velocity profiles. This is because the flow

structure at depths closer to the water surface is unaffected by the bed shape. Given that most flow scour holes occur in the region where the flow jet impacts the downstream side, using larger elements can strengthen velocity profiles towards increasing the flow turbulence and flow energy dissipation and make for more desirable conditions of the flow in this region. It is important to note that with the passage of flow into the downstream region, the elements' dimensions at regions farther away from the jet impact will have less effect owing to flow development and full formation of the boundary layer.

Since the Reynolds stress turbulence parameters have a number of transport terms and heterogeneous and non-isotropic diffusions in comparison with other turbulence parameters, they are more accurate and sensitive in energy transfer from the mean flow to fluctuating parameters. Accordingly, after extraction of the numerical simulation's results in this section, the Reynolds stresses including $\tau_{u'w'}$ and $\tau_{v'w'}$ parameters along the flow depth for station $X/L = 0.5$ are discussed (Figure 8).

In the region near the bed with A-Jacks armor, the Reynolds shear stresses τ_{u,w_t} and τ_{v,w_t} from the channel bed increase. Then, further away from the bed in $Y/Y_t = 0.5 - 1.5$ region, the Reynolds shear stresses of τ_{u,w_t} and τ_{v,w_t} reach their maximum. Afterwards, in $Y/Y_t = 2 - 10$ region, the Reynolds shear stresses τ_{u,w_t} and τ_{v,w_t} decrease to near-zero values at the water surface. Near-zero values close to the water surface suggest highly low shear in this region and the effect of free surface. This means that the shear stress is minimum at a layer near the water surface, and the geometry of A-Jacks armors has not been able to affect the free water surface at this layer. In other words, although increasing A-Jacks armors' dimensions entails an increase in the Reynolds shear stress parameters, it does not have much effect along the flow depth. According to the presented diagram, the maximum Reynolds shear stress values occurred in a region farther away from the bed, the result of which is that the shear stress in the vicinity of sediment particles at the layer beneath the armor is zero; therefore, it can play a significant part in reducing scour in these regions.

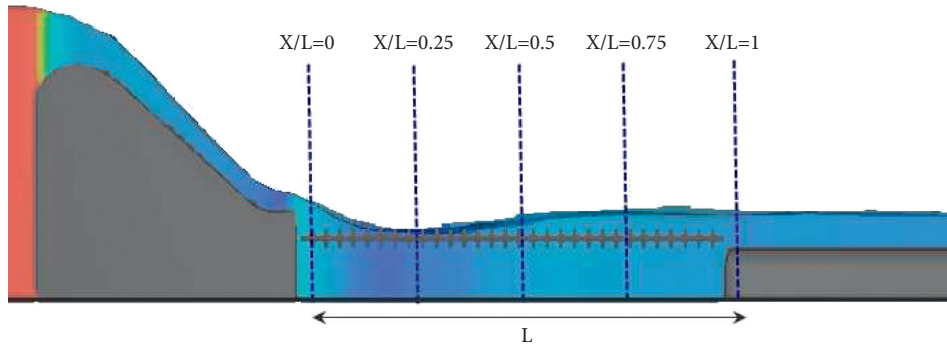


FIGURE 6: Side view of the numerical model and the properties of the stations measuring flow hydrodynamic parameters.

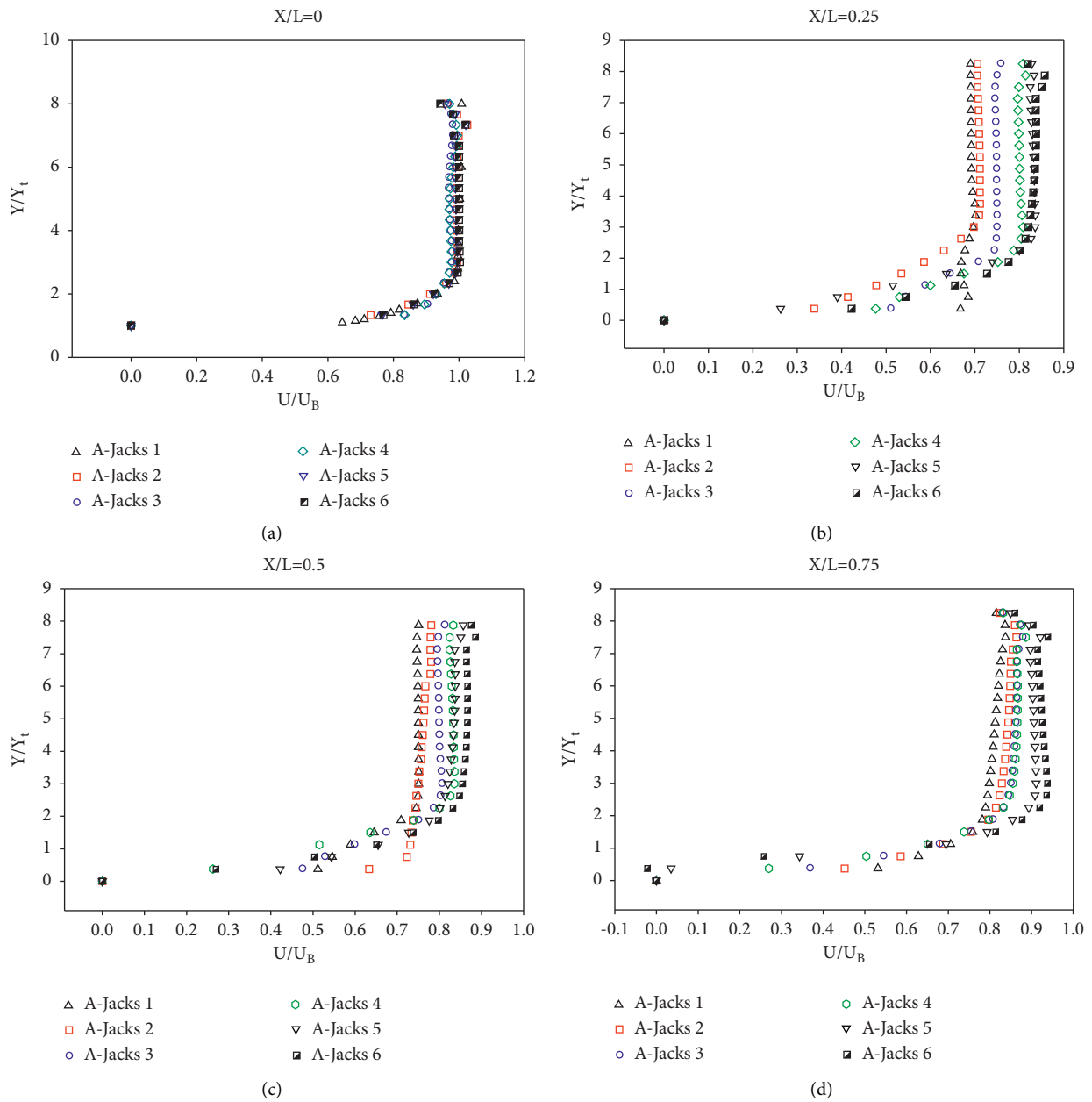


FIGURE 7: Continued.

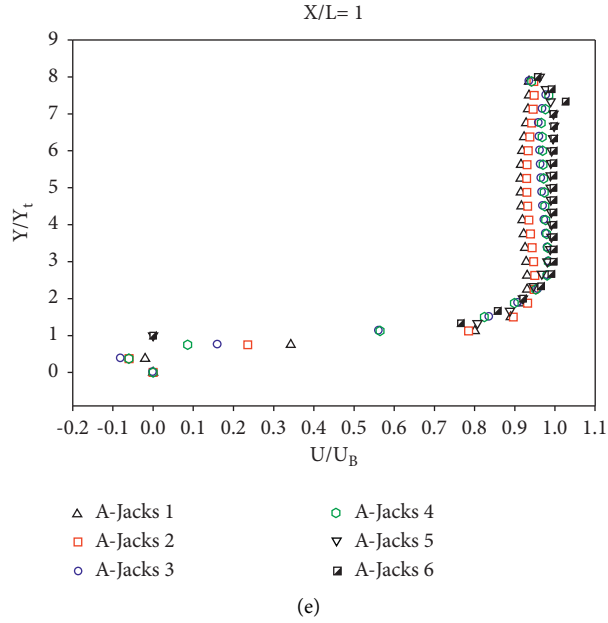


FIGURE 7: Velocity profiles at station ($X/L = 0, 0.25, 0.5, 0.75, 1$) downstream of the flip bucket with A-Jacks (1 to 6).

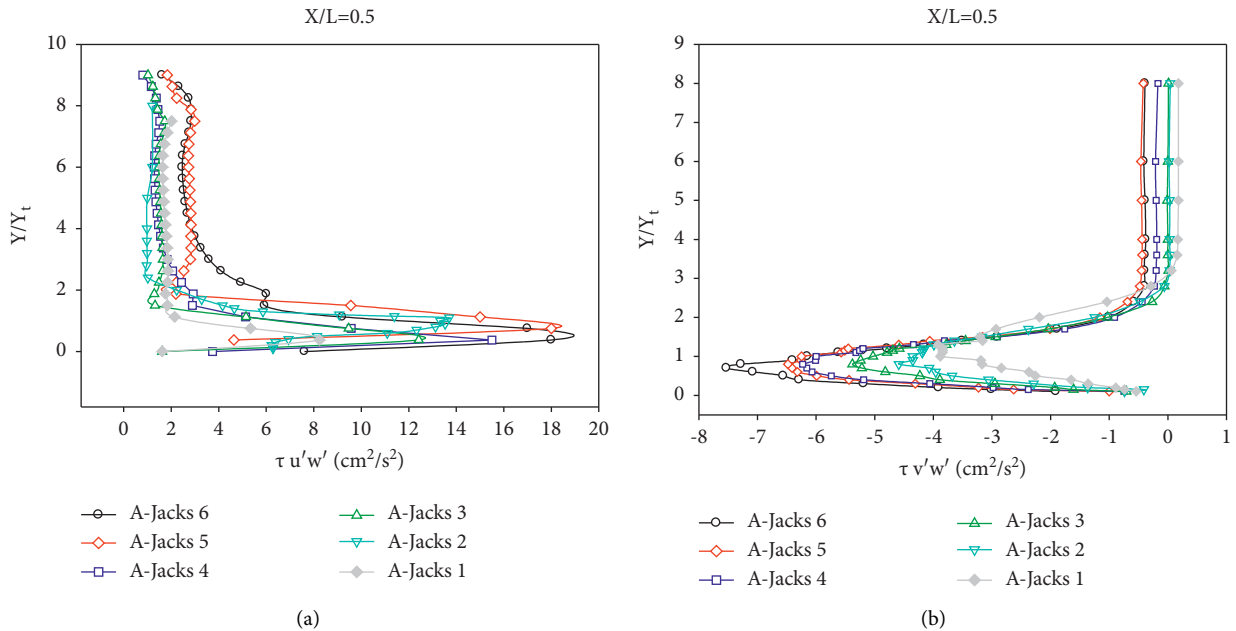


FIGURE 8: Reynolds shear stress profiles of $\tau_{u'w'}$ and $\tau_{v'w'}$ for station $X/L = 0.5$.

A-Jacks armors have 6 interlocked piers, which cause great roughness at bed. Due to creation of roughness at bed, when the flow is passing over the rough bed, the adhesive drag force functions as the main inhibitor against the flow [29]. In rough beds similar to A-Jacks armors, the skin friction coefficient (C_f) is put forth for measuring resistance against the flow. The skin friction coefficient (C_f) along the flow length has been extracted for 6 modes of A-Jacks armors using the simulations, and it is shown in Figure 9.

As shown in Figure 9, with the impact of the jet with A-Jacks armor, skin friction coefficient (C_f) values are

highly varied due to great turbulence resulting from the impact of the jet with the tailwater. Since the shear stress values parameters ($C_f = 2[u_*'/U]^2$) and the flow velocity are involved in the skin friction coefficient (u_*') equation, the shear velocity values could increase along the flow length and entail an increase in the skin friction coefficient (C_f) values. The results of the numerical model indicate that with an increase in the size of A-Jacks armors, vortex flows between the piers lead to a decrease in the resulting flow energy. Along A-Jacks armors, the elements' roughness affects both the friction force and the

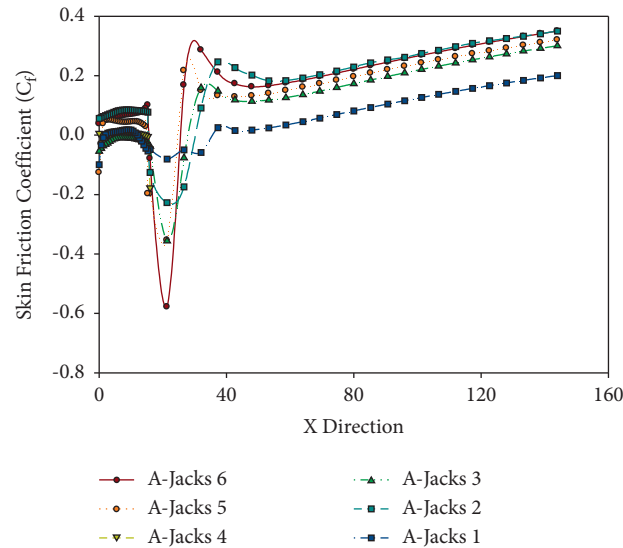


FIGURE 9: . Skin friction coefficient (C_f) along the flow length for 6 modes of A-Jacks armors.

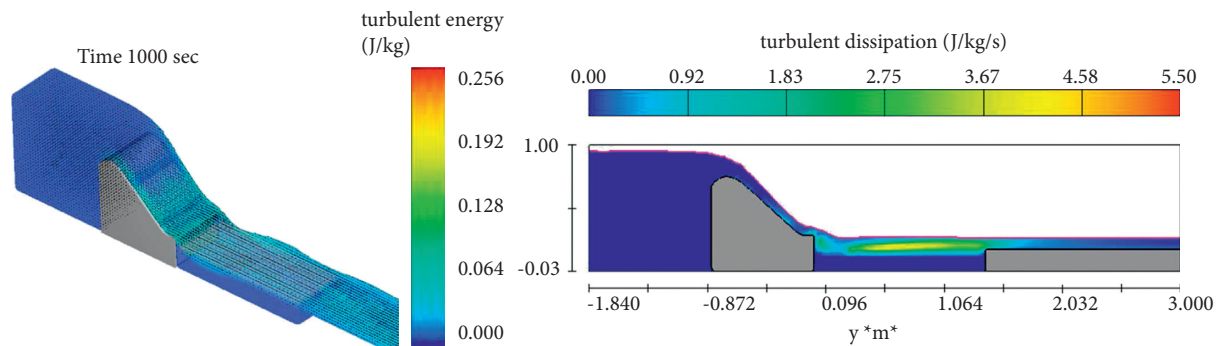


FIGURE 10: Flow turbulence energy variations and flow turbulence energy dissipation downstream of flip buckets.

compressive drag force from the fluid on the bed. Under the same hydraulic conditions, the compressive drag force increases as much as the elements become larger, and the overall force imposed on the flow will be larger, leading to an increase in energy loss. The parameters of the flow turbulence energy values and the flow turbulence energy dissipation extracted from the Flow3D numerical model are depicted in Figure 10. Increase in flow turbulence energy dissipation downstream of flip buckets significantly mitigates the conditions of scour occurrence and confirms the proper performance of A-Jacks armors in reducing scour depth.

5. Conclusion

Regarding the extensive use of flip buckets in chute spillways, particularly in major (concrete or embankment) dams, it is regarded important to build and analyze a bed protection system for this type of dissipater's tailwater. Accordingly, this study analyzed the hydrodynamic parameters of the A-Jacks bed protective system. The bed erosion mechanism downstream of flip buckets is

made analyzable by determining the flow hydrodynamic parameters. Due to flow jet turbulence, there are vortices developed in the region near the bed and the region downstream of the flip bucket jet that can play an important role in digging, lifting, and transporting sediments. As the numerical model results indicated, utilizing A-Jacks armors could entail desirable variations in flow velocity profiles U/U_B , Reynolds stresses $\tau_{u'w'}$ and $\tau_{v'w'}$, and the skin friction coefficient C_f . The size of A-Jacks elements can have a role in increasing the flow turbulence to a certain depth so that after the impact of the flow with A-Jacks armor, the vortices' intensity as well as the shear stress affecting the bed gradually decreases because first the water depth values at the tailwater are increased locally and then the excessive flow energy is dissipated due to the armor's roughness. As a result of this process, the shear stress values and the vortices' intensity decrease. Altogether, the numerical model results suggest that A-Jacks armors enjoy highly proper geometric conditions which can improve the flow hydrodynamic conditions downstream of flip buckets towards reducing bed erosion to a very significant extent.

Data Availability

All data used to support the findings of the study are included within the article.

Conflicts of Interest

The authors declare that there are no conflicts of interest regarding the publication of this paper.

References

- [1] Report MHL 1251, "Physical modelling of a-jacks units in wave flume," Report No. MHL1251, Manly Hydraulics Laboratory, Manly Vale, Australia, 2003.
- [2] C. I. Thornton, C. C. Watson, S. R. Abt, C. M. Lipscomb, and C. M. Ullman, *Laboratory Testing of A-JACKS Units for Inland Applications: Pier Scour Protection Testing*, Colorado State University research report for Armortec Inc., Collins, CO, USA, 1999.
- [3] J. J. Mickel, "A-jacks matrix stability: deflection due to static normal loads," M.Sc. Thesis, Oregon State University, Corvallis, OR, USA, 1999.
- [4] T. E. Latta, "Static and dynamic stresses in a-jacks concrete armor units," M.Sc. Thesis, Oregon State University, Corvallis, OR, USA, 2000.
- [5] M. Zolghadr and M. Shafai Bejestan, "Six legged concrete (SLC) elements as scour countermeasures at wing wall bridge abutments," *International Journal of River Basin Management*, vol. 1, pp. 1–7, 2020.
- [6] M. Zolghadr, M. S. Bejestan, and M. Rezaeianzadeh, "Investigating the effect of six-legged element placement density on local scour at wing-wall bridge abutments," in *Proceedings of the World Environmental and Water Resources Congress 2016*, West Palm Beach, FL, USA, May 2016.
- [7] H. Reza, A. Ali, M. S. Bajestan, M. Ghomeshi, and M. Fathi Moghadam, "Investigation of the effect of six legged concrete (SLC) elements combined with riprap on scour depth at vertical wall bridge abutments," *Irrigation Sciences and Engineering*, vol. 42, no. 1, pp. 99–114, 2019.
- [8] K. Khalifehei, G. Azizyan, M. Shafai-Bajestan, and K.-w. Chau, "Stability of A-Jack concrete block armors protecting the riverbeds," *Ain Shams Engineering Journal*, vol. 12, no. 1, pp. 381–391, 2021.
- [9] K. Khalifehei, G. Azizyan, M. Shafai-Bajestan, and K. W. Chau, "Experimental modeling and evaluation sediment scouring in riverbeds around downstream in flip buckets," *International Journal of Engineering*, vol. 33, no. 10, pp. 1904–1916, 2020.
- [10] M. R. Nou, M. A. Moghaddam, M. S. Bajestan, and H. M. Azamathulla, "Control of bed scour downstream of ski-jump spillway by combination of six-legged concrete elements and riprap," *Ain Shams Engineering Journal*, vol. 11, pp. 1047–1059, 2020.
- [11] H. Vaseli, L. Hashemian, and A. Bayat, "Productivity analysis of micro-trenching using simphony simulation modeling," *Civil Engineering Journal*, vol. 6, no. 11, pp. 2131–2142, 2020.
- [12] C. W. Hirt and B. Nichols, "Flow-3D User's manual," *Flow Science Inc*, vol. 107, 1988.
- [13] N. J. H. Al-Mansori, L. S. A. Al-Zubaidi, and Al-Zubaidi Laith Shaker Ashoor, "One-dimensional hydrodynamic modeling of the euphrates river and prediction of hydraulic parameters," *Civil Engineering Journal*, vol. 6, no. 6, pp. 1074–1090, 2020.
- [14] A. Yamini, S. H. M. Omid, M. R. Kavianpour, and Ramin Safari Ghaleh, "Hydrodynamic performance and cavitation analysis in bottom outlets of dam using CFD modelling," *Advances in Civil Engineering*, vol. 2021, Article ID 5529792, 14 pages, 2021.
- [15] S. M. Mousavimehr, Omid Aminoroayaie Yamini, and M. R. Kavianpour, "Performance assessment of shockwaves of chute spillways in large dams," *Shock and Vibration*, vol. 2021, Article ID 6634086, 17 pages, 2021.
- [16] A. Anand, M. Beg, and N. Kumar, "Experimental studies and analysis on mobilization of the cohesionless sediments through alluvial channel: a review," *Civil Engineering Journal*, vol. 7, no. 5, pp. 915–936, 2021.
- [17] A. Temel and D. Mustafa, "Time dependent investigation of the wave induced scour at the trunk section of a rubble mound breakwater," *Ocean Engineering*, vol. 221, Article ID 108564, 2021.
- [18] G. Mihajlović and M. Živković, "Sieving extremely wet earth mass by means of oscillatory transporting platform," *Emerging Science Journal*, vol. 4, no. 3, pp. 172–182, 2020.
- [19] A. Movahedi, M. R. Kavianpour, and Omid Aminoroayaie Yamini, "Evaluation and modeling scouring and sedimentation around downstream of large dams," *Environmental Earth Sciences*, vol. 77, no. 8, pp. 1–17, 2018.
- [20] B. Fazelabdolabadi and M. H. Golestan, "Towards bayesian quantification of permeability in micro-scale porous structures-the database of micro networks," *HighTech and Innovation Journal*, vol. 1, no. 4, pp. 148–160, 2020.
- [21] M. Nazari-Sharabian, M. Karakouzian, M. Karami, and M. Karami, "Sacrificial piles as scour countermeasures in river bridges a numerical study using FLOW-3D," *Civil Engineering Journal*, vol. 6, no. 6, pp. 1091–1103, 2020.
- [22] Helbar, M. Sadat, Atefeh Parvaresh Rizi, J. Farhoudi, and A. Mohammadi, "3D flow simulation to improve the design and operation of the dam bottom outlets," *Arabian Journal of Geosciences*, vol. 14, no. 2, pp. 1–11, 2021.
- [23] K. Khosravi, Z. S. Khozani, and L. Mao, "A comparison between advanced hybrid machine learning algorithms and empirical equations applied to abutment scour depth prediction," *Journal of Hydrology*, vol. 596, Article ID 126100, 2021.
- [24] V. Yakhot, S. A. Orszag, S. Thangam, T. B. Gatski, and C. G. Speziale, "Development of turbulence models for shear flows by a double expansion technique," *Physics of Fluids*, vol. 4, no. 7, pp. 1510–1520, 1992.
- [25] V. Zhaba and E. Gohman, "Activation level and probabilities of electromagnetic γ -transitions in the reaction $77\text{Se}(\gamma, \gamma')$ 77mSe ," *Emerging Science Journal*, vol. 4, no. 3, pp. 165–171, 2020.
- [26] K. Khalifehei, G. Azizyan, and C. Gualtieri, "Analyzing the performance of wave-energy generator systems (SSG) for the southern coasts of Iran, in the Persian gulf and Oman sea," *Energies*, vol. 11, no. 11, p. 3209, 2018.
- [27] S. B. Dirbude and V. K. Maurya, "Effect of uniform magnetic field on melting at various Rayleigh numbers," *Emerging Science Journal*, vol. 3, no. 4, pp. 263–273, 2019.
- [28] A. Movahedi, M. Kavianpour, and O. Aminoroayaie Yamini, "Experimental and numerical analysis of the scour profile downstream of flip bucket with change in bed material size," *ISH Journal of Hydraulic Engineering*, vol. 25, no. 2, pp. 188–202, 2019.
- [29] R. Fernández, A. J. Vitale, G. Parker, and M. H. García, "Hydraulic resistance in mixed bedrock-alluvial meandering channels," *Journal of Hydraulic Research*, vol. 59, no. 2, pp. 298–313, 2021.

Research Article

Experimental Investigation on the Ductility of Concrete Deep Beams Reinforced with Basalt-Carbon and Basalt-Steel Wire Hybrid Composite Bars

Mohammadamin Mirdarsoltany , Alireza Rahai , and Farzad Hatami 

Department of Civil Engineering, Faculty of Civil Engineering, Amirkabir University of Technology (Tehran Polytechnic), Tehran, Iran

Correspondence should be addressed to Mohammadamin Mirdarsoltany; amin.st@aut.ac.ir

Received 16 June 2021; Revised 2 July 2021; Accepted 12 July 2021; Published 22 July 2021

Academic Editor: S. Mahdi S. Kolbadi

Copyright © 2021 Mohammadamin Mirdarsoltany et al. This is an open access article distributed under the Creative Commons Attribution License, which permits unrestricted use, distribution, and reproduction in any medium, provided the original work is properly cited.

Using steel bars in corrosive conditions imposes a high cost on concrete elements. This is due to corrosion of steel bars. In order to eliminate this issue, the use of composite materials in civil engineering practices has become an area of focus because of their acceptable mechanical behavior, such as high strength, suitable durability in corrosive environmental conditions, and low weight. However, composite bars show low ductility and brittle fracture in tensile tests. These weaknesses act as a stumbling block to the widespread use of such bars in concrete elements. Therefore, a new generation of hybrid composite bars, fabricated by a combination of two or more composite fibers, has been proposed to eliminate these downsides. In this research project, six reinforced concrete beams in three groups, including beams reinforced with basalt-wire hybrid composite bars, carbon-basalt hybrid composite bars, and steel bars, have been evaluated in statistical 4-point flexural tests. The test results showed that the energy absorption rate for beams reinforced with basalt-wire hybrid bars compared to beams reinforced with steel bars was up to 93% in the statistical 4-point flexural test.

1. Introduction

Steel bars have many weaknesses in aggressive environmental conditions due to corrosion [1]. These weaknesses, in the long run, cause damages to concrete elements. The very epitome of such weaknesses is cracking and loss of concrete cover and reducing the function of concrete elements [2, 3]. Various methods have been proposed by researchers to eliminate these weaknesses. One of the proposed methods is using a hybrid system in which steel bars and composite bars are used in concrete elements simultaneously [4–7]. Zadeh and Nanni [8] presented a theoretical method to investigate the behavior of concrete elements reinforced with composite glass fiber-reinforced polymer (GFRP) bars under simultaneous bending and axial forces. Ferreira et al. [9] showed that the cross-sectional shape of composite bars plays an essential role in the behavior of concrete elements.

Almusallam [10] proposed a numerical method for predicting the bending behavior of beams reinforced with FRP bars. Toutanji and Deng [11] evaluated the cracks' width in 6 specimens of concrete beams reinforced with GFRP bars.

Using composite bars instead of using steel ones eliminates bars' corrosion in concrete elements because this type of bars has acceptable mechanical properties, such as high environmental durability and high resistance to corrosion [9, 12]. However, using such bars is limited due to their low elastic modulus and also their low ductility [13, 14]. Therefore, utilizing hybrid composite bars that are made from 2 or more fibers is proposed to deal with these weaknesses. Mirdarsoltany et al. [15] made hybrid composite bars using steel bars and glass fibers. This type of bars had an elastic modulus of 96 GPa and tensile strength of about 790 MPa. Ma et al. [16] fabricated hybrid composite bars with steel bars and basalt fibers. The test results showed that

hybridization makes an improvement in the elastic modulus of this type of bars compared to GFRP bars. Cui and Tao [17] made only one type of hybrid composite bars using carbon, Twaron, glass, and steel fibers, which were much more resistant to corrosion than steel bars, and they had an elastic modulus of 142.11 GPa and tensile strength of 628 MPa. Two types of hybrid composite bars using carbon and glass fibers were made by Liang et al. [18]. In the first type, carbon fibers were placed in the core of the bar and glass fibers around it, and in the second type, carbon fibers were distributed irregularly in the cross section of the bar. These specimens were evaluated under a one-way tensile test. Test results showed a yield point of 1153 MPa and tensile strength of 1191 MPa with a final strain of 3.5%.

Seo et al. [19] investigated the effect of the hybridization process on the elastic modulus of composite bars made of glass fibers, which showed a 270% increase in elastic modulus compared to GFRP bars. Hwang et al. [20] evaluated two specimens of hybrid bars with diameters of 13 and 16 mm and the percentage of steel wires with diameters of 0.5, 1, and 2 mm with steel ratios of 10, 30, 50, and 70%. The results showed an increase in the elastic modulus of hybrid composite bars from 20 to 190% compared to GFRP bars. Correia et al. [21] built two types of glass-steel and basalt-steel composite hybrid bars and compared their tensile behavior results with GFRP bars [22]. The results of the specimens showed that this process caused nonlinear behavior in these types of hybrid composite bars [23]. Since few tests have been performed on evaluating the performance of hybrid composite bars in concrete elements, in this research project, four specimens of concrete beams reinforced with hybrid composite bars were investigated under statistical four-point flexural tests [24]. Moreover, results were compared with 2 specimens of beams reinforced with steel bars.

2. Materials and Methods

Six concrete beams reinforced with hybrid composite bars and steel bars were evaluated. All the specimens were subjected to a statistical four-point flexural test, and the test variables are the type of bars used in the sections.

2.1. Bars. For reinforcing all of 6 specimens, steel bars with a diameter of 10 mm are used as compression bars, and also, bars with a diameter of 8 mm are used as transverse reinforcements. For longitudinal bars in the tensile area of the beam, steel bars with a diameter of 10 mm are used as a control specimen. Six numbers of hybrid bars in 2 types (basalt-wire bars and carbon-basalt bars) with a length of 950 mm and diameter of 10 mm were fabricated by a hybridization process and then used as a reinforcement for concrete beams. In basalt-wire hybrid composite bars, 22% of the cross-sectional area was made of steel wires with a diameter of 1.5 mm, and 78% of bars' cross section were basalt roving [25]. It should be noted that the volume of the resin was not considered [26]. The carbon-basalt hybrid composite bars were made of carbon and basalt composite fibers. Carbon roving fibers were used in the bar's core and basalt roving fibers were placed as the core coating [27]. The

mechanical properties of materials used in the fabrication of hybrid composite bars were obtained from tensile tests, and their results are shown in Table 1. The mechanical behavior of bars used for reinforcing concrete specimens is shown in Table 2. It should be noted that hybrid composite bars were tested in accordance with ACI 440K standards.

Figures 1 and 2 show the strain-stress diagram of basalt-carbon and basalt-steel hybrid composite bars obtained from the tensile tests. Figure 3 shows a tensile test of hybrid composite bars.

It should be noted that, to increase the adhesion of hybrid composite bars and the concrete surface, bars' surfaces were covered with a sand coating method to prevent these bars from slipping during the four-point test. Figure 4 shows the surface of hybrid composite bars.

2.2. The Concrete. The compressive strength of concrete was measured at 41 MPa on the day of the test. Figure 5 shows 150 * 300 mm standard cylinder for measuring the compressive strength of concrete on the day of the test.

2.3. Test Specimens. The concrete beams were 250 mm high, 150 mm wide, and 1000 mm long. The stirrups used to prevent shear rupture are placed 100 mm apart. The amount of concrete cover was 27.5 mm for all concrete beam specimens. All beams are designed based on the rupture of the longitudinal bars used. Figures 6 and 7 show details of concrete beam specimens. Specimens of concrete beams reinforced with basalt-wire, carbon-basalt, and steel hybrid bars are shown in Table 3.

2.4. Loading Beams. Beams were subjected to the four-point flexural test by using the Schenck machine. The capacity of the device was 600 KN, and loading was done using hydraulic rams [28]. These rams are also based on the speed of movement as the input [29]. Therefore, after receiving this speed, the machine records the amount of force applied to the ram per shift, and finally, the output will be the load-displacement diagram. The displacement is related to the main ram. The 4-point flexural test is designed in which the area between two loading rams is subjected to pure bending. Figure 8 shows the loading of concrete beams. Moreover, it should be noted that, according to ISIS module 3, all specimens were designed based on failure of longitude reinforcement.

3. Results and Discussion

3.1. Test Results of Concrete Beams. As mentioned in the previous section, in this research project, six specimens of concrete beams with specific dimensions were subjected to the 4-point flexural test. In this test, the force-displacement diagram of the beam was obtained via using a Schenck machine.

3.2. Comparison of Force-Displacement Diagrams of Reinforced Concrete Beams. As shown in Figure 8, the force-

TABLE 1: Mechanical properties of materials used to fabricate hybrid composite bars.

Materials	Tensile strength (MPa)	Elastic modulus (GPa)	Tensile elongation (%)
Carbon T300 fibers	1230–1540	225	1.25–1.5
Basalt fibers	1050–1100	72	2.8–3
Steel wires	1270–1470	200	—
Vinyl ester 901	75	3	4.5–5

TABLE 2: Mechanical specifications of bars used in concrete beams.

Materials	Tensile strength (MPa)	Elastic modulus (GPa)
Basalt-wire	1027	55
Carbon-basalt	869	106
Steel	1180–1370	200

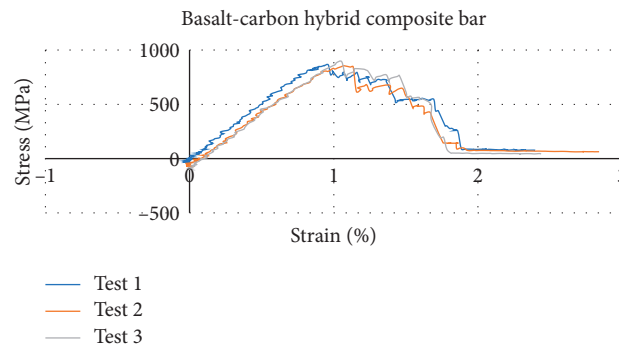


FIGURE 1: Stress-strain diagram of basalt-carbon hybrid composite bars.

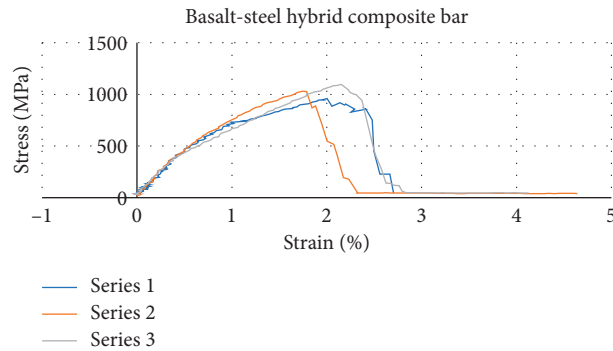


FIGURE 2: Stress-strain diagram of basalt-steel hybrid composite bars.

displacement diagram of the beams reinforced with basalt fibers and steel wire shows acceptable energy absorption and entry into the linear zone. These specimens also have a higher bearing capacity compared to a beam reinforced with steel bars. Figure 9 shows the cracks created in the concrete beam reinforced with basalt-wire hybrid composite bars. Unlike the beam reinforced with the hybrid composite bars made of basalt fibers and steel wire, the beam reinforced with hybrid composite bars made of carbon fibers and basalt does not exhibit good ductility behavior. It should be noted that this specimen has a higher bearing capacity compared to other beams. Figure 10 shows

the cracks created in the concrete specimen reinforced with the carbon-basalt hybrid composite bar. Figure 11 shows the mean value of the force and displacement of concrete beams.

3.3. The Amount of Energy Absorbed in Concrete Specimens.

To calculate the energy absorbed by each of the specimens, the area under the force-ductility diagram of each beam is calculated, which is shown in Table 4. In order to compare the ductility of beams, ductility-based methods in beams reinforced with nonsteel bars are not applicable due to the



FIGURE 3: Tensile test of hybrid composite bars.



FIGURE 4: The surface of hybrid composite bars.



FIGURE 5: Measuring compressive strength of concrete using standard cylinders.

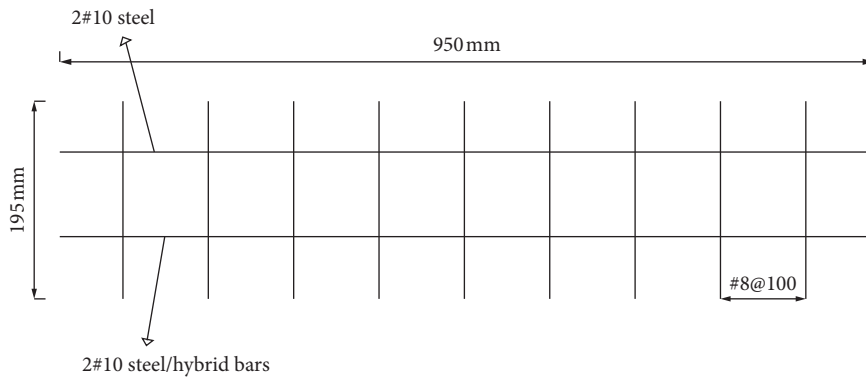


FIGURE 6: How to reinforce concrete specimens.

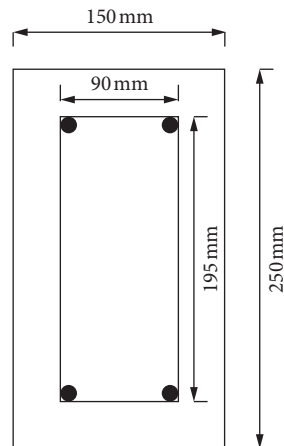


FIGURE 7: Cross section of concrete specimens.

TABLE 3: Specifications of built concrete beams.

Specimen ID	f_c (MPa)	A_f (mm ²)
Basalt-wire	41.2	78.5
Carbon-basalt	40.8	78.5
Steel	41.3	78.5

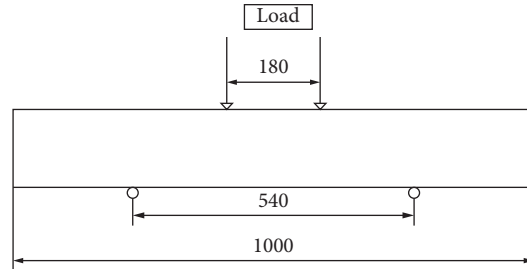


FIGURE 8: Four-point flexural loading of concrete beams.

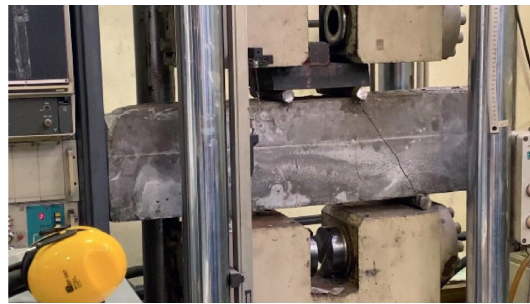


FIGURE 9: Cracks made in the concrete beam reinforced with the basalt-wire hybrid composite bar.



FIGURE 10: Cracks created in a specimen of the concrete beam reinforced with the carbon-basalt hybrid bar.

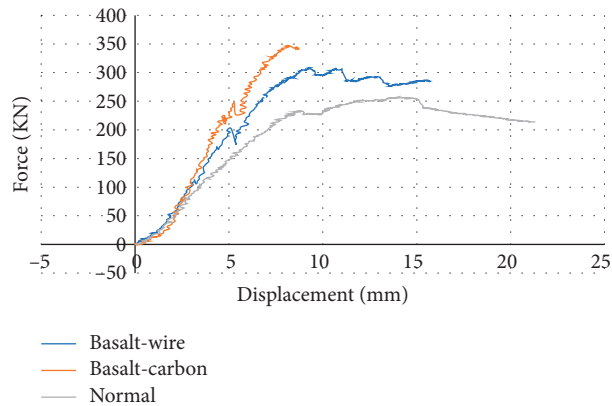


FIGURE 11: Results of the 4-point flexural test of reinforced concrete beams.

TABLE 4: The amount of energy absorbed by reinforced concrete beams.

Beam ID	Absorbed energy (J)	Relative energy absorbed
Steel bar-reinforced beam	5812.021	—
Basalt-wire bar-reinforced beam	5439.252	0.93
Carbon-basalt bar-reinforced beam	2920.322	0.5

lack of a specific yield point of the hybrid composite bars. In order to evaluate the amount of energy absorbed by the beam, the area under the load-displacement diagram can be calculated. The area below this diagram is equal to $\int_0^{d_u} F \cdot dl$. In this equation, d_u is the final rise of the section, dl is the differential rise, and F is the ram force.

4. Conclusion

In this research project, force-displacement diagrams of 4 concrete beams in two groups, including beams reinforced with carbon-basalt and beams reinforced with basalt-wire hybrid composite bars, were compared with the force-displacement results of beams reinforced with steel bars under the four-point test. Beams reinforced with basalt-wire hybrid composite bars showed ductile behavior during rupture and had about 1.2 times higher bearing capacity compared to steel bar-reinforced concrete beams. In concrete beams reinforced with carbon-basalt hybrid composite bars, the specimen did not show ductile behavior at rupture, and the rupture was sudden, but compared to the reinforced concrete specimen with the steel bar, it had a bearing capacity of about 1.3 times higher. Compared to concrete beams reinforced with steel bars, beams reinforced with basalt-wire and carbon-basalt hybrid composite bars showed less displacement in the 4-point flexural tests, and this value was about 21.3 mm, 15.7 mm, and 8.7 mm, respectively. Comparing the energy absorbed in beams reinforced with basalt-wire and carbon-basalt hybrid bars, the energy absorption rate of beams was 95% and 50% of concrete beams reinforced with steel bars, respectively.

Data Availability

Requests for access to these data should be made to the corresponding author (amin.st@aut.ac.ir).

Conflicts of Interest

The authors declare that there are no conflicts of interest regarding the publication of this paper.

Acknowledgments

The authors thank the individuals who provided help during the research and preparation of this manuscript.

References

- [1] M. Alexander and H. Beushausen, "Durability, service life prediction, and modelling for reinforced concrete structures - review and critique," *Cement and Concrete Research*, vol. 122, pp. 17–29, 2019.
- [2] M. Te Liang, R. Huang, and H. Y. Jheng, "Reconsideration for a study of the effect of chloride binding on service life predictions," *Journal of Marine Science and Technology*, vol. 19, no. 5, pp. 531–540, 2011.
- [3] M. Valipour, F. Pargar, M. Shekarchi, S. Khani, and M. Moradian, "In situ study of chloride ingress in concretes containing natural zeolite, metakaolin and silica fume exposed to various exposure conditions in a harsh marine environment," *Construction and Building Materials*, vol. 46, pp. 63–70, 2013.
- [4] J. Du, C. Wang, M. Qiao, X. Chang, and H. Chen, "Flexural behavior of concrete beams reinforced by CFRP bars," *2010 International Conference on Mechanic Automation and Control Engineering*, vol. 13, no. 5, pp. 1060–1063, 2010.
- [5] Z. Sun, Y. Yang, W. Qin, S. Ren, and G. Wu, "Experimental study on flexural behavior of concrete beams reinforced by steel-fiber reinforced polymer composite bars," *Journal of Reinforced Plastics and Composites*, vol. 31, no. 24, pp. 1737–1745, 2012.
- [6] A. Al-Rahmani and F. H. Abed, "Numerical investigation of hybrid FRP reinforced beams," in *Proceedings of the 2013 5th International Conference on Modeling, Simulation and Applied Optimization*, Hammamet, Tunisia, April 2013.
- [7] A. El Refai, F. Abed, and A. Al-Rahmani, "Structural performance and serviceability of concrete beams reinforced with hybrid (GFRP and steel) bars," *Construction and Building Materials*, vol. 96, pp. 518–529, 2015.
- [8] H. J. Zadeh and A. Nanni, "Design of RC columns using glass FRP reinforcement," *Journal of Composites for Construction*, vol. 17, no. 3, pp. 294–304, 2013.
- [9] A. J. M. Ferreira, P. P. Camanho, A. T. Marques, and A. A. Fernandes, "Modelling of concrete beams reinforced with FRP re-bars," *Composite Structures*, vol. 53, no. 1, pp. 107–116, 2001.
- [10] T. H. Almusallam, "Analytical prediction of flexural behavior of concrete beams reinforced by FRP bars," *Journal of Composite Materials*, vol. 31, no. 7, pp. 640–657, 1997.
- [11] H. Toutanji and Y. Deng, "Deflection and crack-width prediction of concrete beams reinforced with glass FRP rods," *Construction and Building Materials*, vol. 17, no. 1, pp. 69–74, 2003.
- [12] C. Barris, L. Torres, A. Turon, M. Baena, and A. Catalan, "An experimental study of the flexural behaviour of GFRP RC beams and comparison with prediction models," *Composite Structures*, vol. 91, no. 3, pp. 286–295, 2009.
- [13] P. F. Castro and N. J. Carino, "Tensile and nondestructive testing of FRP bars," *Journal of Composites for Construction*, vol. 2, no. 1, pp. 17–27, 1998.
- [14] H. Wang and A. Belarbi, "Ductility characteristics of fiber-reinforced-concrete beams reinforced with FRP rebars," *Construction and Building Materials*, vol. 25, no. 5, pp. 2391–2401, 2011.
- [15] M. Mirdarsoltany, A. Rahai, and F. Hatami, "Tensile behavior of GFRP hybrid composite bars in RC structures," *Solid State Technology*, vol. 64, no. 2, pp. 4955–4961, 2021.
- [16] G. Ma, Y. Huang, F. Aslani, and T. Kim, "Tensile and bonding behaviours of hybridized BFRP-steel bars as concrete

- reinforcement,” *Construction and Building Materials*, vol. 201, pp. 62–71, 2019.
- [17] Y.-H. Cui and J. Tao, “A new type of ductile composite reinforcing bar with high tensile elastic modulus for use in reinforced concrete structures,” *Canadian Journal of Civil Engineering*, vol. 36, no. 4, pp. 672–675, 2009.
- [18] Y. Liang, C. Sun, and F. Ansari, “Acoustic emission characterization of damage in hybrid fiber-reinforced polymer rods,” *Journal of Composites for Construction*, vol. 8, no. 1, pp. 70–78, 2004.
- [19] D.-W. Seo, K.-T. Park, Y.-J. You, and H.-Y. Kim, “Enhancement in elastic modulus of GFRP bars by material hybridization,” *Engineering*, vol. 5, no. 11, pp. 865–869, 2013.
- [20] J.-H. Hwang, D.-W. Seo, K.-T. Park, and Y.-J. You, “Experimental study on the mechanical properties of FRP bars by hybridizing with steel wires,” *Engineering*, vol. 6, no. 7, pp. 365–373, 2014.
- [21] L. Correia, F. Cunha, C. Mota, R. Figueiro, and J. P. Nunes, “Pseudo-ductile braided composite rods (BCRs) produced by braiding,” in *Proceedings of the ECCM is Europe’s Leading Conference on Composite Materials*, Seville, Spain, June 2016.
- [22] R. K. Mohammadi, M. Mirjalaly, M. Mirtaheri, and M. Nazeryan, “Comparison between uniform deformation method and Genetic Algorithm for optimizing mechanical properties of dampers,” *Earthquakes and Structures*, vol. 14, no. 1, pp. 001–010.
- [23] S. M. Seyed Kolbadi, H. Davoodian, and S. M. S. Kolbadi, “Evaluation of nonlinear behavior of reinforced concrete frames by explosive dynamic loading using finite element method,” *Civil Engineering Journal*, vol. 3, no. 12, pp. 1198–1225, 2017.
- [24] S. Mohammad Seyed Kolbadi, N. Hassani, and M. Safi, “Numerical evaluation on improvement performance of waved connection to reduce damage on buried gas pipeline,” *Shock and Vibration*, vol. 2020, Article ID 6680384, 9 pages, 2020.
- [25] P. Duy Nguyen, V. Hiep Dang, and N. Anh Vu, “Performance of concrete beams reinforced with various ratios of hybrid GFRP/steel bars,” *Civil Engineering Journal*, vol. 6, no. 9, pp. 1–18, 2020.
- [26] V. J. Jayakumar and S. Anandan, “Composite strain hardening properties of high performance hybrid fibre reinforced concrete,” *Advances in Civil Engineering*, vol. 2014, Article ID 363649, 9 pages, 2014.
- [27] M. Kolbadi, “Review on nonlinear behavior assessment of reinforced concrete frames by carbon fiber reinforced polymers under blast loading,” *Cur Trends Civil & Structures Engineering*, vol. 2, no. 5, 2019.
- [28] R. Balamuralikrishnan and J. Saravanan, “Effect of addition of alccofine on the compressive strength of cement mortar cubes,” *Emerging Science Journal*, vol. 5, no. 2, pp. 1–15, 2021.
- [29] T.-F. Yuan, K.-H. M. Jin-Young Lee, and Y.-S. Yoon, “Experimental investigation on mechanical properties of hybrid steel and polyethylene fiber-reinforced No-slump high-strength concrete,” *International Journal of Polymer Science*, vol. 2019, Article ID 4737384, 11 pages, 2019.

Research Article

Free and Forced Vibration Characteristics Analysis of a Multispan Timoshenko Beam Based on the Ritz Method

Cong Gao,¹ Fuzhen Pang,¹ Haichao Li ,¹ Hongfu Wang,¹ Jie Cui,² and Jisi Huang³

¹College of Shipbuilding Engineering, Harbin Engineering University, Harbin 150001, China

²College of Naval Architecture and Ocean Engineering, Jiangsu University of Science and Technology, Zhenjiang 212000, China

³China National Intellectual Property Administration, Beijing 100088, China

Correspondence should be addressed to Haichao Li; lihaichao@hrbeu.edu.cn

Received 27 April 2021; Revised 21 June 2021; Accepted 2 July 2021; Published 13 July 2021

Academic Editor: S. Mahdi S. Kolbadi

Copyright © 2021 Cong Gao et al. This is an open access article distributed under the Creative Commons Attribution License, which permits unrestricted use, distribution, and reproduction in any medium, provided the original work is properly cited.

The uniform formulation of dynamic vibration analysis of multispan beams is presented by using an efficient domain decomposition method in this paper. Firstly, the structure is divided into several equal sections based on domain decomposition method. Next, the artificial spring is used to simulate complex boundaries and continuity condition of multispan beam. Finally, the admissible displacement functions are expanded through Jacobi orthogonal polynomials, and the free and forced vibration characteristics of multispan beam structures can be obtained by using Rayleigh–Ritz method. Results for various boundary conditions, ratios of thickness to length (h/L), numbers, and stiffness of supporting springs are presented. It is clearly shown that accurate solutions can be obtained by using the proposed method, and this study extends the application range of the Jacobi polynomials-Ritz method. In addition, the research results of this paper can provide data support for engineers such as bridge designers to design multispan bridges.

1. Introduction

Multispan beam structure, as a basic component, has been widely used in areas such as aviation, bridge, ship, and other infrastructure because of its unique mechanical properties. This kind of structure is usually exposed to complex environment in the actual engineering application, which leads to being subjected to various environmental loads. In addition, the structure composition is relatively complex, and the traditional method is difficult and inefficient to simulate arbitrary boundary conditions. Therefore, the accurate method can be proposed to analyze of vibration characteristics of multispan beam structure has the important engineering value for guiding its structure design.

The bending vibration problems of beam structures mainly include Euler–Bernoulli beam, shear beam, Rayleigh beam, and Timoshenko beam [1]. Much effort has been dedicated to investigating the vibration characteristics of various structures in recent years. The main research methods include variational iteration method [2, 3],

differential quadrature method [4, 5], transfer matrix method [6], Ritz method [7, 8], domain decomposition method [9–11], finite volume method [12], and finite element method [13–15]. In the framework of Euler–Bernoulli beam theory, Chen et al. [16] put forward an energy finite element method (EFEM) to solve the high-frequency vibration response of beams with axial force. Considering the influence of nonuniform cross section, Sinir et al. [17] carried out the free and forced vibration characteristics of FGM Euler–Bernoulli beam by employing differential quadrature method (DQM). According to the Timoshenko beam theory, Akbas [18] investigated the forced vibration characteristics of axially functionally graded beams, in which the effects of material and geometric parameters are considered. The free and forced vibration of variable thickness functionally graded beam were carried out by Xiang and Yang [19], who developed Lagrange interpolation polynomials to solve the dynamic equation. Wu and Chen [20] dealt with the free and forced vibration behaviors of laminated composite beams based on higher-order zig-zag

theory, where the transverse shear stress is introduced into the equation of motion by using Hamilton's principle. More studies corresponding to the vibration characteristics of single-span beam can be found in [21–25].

With regard to multispan beam, based on the Euler–Bernoulli beam theory, Johansson et al. [26] deduced the closed-form dynamical solution of stepped multispan Bernoulli–Euler beam under concentrated moving loads. Fakhreddine et al. [27] performed nonlinear free and forced vibrations of multispan beam by means of single-mode approach, in which the formula derivation is in the framework of Hamilton's principle. Considering the influences of the boundary condition and damping, Ghannadiasl and Ajrlou [28] utilized the analytical method to analyze the forced vibration of multispan Euler–Bernoulli beams according to dynamic Green function formulation. Based on the Timoshenko beam theory, Chen et al. [29] demonstrated the application of the transfer matrix method for free and forced vibration analysis of multistep beams, where the forced vibration response was obtained on account of the modal superposition method. Besides, Lin and Chang [30] and Liu et al. [31] also employed the transfer matrix method to investigate the vibration characteristics of multispan beams. Lee [32] dealt with the free vibration characteristics of multispan beams for different dimension ratios and numbers of sections under different boundary conditions by using the pseudospectral method. In addition, the dynamic stiffness method was applied to investigate the free and forced vibration of multiple FGM multispan beams by Lien et al. [33], who considered the effect of cracks parameters on vibration characteristics of the FGM beams. Lv et al. [34] put to use the improved Fourier series approach and Rayleigh–Ritz method to analyze the vibration characteristics of multispan curved Timoshenko beams with general boundary restraints. Many of the studies in regard to multispan Timoshenko beam have been well documented in the excellent reviews of Yesilce [35–37] and his coworkers, who applied the secant method to study the free and forced vibration of multispan beam. According to the assumed mode method, Zhao et al. [38, 39] illustrated the free vibration solutions of multispan Timoshenko beams, where the vibration mode of the beam was modified by using the interpolation function, and the equations of motion of the structure were established by applying Hamilton's principle. Without any other assumptions, Lin and Tsai [40] performed the exact solutions of the multispan beam with multiple spring-mass systems, where the natural frequencies and corresponding modes were obtained from the differential equations of motion of the structure. Apart from the aforementioned beam theories, in order to investigate the free vibrations of multispan beam, Yesilce [41, 42] conducted numerous studies by using the secant method according to the Reddy–Bickford beam theory.

From the above analysis, it can be seen that the published literature has abundant research methods for the free vibration and forced vibration characteristics of single-span beam structures; however, there is a relative lack of research on the vibration characteristics of multispan beam structures, especially for forced vibration characteristics. In

addition, the vibration response law of multispan beam under complex boundary conditions is not clear yet, and the semianalytical methods for the vibration characteristics of multispan beam structures need to be further enriched. According to this, the study aims at conducting the free and forced vibration solutions of multispan beam structure subject to complex boundary restraints.

Previously, the author has conducted the free vibration characteristics of spherical shell structures [43]; the multi-segment partitioning, artificial spring technology, and Jacobi orthogonal polynomials are introduced to ensure the convergence and validity of the present method. According to the previous publication, several transversal displacement springs are arranged on the structure to represent the intermediate elastic support, and the forced vibration characteristics of the structure are solved by introducing the work done by the external concentrated load in this study. Finally, the parametric study of free and forced vibration characteristics of multispan beams is carried out.

2. Theoretical Formulations

2.1. Description of the Timoshenko Beam. Figure 1 displays the analytical model of multispan Timoshenko beam; L , b , and h , respectively, denote the length, width, and thickness of the structure. The Timoshenko beam differential equations of motion consist of two partial differential equations that can be obtained from literature [44]:

$$\begin{aligned} \rho A \omega^2 w(x) - \kappa G A \left(\frac{\partial \theta(x)}{\partial x} - \frac{\partial^2 w(x)}{\partial x^2} \right) &= 0, \\ \rho I \omega^2 \theta(x) - \kappa G A \left(\theta(x) - \frac{\partial w(x)}{\partial x} \right) + EI \frac{\partial^2 \theta(x)}{\partial x^2} &= 0, \end{aligned} \quad (1)$$

where ρ , E , and G are the density, Young's modulus, and extension rigidity, accordingly. A and I , respectively, represent the area of the cross section and the area moment of inertia, and κ denotes the shear correction factor which is assumed to be 5/6 during the study [45].

The bending moment $M(x)$ and transverse shearing forces $V(x)$ can be written as

$$\begin{aligned} M(x) &= EI \frac{\partial \theta(x)}{\partial x}, \\ V(x) &= -\kappa G A \left(\theta(x) - \frac{\partial w(x)}{\partial x} \right). \end{aligned} \quad (2)$$

The Timoshenko beam boundary restraints can be expressed as

$$\begin{aligned} k_0 w(x) &= -V(x), \quad K_0 \theta(x) = M(x), \quad \text{at } x = 0, \\ k_L w(x) &= V(x), \quad K_L \theta(x) = -M(x), \quad \text{at } x = L, \end{aligned} \quad (3)$$

where k_0 and k_L , respectively, represent the transversal displacement constraint springs and K_0 and K_L are the rotational constraint springs at ends $x = 0$ and $x = L$, which can be shown in Figure 1. It is possible to simulate different boundary conditions by setting the spring stiffness value. By

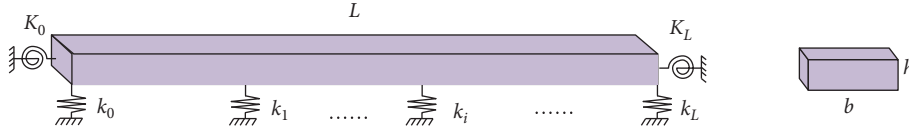


FIGURE 1: Calculation model of multispan beam structure.

changing the stiffness value of the supporting spring (k_i) at the middle elastic support of the multispan beam structure, different elastic support conditions of the multispan beam can be simulated, assuming that there are r supporting springs. The boundary conditions are given by

$$\begin{aligned} \text{clamped (C): } & \theta = 0, w = 0, \\ \text{pinned (P): } & M = 0, w = 0, \\ \text{free (F): } & M = 0, V = 0, \\ \text{sliding (S): } & \theta = 0, V = 0. \end{aligned} \quad (4)$$

In this paper, a multispan beam model is presented based on the domain decomposition method, as shown in Figure 2, assuming that the structure is divided into H segments, where the i th segment is coupled to $i+1$ th segment by a transversal displacement constraint spring ($\bar{k}_{i,i+1}$) and a rotational constraint spring ($\bar{k}_{i,i+1}$). In general, the connective spring stiffness is set to infinity to indicate the direct strong coupling between the two segments.

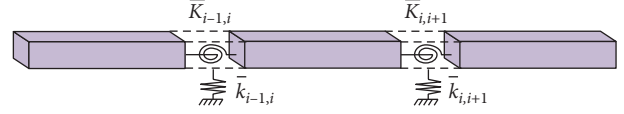


FIGURE 2: Diagram of multispan beam structure partition.

2.2. Admissible Displacement Functions Based on the Jacobi-Ritz Method. In this study, the admissible displacement functions are expanded through Jacobi orthogonal polynomials based on the multisegment partitioning technique [46, 47]. The unified Jacobi orthogonal polynomials are set in the range of $\phi \in [-1, 1]$, and the Jacobi polynomial can be transformed into Legendre polynomials ($\alpha = \beta = 0$), Chebyshev polynomials of first kind ($\alpha = \beta = -0.5$), and Chebyshev polynomials of second kind ($\alpha = \beta = 0.5$) by setting the values of two Jacobi parameters α and β . The recurrence formulas of Jacobi polynomials are given by

$$\begin{aligned} P_0^{(\alpha,\beta)}(\phi) &= 1, \\ P_1^{(\alpha,\beta)}(\phi) &= \frac{\alpha + \beta + 2}{2}\phi - \frac{\alpha - \beta}{2}, \\ P_i^{(\alpha,\beta)}(\phi) &= \frac{(\alpha + \beta + 2i - 1)\{\alpha^2 - \beta^2 + \phi(\alpha + \beta + 2i)(\alpha + \beta + 2i - 2)\}}{2i(\alpha + \beta + i)(\alpha + \beta + 2i - 2)} P_{i-1}^{(\alpha,\beta)}(\phi) \\ &\quad - \frac{(\alpha + i - 1)(\beta + i - 1)(\alpha + \beta + 2i)}{i(\alpha + \beta + i)(\alpha + \beta + 2i - 2)} P_{(i-2)}^{(\alpha,\beta)}(\phi), \end{aligned} \quad (5)$$

where $\alpha, \beta > -1$ and $i = 2, 3, \dots$

Therefore, the displacement function components of multispan beam structure based on Jacobi polynomials are shown as follows:

$$\begin{aligned} w(x) &= \sum_{m=0}^M A_m P_m^{(\alpha,\beta)}(x) e^{i\omega t}, \\ \theta(x) &= \sum_{m=0}^M B_m P_m^{(\alpha,\beta)}(x) e^{i\omega t}, \end{aligned} \quad (6)$$

where A_m and B_m signify the Jacobi expansion coefficients and M is the highest degrees of m .

The parameters such as velocity and acceleration can be obtained by deriving the displacement function one by one. Therefore, the main task of the whole solution process is to solve for the unknown Jacobi expansion coefficients.

2.3. Solution Procedure Based on the Hamilton Principle. Firstly, the energy description of the system is performed to find out the strain energy U^i , kinetic energy T^i , potential energy V , and work done by external load W_e for each partition under this system, respectively, and then the eigenvalue equation of multispan beam vibration is obtained based on Hamilton's principle.

The i th segment strain energy can be shown as follows:

$$U^i = \frac{1}{2} \int_0^{L_i} EI \left(\frac{\partial \theta(x)}{\partial x} \right)^2 dx + \frac{1}{2} \int_0^{L_i} \kappa GA \left(\theta - \frac{\partial w(x)}{\partial x} \right)^2 dx. \quad (7)$$

The i th segment kinetic energy of the structure can be expressed as

$$T^i = \frac{1}{2}\rho A\omega^2 \int_0^{L_i} w(x)^2 dx + \frac{1}{2}\rho I\omega^2 \int_0^{L_i} \theta(x)^2 dx. \quad (8)$$

The structural potential energy is divided into three parts, including the boundary spring potential energy V_b , the

$$V_b = \frac{1}{2} \left\{ \left[k_0 w(x)^2 + K_0 \left(\frac{\partial w(x)}{\partial x} \right)^2 + K_0 \theta(x)^2 \right]_{x=0} + \left[k_L w(x)^2 + K_L \left(\frac{\partial w(x)}{\partial x} \right)^2 + K_L \theta(x)^2 \right]_{x=L} \right\}. \quad (9)$$

The potential energy in connective springs ($\bar{k}_{i,i+1}$, $\bar{k}_{i,i+1}$) can be expressed as

$$V_s = \sum_{i=1}^{n-1} \frac{1}{2} \left\{ \bar{k}_{i,i+1} (w(x)^i - w(x)^{(i+1)})^2 + \bar{k}_{i,i+1} \left(\frac{\partial w(x)^i}{\partial x} - \frac{\partial w(x)^{(i+1)}}{\partial x} \right)^2 + \bar{k}_{i,i+1} (\theta(x)^i - \theta(x)^{(i+1)})^2 \right\}. \quad (10)$$

The potential energy in supporting springs is shown as below:

$$V_c = \sum_{t=1}^r \frac{1}{2} k_t w(x)^2. \quad (11)$$

Therefore, the total potential energy of the constraint conditions for the multispan beam can be defined as

$$V = V_b + V_s + V_c. \quad (12)$$

The work done by the external concentrated load can be written as

$$W_e = \int_0^L F \delta(x - x_0) w(x, t) dx, \quad (13)$$

where δ is the Dirac function (unit impulse function), F is the amplitude of the external concentrated load, and x_0 is the position of the action point.

The Lagrangian energy function \mathcal{L} can be presented as

$$\mathcal{L} = \sum_{i=1}^H (T^i - U^i) - V. \quad (14)$$

By differentiating the unknown Jacobi expansion coefficients of (14), one can obtain

$$\frac{\partial \mathcal{L}}{\partial \vartheta} = 0, \quad \vartheta = A_m, B_m. \quad (15)$$

The multispan beam dynamic characteristic equation can be expressed as

$$(\mathbf{K} - \omega^2 \mathbf{M}) \mathbf{Q} = \mathbf{F}, \quad (16)$$

where \mathbf{K} , \mathbf{M} , and \mathbf{Q} denote the stiffness matrix, mass matrix, and Jacobi coefficients matrix, respectively. The natural frequency and vibration modes for the multispan beam can be obtained by solving equation (16).

connective spring potential energy V_s , and the supporting spring potential energy V_c . The boundary potential energy for the multispan beam can be expressed as

The unknown Jacobi coefficients matrix of the multispan beam structure under arbitrary circular frequency (ω) excitation can be expressed as

$$\mathbf{Q} = (\mathbf{K} - \omega^2 \mathbf{M})^{-1} \mathbf{F}. \quad (17)$$

By substituting the results of the above equation into equations (14) and (15), the vibration characteristics of the multispan beam structure can be obtained.

3. Numerical Examples and Discussion

The general boundary conditions clamped, free, pinned, and sliding are denoted by first alphabet C, F, P, and S, respectively. Unless otherwise specified, in this study, the material properties and geometrical dimensions are as follows: $E = 210$ GPa, $\rho = 7800$ kg/m³, $\nu = 0.3$, $M = 8$, $\alpha = 0.5$, $\beta = 0.5$, $H = 4$; $L = 1$ m, $b = 0.04$ m, and $h = 0.02$ m. The nondimensional frequency is expressed as $\Omega = \sqrt{\omega L^2 \sqrt{\rho A / EI}}$.

3.1. Convergence and Validity Study. In this section, the fundamental purpose is to check the reliability and the convergence of the current method. The parameters of boundary springs and connective springs decide boundary constrain condition and continuity condition. As mentioned above, the domain decomposition technique is utilized in current method; therefore, the convergence of algorithmic program is betting on the amount of number of segments and Jacobi parameters.

Figure 3 exhibits the nondimensional frequency parameters of multispan beam structure with different boundary parameters. The boundary condition and continuity condition changing from free condition to clamped condition with the spring stiffness varies from 10^{-11} to 10^{11} . We can easily get that the stiffness values can be selected in the range of $10^8 \sim 10^{11}$ for clamped boundary condition and the stiffness value is obviously to choose

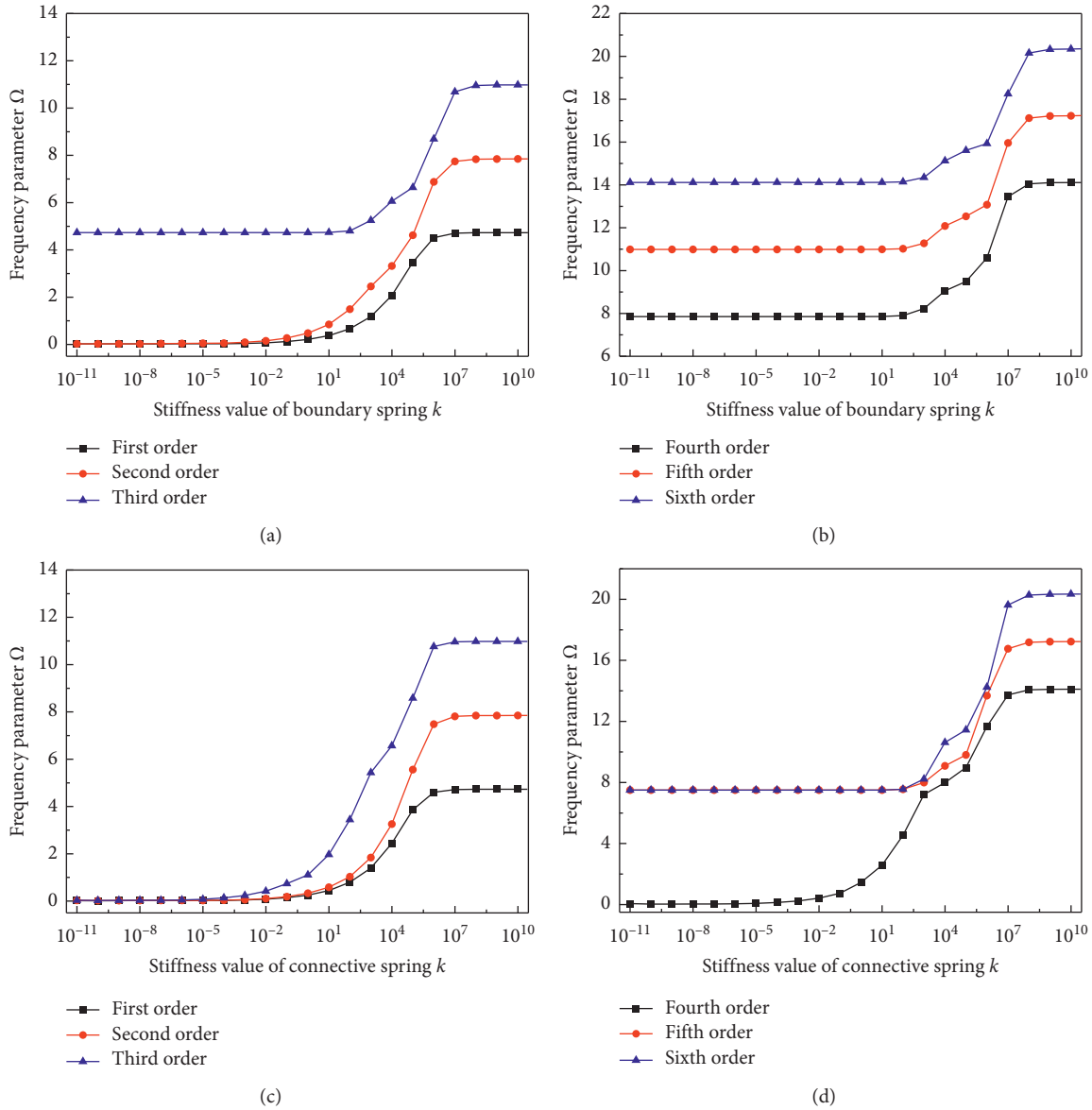


FIGURE 3: Frequency parameters Ω of multispan beam with different boundary parameters.

zero for free boundary condition. Whether it is a boundary spring or connective spring, it is apparently that the nondimensional frequency parameter increases rapidly with the spring value increasing in the range of $10^1 \sim 10^7$. As mentioned above, the connective spring stiffness is generally set to infinity to indicate the strong coupling between the two segments. Thus, all boundary conditions of multispan beam structure used in this paper are displayed in Table 1.

Figure 4 displays the variation of nondimensional results with number of segments. It is evident to see that the great convergence can be obtained when the number of segments no less than 3, which means that the high number of segments is not necessary. Therefore, the number of sections is chosen as 4 in this paper.

Next, convergence analysis of nondimensional frequency parameters Ω in relation to truncation terms of the

displacement functions is conducted to obtain the optimum solutions. The nondimensional frequency parameters Ω of multispan beam with different truncation are displayed in Figure 5. The results converge rapidly with the number of truncations of the Jacobi polynomial increasing, which is consistent with the pattern of the number of segments, and the results are stable when the truncation terms M reaches 4. If the truncation terms M is large, it will not only lead to an increase in computation, but also make the matrix pathological, so the polynomial truncation number is taken as 8 in this paper.

As stated previously, the Jacobi polynomial can be transformed into Legendre polynomials or Chebyshev polynomials by setting the values of two Jacobi parameters. Figure 6 demonstrates the relative percentage error of multispan beam with different Jacobi parameters, in which $\alpha = \beta = 0.5$ is selected as reference value. It is apparently that

TABLE 1: The spring stiffness values of the general edge conditions.

Boundary conditions	Transverse constraint spring k (N/m)	Rotation constraint spring K (Nm/rad)
F	0	0
S	0	10^{11}
P	10^{11}	0
C	10^{11}	10^{11}

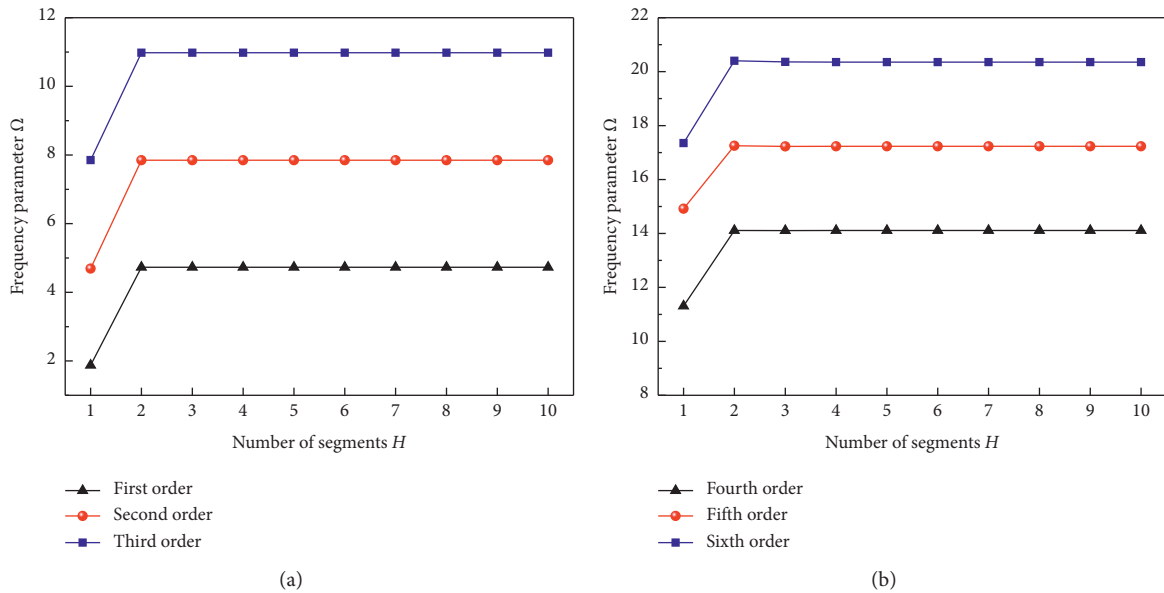


FIGURE 4: Frequency parameters Ω of multispan beam with different number of segments.

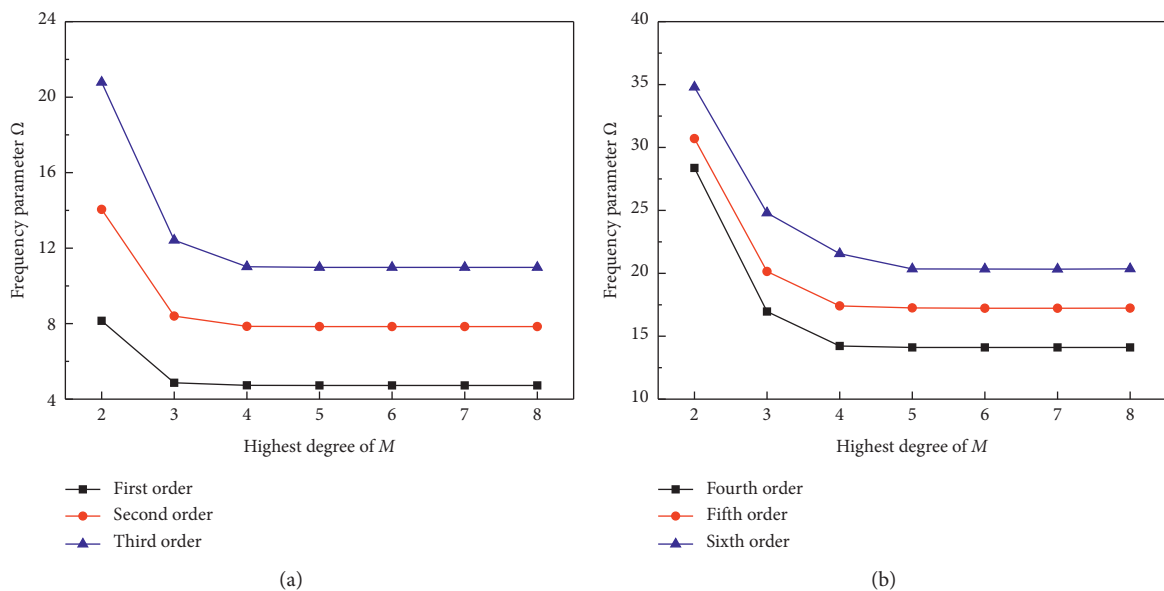


FIGURE 5: Frequency parameters Ω of multispan beam with different truncation.

the maximum relative percentage error is not more than 0.03% regardless of the value of α and β in the current methodology, and the problem can be solved by any of the orthogonal polynomials in Jacobi systems, which means that the choice of polynomial can be various.

3.2. *Free Vibration Behavior of a Multispan Beam.* Firstly, the reliability and accuracy of the present approach is studied in this section. For this purpose, free vibration solutions of multispan beam under general boundary restraints are compared with those from the FEM and literature. Table 2

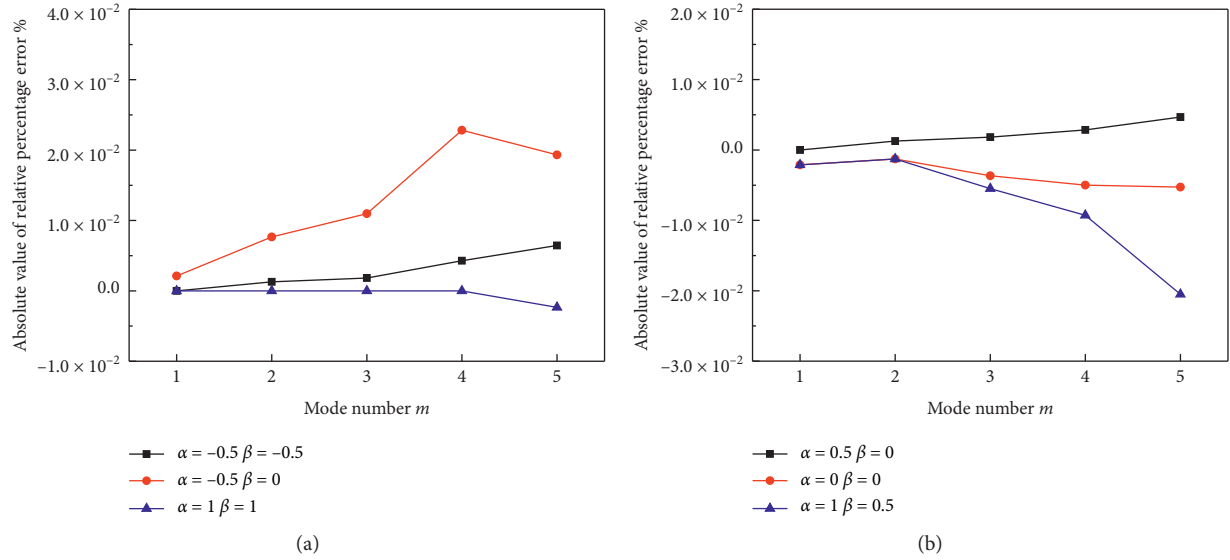


FIGURE 6: Relative percentage error of multispan beam with different Jacobi parameters.

TABLE 2: Comparison of frequency for multispan beam with different boundary condition ($k_t = 10^{11}$ N/m).

Boundary conditions	Mode no.	Single-span		Two-span		Four-span	
		FEM	Present	FEM	Present	FEM	Present
C-C $h = 0.02$ $b = 0.04$	1	106.38	106.38	292.21	292.21	864.87	864.88
	2	292.21	292.21	422.12	422.17	1147.60	1148.26
	3	570.15	570.17	936.88	936.97	1467.60	1469.73
	4	936.88	936.97	1147.60	1148.30	1636.60	1640.14
	5	1389.60	1389.85	1924.90	1925.77	3111.90	3120.22
S-S $h = 0.02$ $b = 0.08$	1	47.03	47.02	47.03	47.02	292.21	292.21
	2	187.73	187.72	106.38	106.38	311.43	311.46
	3	421.00	420.95	421.00	420.95	936.80	936.92
	4	745.05	744.91	570.12	570.14	1308.10	1309.00
	5	1157.40	1157.08	1157.40	1157.08	1924.60	1925.44

and Figure 7, respectively, exhibit the comparison of frequency and predicted mode shapes for multispan beam. It can be easily to find that the results of current approach are in great agreement with those obtained by FEM. The comparison of the nondimensional frequency parameters with published literature [44, 48] in different boundary condition is displayed in Table 3. It is clear that the present approach has great accuracy on the grounds of the comparison with FEM and published literature; we can get the conclusion that the present method has accurate precision to obtain the free vibration solutions of multispan beam.

Next, the influence of transverse constraint spring and rotation constraint spring on the vibration characteristics of multispan beam is discussed; the three-dimensional comparison graph of nondimensional frequency parameters Ω is shown in Figure 8. The multispan beam is fixed at one end and the transverse constraint spring and rotation constraint spring are, respectively, changed at the other end, from which the influence of both on the vibration characteristics of the multispan beam can be easily judged. The curvature of the graph does not change very much when transverse constraint spring is kept constant and rotation constraint

spring is gradually increasing; on the contrary, the curvature of the graph changes a lot when rotation constraint spring is kept constant and transverse constraint spring is gradually increasing. Therefore, it can be clear to find that the effect of the transverse constraint spring on the vibration characteristics of the structure is greater than that of the rotation constraint spring; in other words, the transverse constraint spring limits the displacement of the structure and has a greater effect on the stiffness of the structure.

Table 4 and Figure 9 present the nondimensional frequency parameters of multispan beam with different number of modes under various boundary conditions. It is apparent to see that the boundary restraints have an obvious effect on the vibration behaviors of multispan beam; the nondimensional frequency parameters gradually increase as the boundary condition is enhanced. In addition, the effect of the shear correction factor on the vibration characteristics of the multispan beam structure is also investigated. It is not hard to find that there is a slight tendency for the frequency parameter to increase with the shear correction factor increase; however, the effect is not significant. Figure 10 displays the frequency parameters Ω of multispan beam

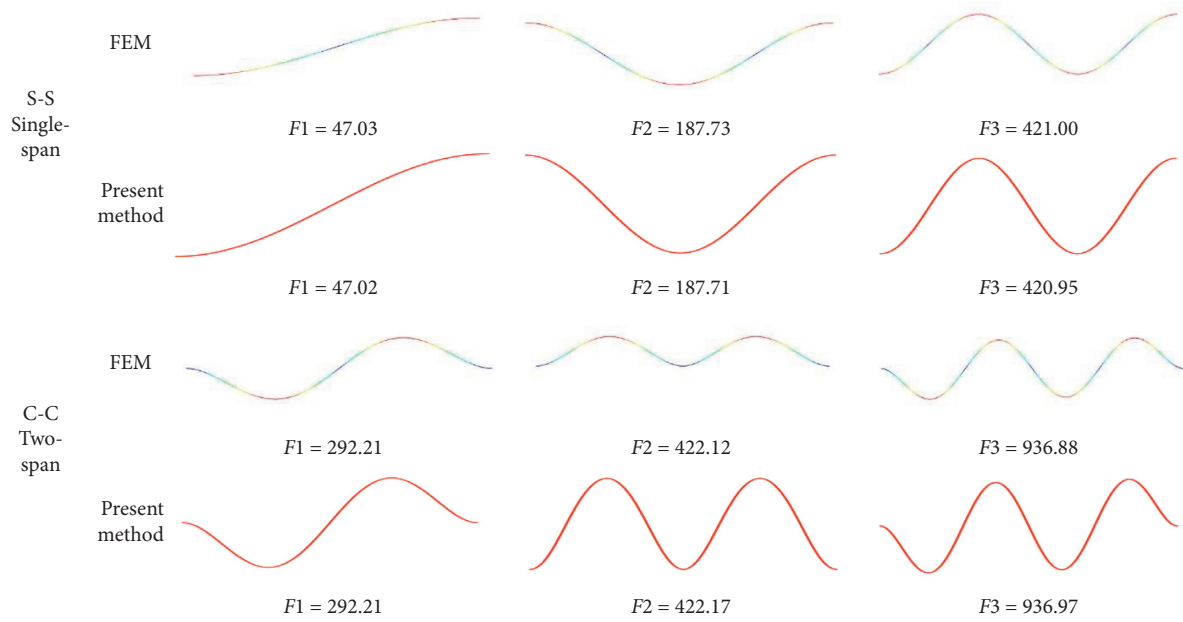


FIGURE 7: Comparison of the FEM and present method of predicted mode shapes for multispan beam.

TABLE 3: Comparison of the nondimensional frequency parameters with different boundary condition.

Boundary conditions	Mode no.	$h/L = 0.02$			$h/L = 0.05$			$h/L = 0.1$		
		Present	Ref [44]	Ref [48]	Present	Ref [44]	Ref [48]	Present	Ref [44]	Ref [48]
C-C	1	4.7236	4.7236	4.7235	4.6899	4.6904	4.6899	4.5777	4.5813	4.5796
	2	7.8285	7.8285	7.8281	7.7042	7.7052	7.7035	7.3274	7.3365	7.3312
	3	10.9352	10.9340	10.9340	10.6430	10.6430	10.6400	9.8530	9.8662	9.8561
	4	14.0173	14.0160	14.0150	13.4624	13.4670	13.4610	12.1196	12.1610	12.1450
	5	17.0718	17.0700	17.0680	16.1648	16.1690	16.1590	14.2114	14.2540	14.2320
	6	20.0941	20.0900	20.0870	18.7432	18.7460	18.7320	16.1259	16.1760	16.1490
P-P	1	3.1405	3.1405	3.1405	3.1349	3.1351	3.1349	3.1150	3.1159	3.1157
	2	6.2747	6.2748	6.2747	6.2307	6.2319	6.2314	6.0862	6.0925	6.0907
	3	9.3962	9.3966	9.3963	9.2534	9.2570	9.2554	8.8282	8.8456	8.8405
	4	12.4989	12.5000	12.4990	12.1741	12.1840	12.1810	11.3043	11.3520	11.3430
	5	15.5779	15.5790	15.5780	14.9849	14.9990	14.9930	13.5763	13.6280	13.6130
	6	18.6282	18.6300	18.6280	17.6688	17.6910	17.6810	15.6270	15.7000	15.6790

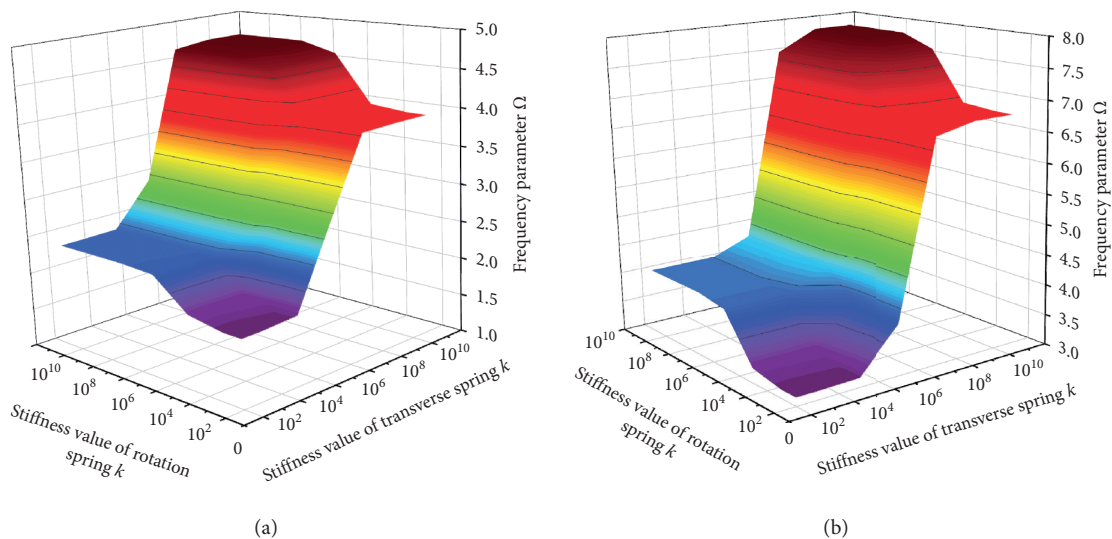


FIGURE 8: Comparison of frequency parameters Ω with transverse constraint spring and rotation constraint spring.

TABLE 4: Nondimensional frequency parameters of single-span beam with different number of modes under general boundary conditions.

	Mode no.	FC	PC	PP	CC	CS
$\kappa = 4/6$	1	1.8747	3.9228	3.1403	4.7221	2.364
	2	4.6880	7.05	6.2731	7.8232	5.4884
	3	7.8304	10.1587	9.3908	10.9228	8.6071
	4	10.9332	13.2424	12.4864	13.9936	11.7043
	5	14.0103	16.2955	15.554	17.0315	14.7733
	6	17.0555	19.3119	18.5878	20.0302	17.8088
$\kappa = 5/6$	1	1.8748	3.9235	3.1405	4.7236	2.3642
	2	4.6889	7.0532	6.2747	7.8285	5.4901
	3	7.8342	10.1673	9.3962	10.9352	8.6125
	4	10.9429	13.2601	12.4989	14.0173	11.7169
	5	14.0298	16.327	15.5779	17.0718	14.7973
	6	17.0896	19.3623	18.6282	20.0941	17.8495
$\kappa = 1$	1	1.8748	3.9239	3.1407	4.7246	2.3643
	2	4.6896	7.0553	6.2757	7.8321	5.4912
	3	7.8368	10.173	9.3997	10.9436	8.6161
	4	10.9494	13.2721	12.5072	14.0335	11.7254
	5	14.0429	16.3484	15.5938	17.0989	14.8134
	6	17.1125	19.3978	18.6553	20.1357	17.8764
$\kappa = 7/6$	1	1.8749	3.9243	3.1408	4.7253	2.3644
	2	4.6900	7.0568	6.2765	7.8347	5.4919
	3	7.8386	10.1771	9.4023	10.9497	8.6188
	4	10.9542	13.2808	12.5132	14.0454	11.7315
	5	14.0285	16.364	15.6055	17.119	14.8253
	6	17.1541	19.423	18.6766	20.1678	17.8963

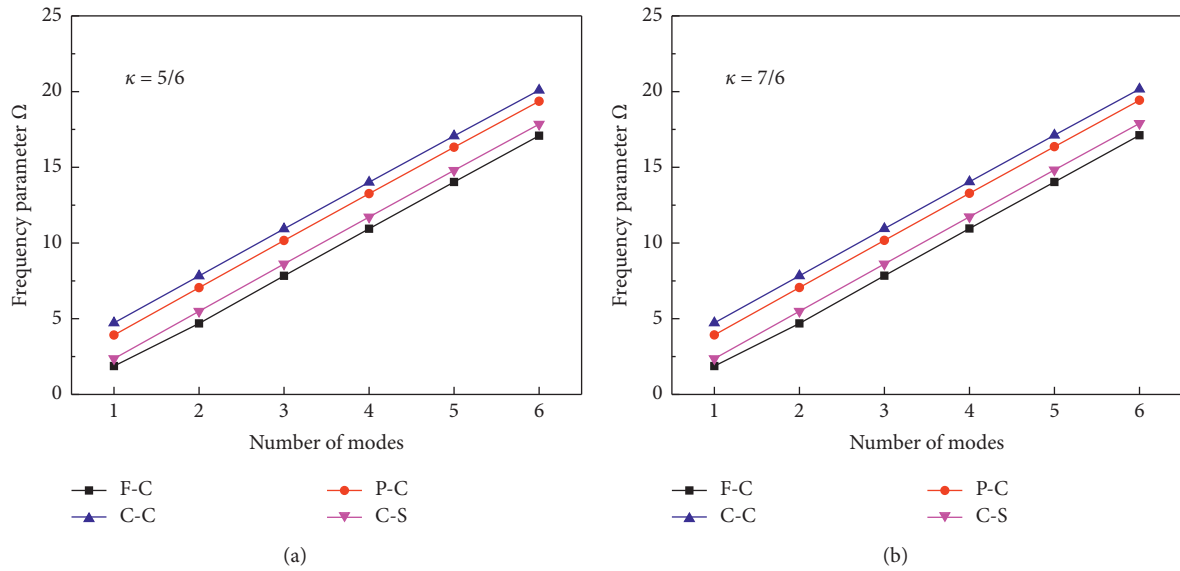


FIGURE 9: Frequency parameters Ω of multispan beam with different number of modes under various boundary conditions.

with different number of modes under various shear correction factors; as shown in Figure 10, the frequency parameters barely change with the increase of shear correction factor, and only a slight increasing trend can be seen.

As shown in Table 3, h/L ratio seems to have little effect on the nondimensional frequency. Therefore, the natural frequency of single-span beam under general boundary restraints with different h/L ratio is shown in Table 5 and Figure 11, where five different kinds of h/L are included. The consequence can be drawn that the natural frequency

increases significantly with the increase of h/L ratio; that is, the increase of the thickness of the structure increases the structural stiffness to a greater extent.

Tables 6 and 7 and Figures 12 and 13, respectively, display the nondimensional frequency parameters of multispan beam subject to general boundary conditions with different numbers and stiffness of supporting springs. Unsurprisingly, we can clearly get that the nondimensional frequency parameters gradually increase with the numbers and stiffness of supporting springs increasing. That is to say,

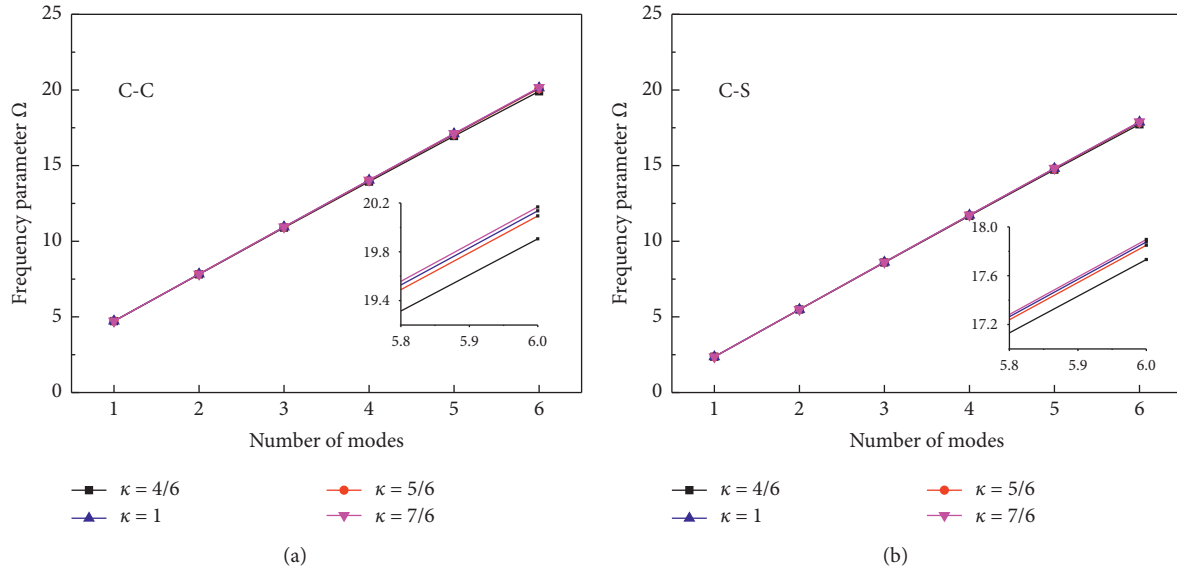


FIGURE 10: Frequency parameters Ω of multispan beam with different number of modes under various shear correction factor.

TABLE 5: Natural frequency of single-span beam subject to general boundary conditions with different h/L ratios.

Boundary conditions	h/L	Mode no.				
		1	2	3	4	5
F-C	0.01	8.38	52.50	146.89	287.53	474.63
	0.02	16.76	104.83	292.63	570.96	938.57
	0.03	25.13	156.82	436.23	846.86	1383.26
	0.04	33.48	208.28	576.37	1110.92	1798.82
	0.05	41.83	259.09	712.53	1362.06	2184.14
P-C	0.01	36.74	118.98	248.00	423.52	645.19
	0.02	73.39	237.19	492.89	838.41	1271.13
	0.03	109.88	353.94	732.04	1237.71	1863.04
	0.04	146.09	468.33	962.11	1613.08	2405.39
	0.05	181.97	579.98	1182.11	1963.32	2898.18
P-P	0.01	23.52	94.05	211.43	375.44	585.75
	0.02	47.02	187.72	420.95	744.88	1157.42
	0.03	70.48	280.63	626.73	1102.85	1701.73
	0.04	93.86	372.43	827.15	1444.85	2210.23
	0.05	117.14	462.79	1020.84	1767.64	2677.90
C-C	0.01	53.30	146.79	287.43	474.43	707.46
	0.02	106.38	292.21	570.17	936.97	1389.85
	0.03	159.05	435.09	844.45	1378.74	2029.52
	0.04	211.04	573.77	1104.97	1787.17	2604.57
	0.05	262.23	707.81	1351.21	2163.57	3120.54
C-S	0.01	13.33	72.01	177.66	329.96	528.66
	0.02	26.65	143.71	353.66	654.58	1044.07
	0.03	39.94	214.82	526.52	969.26	1535.79
	0.04	53.19	285.03	694.60	1269.10	1992.79
	0.05	66.38	354.11	856.97	1552.28	2413.41

the increase in the numbers and stiffness of supporting springs leads to an increase in the stiffness of the multispan beam structure.

3.3. *Forced Vibration Behavior of a Multispan Beam.* The multispan beam may be subjected to external excitation loads in engineering applications, and this section

conducted forced vibration analysis for the multispan beam. The excitation load is a unit concentrated force in the downward direction, located at the middle of the beam, the analysis frequency band is 2–1000 Hz with the interval being 2 Hz.

In order to verify the accuracy of current methodology for forced vibration of multispan beam, the comparison of the FEM and present approach of forced

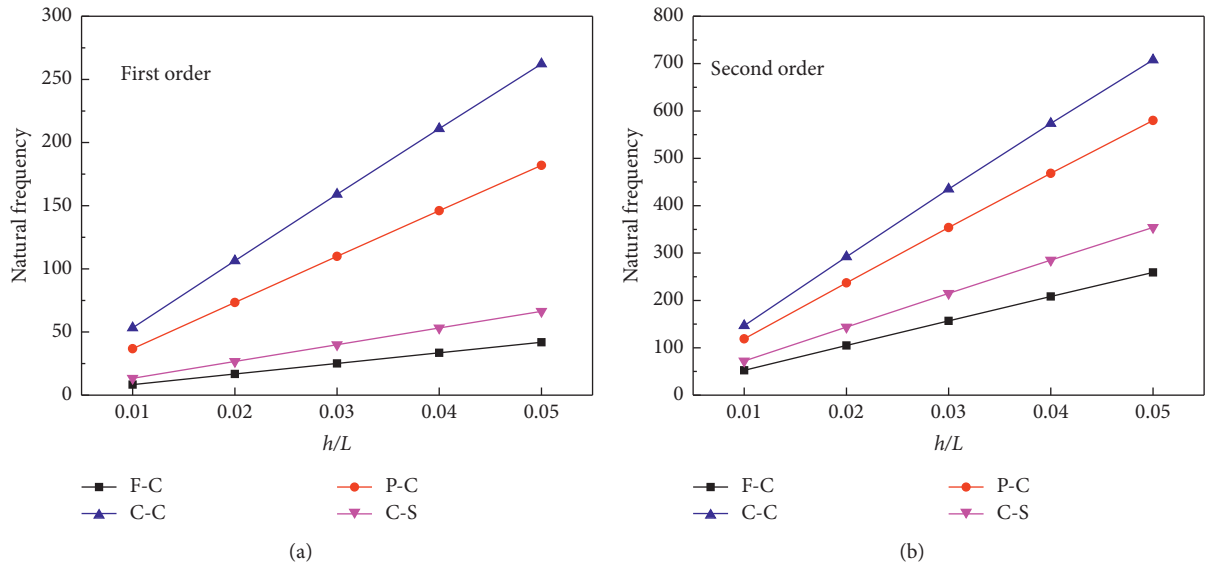


FIGURE 11: Frequency parameters Ω of single-span beam with different h/L ratios.

TABLE 6: Nondimensional frequency parameters of multispan beam subject to general boundary conditions with different numbers of supporting springs.

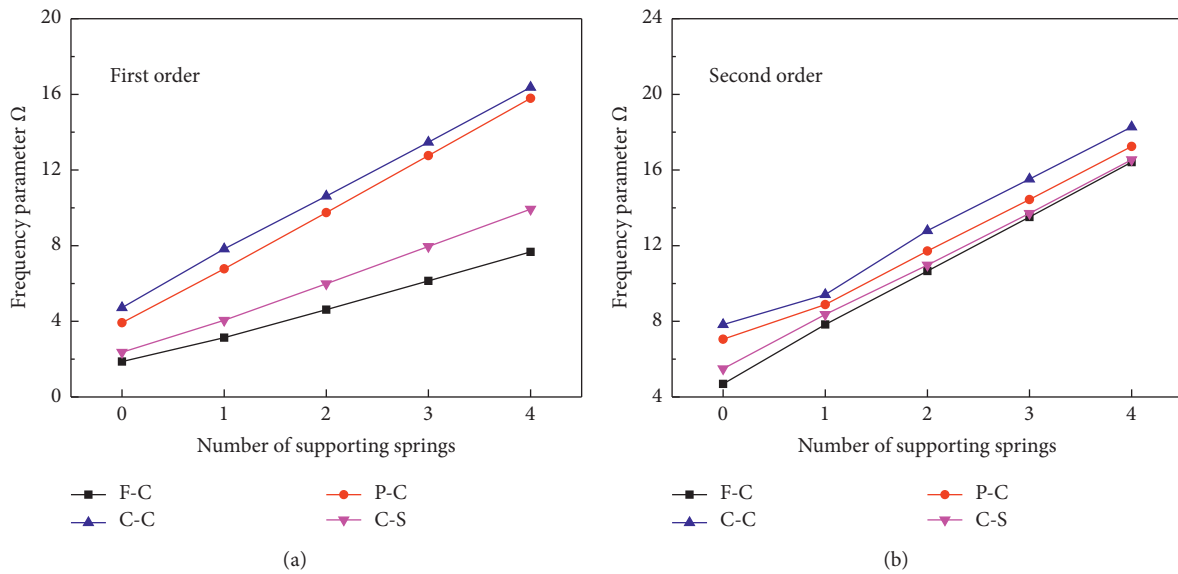
Boundary conditions	Number of supporting springs	Mode no.				
		1	2	3	4	5
F-C	0	1.8748	4.6889	7.8342	10.9429	14.0298
	1	3.1390	7.8330	9.3792	14.0303	15.5353
	2	4.6184	10.6594	12.7664	14.0642	19.8544
	3	6.1401	13.5133	15.5344	17.5290	18.5285
	4	7.6686	16.4144	18.3171	20.4367	22.2501
P-C	0	3.9235	7.0532	10.1673	13.2601	16.3270
	1	6.7730	8.8871	13.0061	15.0232	19.1158
	2	9.7470	11.7167	13.7094	18.9990	20.9373
	3	12.7626	14.4393	16.5925	18.2721	24.9088
	4	15.7912	17.2493	19.3532	21.4813	22.9936
P-P	0	3.1405	6.2747	9.3962	12.4989	15.5779
	1	6.2747	7.8286	12.4991	14.0177	18.6297
	2	9.3962	10.6206	12.8273	18.6279	19.8906
	3	12.4991	13.4679	15.5182	17.5560	24.6486
	4	15.5781	16.3927	18.2606	20.4574	22.4309
C-C	0	4.7236	7.8285	10.9352	14.0173	17.0718
	1	7.8287	9.4098	14.0185	15.5191	20.0975
	2	10.6181	12.7926	14.0823	19.8445	21.8922
	3	13.4684	15.5188	17.5573	18.5473	25.5818
	4	16.3748	18.2761	20.4392	22.2724	23.2536
C-S	0	2.3642	5.4901	8.6125	11.7169	14.7973
	1	4.0545	8.3659	10.4255	14.5283	16.5663
	2	5.9861	10.9737	13.3968	15.4543	20.1807
	3	7.9553	13.7077	15.9991	18.1054	20.3568
	4	9.9302	16.5455	18.6778	20.9984	22.8912

vibration response for multispan beam is shown in Figure 14. It is apparent to find that the current method agrees well with the FEM results; the curve trend of the two is basically the same, with only little deviation at the individual peak. That is to say, the present method can effectively analyze the forced vibration characteristics for multispan beam.

Having validated the correctness of the current method for forced vibration analysis of multispan beam, parametric investigations are conducted to analyze the steady-state vibration behaviors. Firstly, Figure 15 displays the comparison of the forced vibration response of multispan beam with different boundary conditions. The results reveal that the boundary conditions have a significant effect on the

TABLE 7: Nondimensional frequency parameters of two-span beam subject to general boundary conditions with different stiffness of supporting springs.

Boundary conditions	Stiffness of supporting spring (N/m)	Mode no.				
		1	2	3	4	5
F-C	0	1.8748	4.6889	7.8343	10.9431	14.0304
	10^2	1.8751	4.6890	7.8343	10.9431	14.0305
	10^5	2.1139	4.7758	7.8343	10.9499	14.0305
	10^8	3.1332	7.8328	9.1911	14.0302	14.5828
	10^{11}	3.1390	7.8330	9.3792	14.0303	15.5353
P-C	0	3.9235	7.0533	10.1675	13.2607	16.3281
	10^2	3.9236	7.0533	10.1675	13.2608	16.3281
	10^5	4.0685	7.0574	10.1747	13.2613	16.3298
	10^8	6.7572	8.765	12.8592	14.366	18.2301
	10^{11}	6.773	8.8871	13.0061	15.0232	19.1158
P-P	0	3.1405	6.2747	9.3962	12.4991	15.5784
	10^2	3.1408	6.2747	9.3963	12.4991	15.5783
	10^5	3.3946	6.2747	9.407	12.4991	15.5798
	10^8	6.2747	7.7204	12.4991	13.3361	18.0186
	10^{11}	6.2747	7.8286	12.4991	14.0177	18.6297
C-C	0	4.7236	7.8287	10.9356	14.0185	17.0735
	10^2	4.7237	7.8287	10.9356	14.0187	17.0736
	10^5	4.8265	7.8287	10.9423	14.0185	17.0753
	10^8	7.8287	9.2265	14.0185	14.5694	19.108
	10^{11}	7.8287	9.4098	14.0185	15.5191	20.0975
C-S	0	2.3642	5.4901	8.6126	11.7171	14.7979
	10^2	2.3645	5.4902	8.6126	11.7171	14.7981
	10^5	2.5757	5.5406	8.6146	11.7218	14.7984
	10^8	4.0427	8.3378	10.2199	14.2822	15.7002
	10^{11}	4.0545	8.3659	10.4255	14.5283	16.5663

FIGURE 12: Frequency parameters Ω of multispan beam with different numbers of supporting springs.

structural forced vibration response; the first peak frequency of the structural forced response gradually increases with the enhancement of the boundary stiffness, while the number of peaks decreases. At the same time, it is not hard to find that the peak of the forced response corresponds to the natural frequency of the structure.

Next, the purpose of this section is to explore the influence of beam structural parameters on forced vibration. Figure 16 exhibits the comparison of the forced vibration response of multispan beam with different h/L ratios. The results demonstrate that the stiffness increases and the natural frequency increases as the thickness of the structure

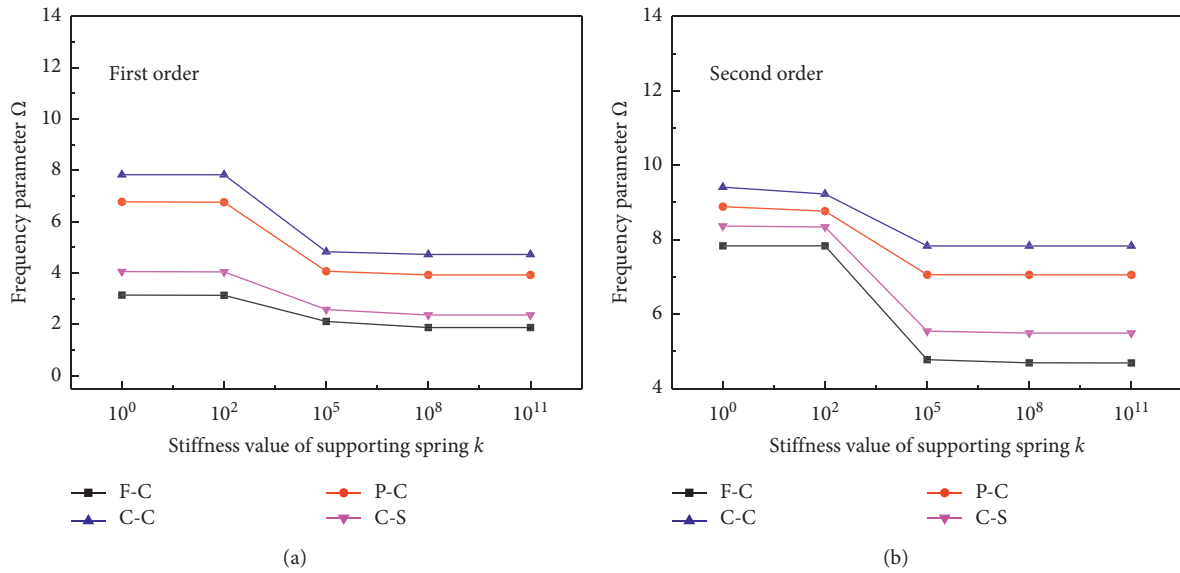


FIGURE 13: Frequency parameters Ω of two-span beam with different stiffness of supporting springs.

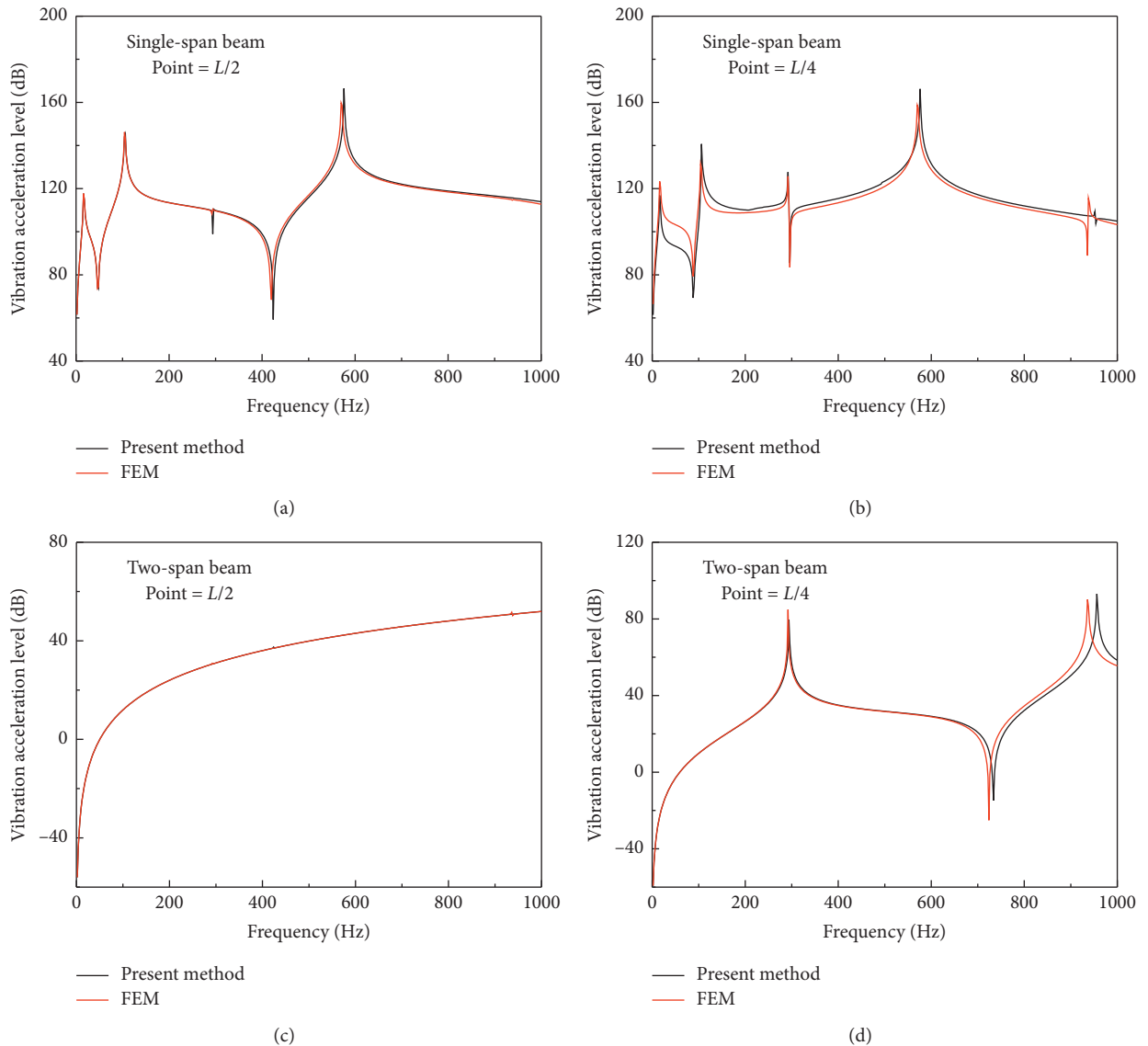


FIGURE 14: Comparison of the FEM and present method of forced vibration response for multispan beam.

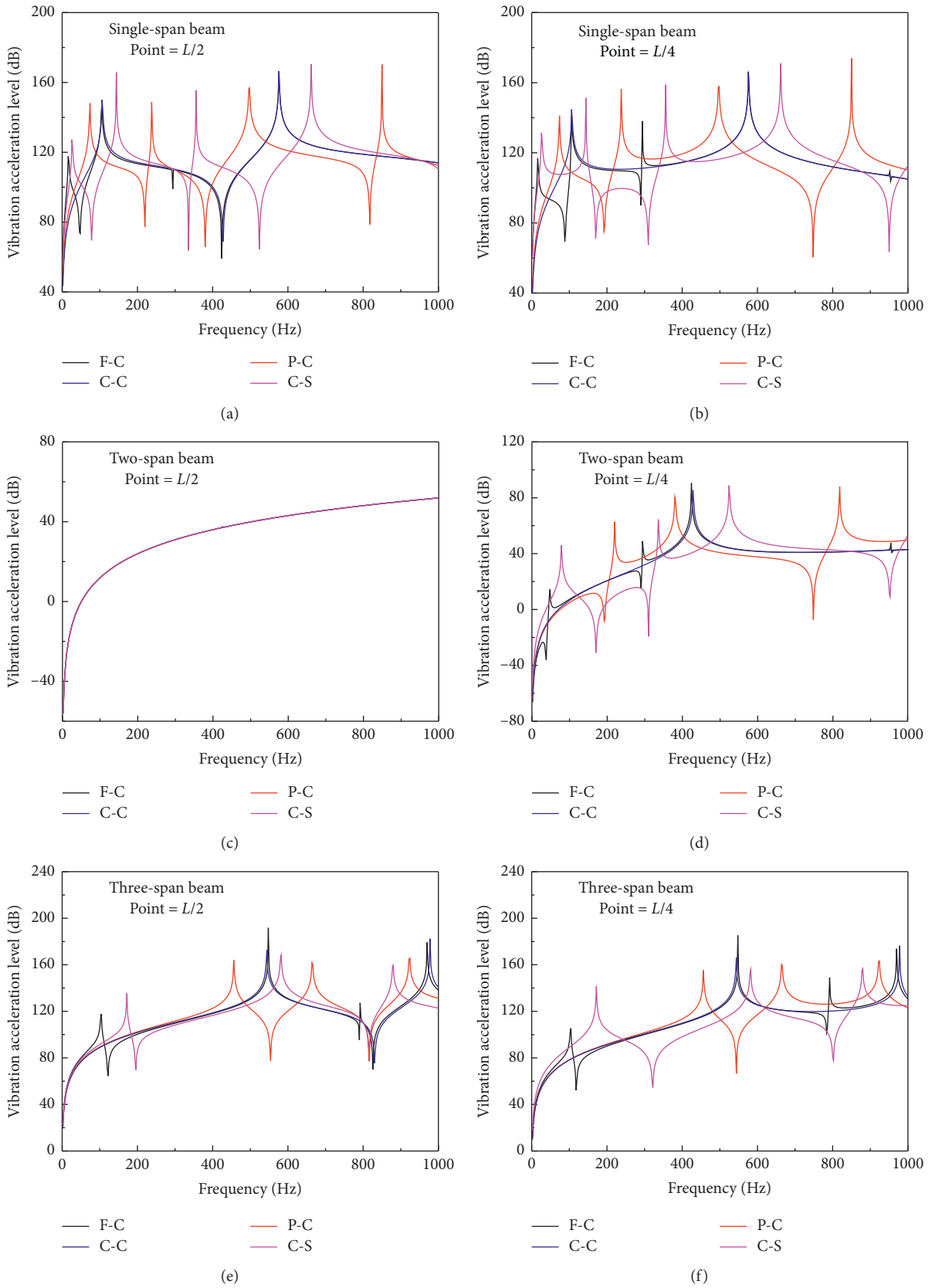


FIGURE 15: Comparison of the forced vibration response of multispan beam with different boundary conditions.

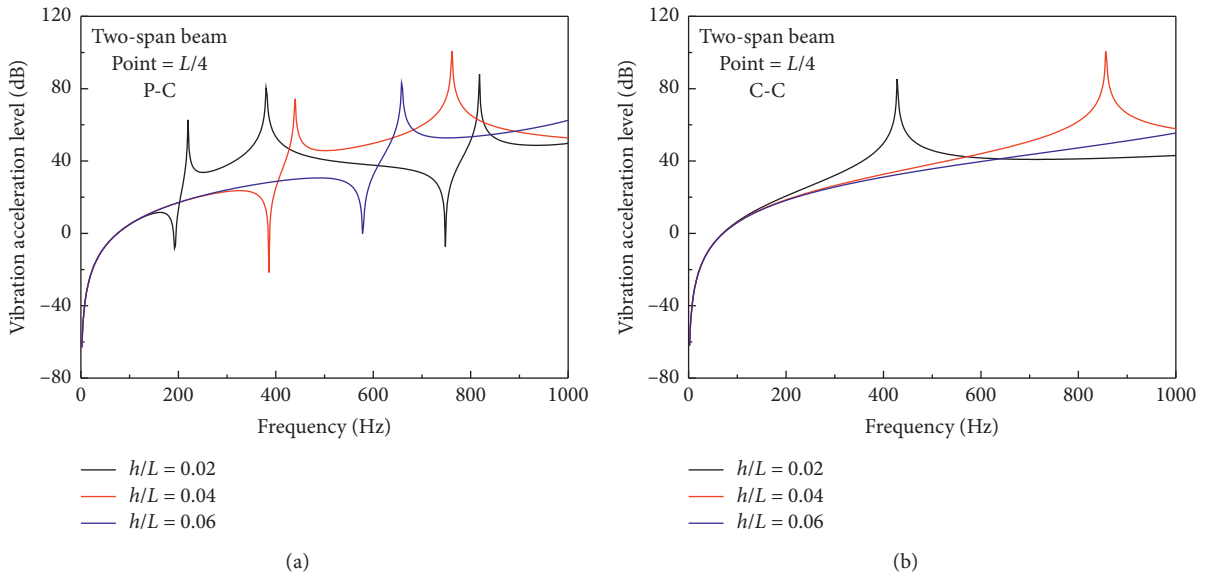


FIGURE 16: Comparison of the forced vibration response of multispan beam with different h/L ratios.

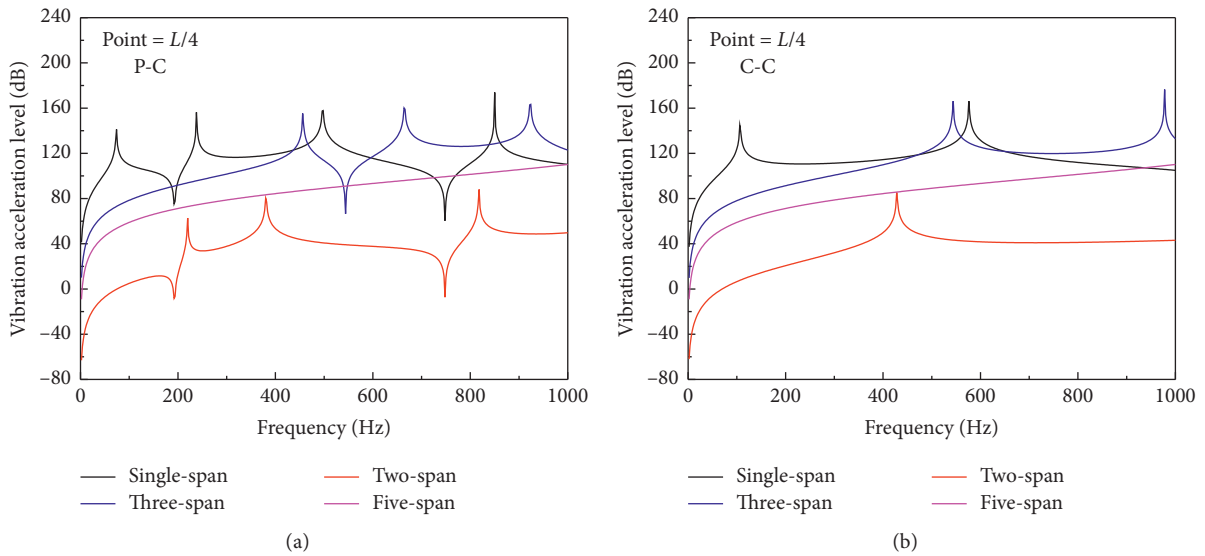


FIGURE 17: Comparison of the forced vibration response of multispan beam with different numbers of supporting springs.

increases, the number of forced vibration response peaks decreases in the low-frequency band, while the magnitude increases.

Lastly, Figures 17 and 18, respectively, display the comparison of the forced vibration response of multispan beam with different numbers and stiffness of supporting

springs. It is indicated that the peak frequency shifts to the right with the numbers and stiffness of support springs increases, while the numbers of vibration response peaks decrease. At the same time, it can also be found that the response gradually decreases with the spring stiffness increases.

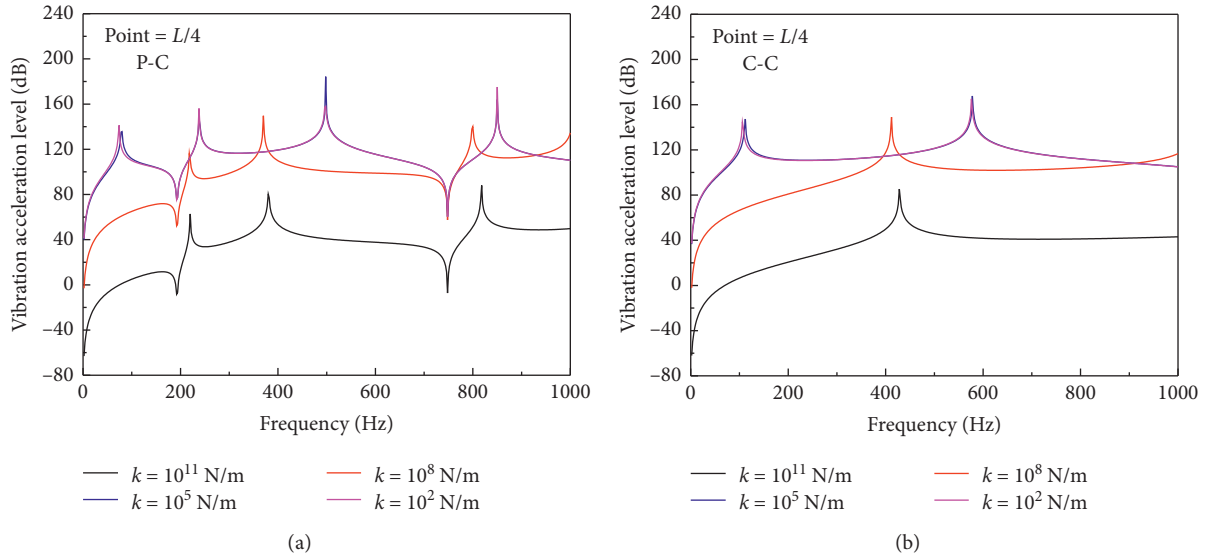


FIGURE 18: Comparison of the forced vibration response of two-span beam with different stiffness of supporting springs.

4. Conclusions

The free and forced vibration response of a multispan Timoshenko beam with different boundary restraints are studied by using the Ritz method in this paper. The domain decomposition approach is used to divide the structure to several equal sections, and two groups of springs (transversal displacement spring and rotational spring) are used to simulate different boundary restraints and continuity condition of the structure. In addition, several transversal displacement springs are arranged on the structure to represent the intermediate elastic support. Finally, the admissible displacement functions are expanded through Jacobi orthogonal polynomials, and the free and forced vibration characteristics of multispan beam structures can be obtained by using the Rayleigh–Ritz method. The accuracy of the current approach has been verified by comparing the results with existing literatures and FEM. The effects of transverse constraints spring and rotating constraints spring on the vibration characteristics of the structure are explored, which clearly shows that the effect of the transverse constraint spring on the vibration characteristics of the structure is greater than that of the rotation constraint spring. Besides this, results for various boundary conditions, ratios of h/L , numbers, and stiffness of supporting springs are presented, which shows that the geometric dimensions and restraint conditions have obvious influence on free and forced vibration characteristics of multispan beam. However, the paper only studies the free vibration and steady vibration of the continuous beam structure, which lacks the research on the transient vibration. At the same time, it needs to be studied for the more complex plate and shell structure, which will be the focus research of the future directions. In general, the research in this paper can be used as an extended application of Jacobi–Ritz method, and the research results of the paper can provide data support for engineers to conduct the structural design of infrastructure.

Data Availability

The data used to support the findings of this study are included within the article.

Conflicts of Interest

The authors declare that there are no conflicts of interest regarding the publication of this paper.

Acknowledgments

This study was funded by the National Natural Science Foundation of China (U2006229), National Key Research and Development Program (2016YFC0303406), Key Research and Development Program of Shandong Province (2019JZZY010125, 2020CXGC010701, and 2020CXGC010702), Ph.D. Student Research and Innovation Fund of the Fundamental Research Funds for the Central Universities (3072020GIP0102), Natural Basic Research Project of China (2019414C003), and Southern Marine Science and Engineering Guangdong Laboratory (Zhuhai) (311021013).

References

- [1] A. Palatini and S. Timoshenko, *Vibration Problems in Engineering*, Wiley, Hoboken, NJ, USA, 1930.
- [2] K. Torabi, M. Ghassabi, M. Heidari-Rarani et al., “Variational iteration method for free vibration analysis of a Timoshenko beam under various boundary conditions,” *International Journal of Engineering*, vol. 30, no. 10, pp. 1565–1572, 2017.
- [3] Y. C. Liu and C. S. Gurrum, “The use of He’s variational iteration method for obtaining the free vibration of an Euler-Bernoulli beam,” *Mathematical and Computer Modelling*, vol. 50, no. 11–12, pp. 1545–1552, 2009.
- [4] D. V. Bambill, C. A. Rossit, R. E. Rossi, D. H. Felix, and A. R. Ratazzi, “Transverse free vibration of non uniform rotating Timoshenko beams with elastically clamped

- boundary conditions,” *Meccanica*, vol. 48, no. 6, pp. 1289–1311, 2013.
- [5] M. Mohandes and A. R. Ghasemi, “Modified couple stress theory and finite strain assumption for nonlinear free vibration and bending of micro/nanolaminated composite Euler-Bernoulli beam under thermal loading,” *Proceedings of the Institution of Mechanical Engineers-Part C: Journal of Mechanical Engineering Science*, vol. 231, no. 21, pp. 4044–4056, 2017.
- [6] M. Boiangiu, V. Ceausu, and C. D. Untaroiu, “A transfer matrix method for free vibration analysis of Euler-Bernoulli beams with variable cross section,” *Journal of Vibration and Control*, vol. 22, no. 11, pp. 2591–2602, 2016.
- [7] Y. Kiani, “Analysis of FG-CNT reinforced composite conical panel subjected to moving load using Ritz method,” *Thin-Walled Structures*, vol. 119, pp. 47–57, 2017.
- [8] Y. Kiani and M. Mirzaei, “Rectangular and skew shear buckling of FG-CNT reinforced composite skew plates using Ritz method,” *Aerospace Science and Technology*, vol. 77, pp. 388–398, 2018.
- [9] F. Z. Pang, H. C. Li, H. L. Chen, and Y. Shan, “Free vibration analysis of combined composite laminated cylindrical and spherical shells with arbitrary boundary conditions,” *Mechanics of Advanced Materials and Structures*, vol. 28, pp. 1–18, 2019.
- [10] H. Li, F. Z. Pang, X. H. Miao, and Y. H. Li, “Jacobi-Ritz method for free vibration analysis of uniform and stepped circular cylindrical shells with arbitrary boundary conditions: a unified formulation,” *Computers & Mathematics with Applications*, vol. 77, no. 7, pp. 427–440, 2019.
- [11] F. Pang, H. Li, X. Wang, X. Miao, and S. Li, “A semi analytical method for the free vibration of doubly-curved shells of revolution,” *Computers & Mathematics with Applications*, vol. 75, no. 9, pp. 3249–3268, 2018.
- [12] L.-l. Jing, P.-j. Ming, W.-p. Zhang, L.-r. Fu, and Y.-p. Cao, “Static and free vibration analysis of functionally graded beams by combination Timoshenko theory and finite volume method,” *Composite Structures*, vol. 138, pp. 192–213, 2016.
- [13] R. Balamuralikrishnan and R. J. Saravanan, “Effect of addition of alccofine on the compressive strength of cement mortar cubes,” *Emerging Science Journal*, vol. 5, no. 2, pp. 155–170, 2021.
- [14] F. Rahmani, R. Kamgar, and R. Rahgozar, “Finite element analysis of functionally graded beams using different beam theories,” *Civil Engineering Journal*, vol. 6, no. 11, pp. 2086–2102, 2020.
- [15] P. Rahgozar, “Free vibration of tall buildings using energy method and Hamilton’s principle,” *Civil Engineering Journal*, vol. 6, no. 5, pp. 945–953, 2020.
- [16] Z. Chen, Z. Yang, N. Guo, and G. Zhang, “An energy finite element method for high frequency vibration analysis of beams with axial force,” *Applied Mathematical Modelling*, vol. 61, pp. 521–539, 2018.
- [17] S. Sinir, M. Cevik, and B. G. Sinir, “Nonlinear free and forced vibration analyses of axially functionally graded Euler-Bernoulli beams with non-uniform cross-section,” *Composites Part B: Engineering*, vol. 148, pp. 123–131, 2018.
- [18] S. D. Akbas, “Forced vibration responses of axially functionally graded beams by using Ritz method,” *Journal of Applied and Computational Mechanics*, vol. 7, no. 1, pp. 109–115, 2021.
- [19] H. J. Xiang and J. Yang, “Free and forced vibration of a laminated FGM Timoshenko beam of variable thickness under heat conduction,” *Composites Part B: Engineering*, vol. 39, no. 2, pp. 292–303, 2008.
- [20] Z. Wu and W. J. Chen, “Free and forced vibration of laminated composite beams,” *AIAA Journal*, vol. 56, no. 7, pp. 2877–2886, 2018.
- [21] R. Damghanian, K. Asemi, and M. Babaei, “A new beam element for static, free and forced vibration responses of microbeams resting on viscoelastic foundation based on modified couple stress and third-order beam theories,” *Iranian Journal of Science and Technology-Transactions of Mechanical Engineering*, 2020.
- [22] A. Paul and D. Das, “Non-linear forced vibration analysis of higher-order shear-deformable functionally graded material beam in thermal environment subjected to harmonic excitation and resting on non-linear elastic foundation,” *The Journal of Strain Analysis for Engineering Design*, vol. 53, no. 6, pp. 446–462, 2018.
- [23] H. Y. Lv and Y. M. Zhang, “A wave-based vibration analysis of a finite Timoshenko locally resonant beam suspended with periodic uncoupled force-moment type resonators,” *Crystals*, vol. 10, no. 12, 2020.
- [24] B. Qin, R. Zhong, Q. Wang, and X. Zhao, “A Jacobi-Ritz approach for FGP beams with arbitrary boundary conditions based on a higher-order shear deformation theory,” *Composite Structures*, vol. 247, Article ID 112435, 2020.
- [25] Z. Su, G. Y. Jin, and T. G. Ye, “Vibration analysis and transient response of a functionally graded piezoelectric curved beam with general boundary conditions,” *Smart Materials and Structures*, vol. 25, no. 6, 2016.
- [26] C. Johansson, C. Pacoste, and R. Karoumi, “Closed-form solution for the mode superposition analysis of the vibration in multi-span beam bridges caused by concentrated moving loads,” *Computers & Structures*, vol. 119, pp. 85–94, 2013.
- [27] H. Fakhreddine, A. Adri, S. Rifai, and R. Benamar, “Geometrically nonlinear free and forced vibrations of Euler-Bernoulli multi-span beams,” in *Proceedings of the 14th International Conference on Vibration Engineering and Technology of Machinery (Vetomac Xiv)*, vol. 211, Lisbon, Portugal, September 2018.
- [28] A. Ghannadial and S. Khodapanah Ajirlou, “Forced vibration of multi-span cracked Euler-Bernoulli beams using dynamic Green function formulation,” *Applied Acoustics*, vol. 148, pp. 484–494, 2019.
- [29] G. Chen, X. Zeng, X. Liu, and X. Rui, “Transfer matrix method for the free and forced vibration analyses of multi-step Timoshenko beams coupled with rigid bodies on springs,” *Applied Mathematical Modelling*, vol. 87, pp. 152–170, 2020.
- [30] H. P. Lin and S. C. Chang, “Free vibration analysis of multi-span beams with intermediate flexible constraints,” *Journal of Sound and Vibration*, vol. 281, no. 1-2, pp. 155–169, 2005.
- [31] H. B. Liu, H. H. Nguyen, and Y. M. Xiang, “Vibration analysis of a multi-span continuous beam with cracks,” *Advances in Civil Engineering*, vol. 256–259, no. 1–4, pp. 964–972, 2013.
- [32] J. Lee, “Free vibration analysis of circularly curved multi-span Timoshenko beams by the pseudospectral method,” *Journal of Mechanical Science and Technology*, vol. 21, no. 12, pp. 2066–2072, 2007.
- [33] T. V. Lien, N. T. Duc, and N. T. Khiem, “Free and forced vibration analysis of multiple cracked FGM multi span continuous beams using dynamic stiffness method,” *Latin American Journal of Solids and Structures*, vol. 16, no. 2, 2019.
- [34] X. H. Lv, D. Y. Shi, Q. S. Wang et al., “A unified solution for the in-plane vibration analysis of multi-span curved Timoshenko beams with general elastic boundary and coupling conditions,” *Journal of Vibroengineering*, vol. 18, no. 2, pp. 1071–1087, 2016.

- [35] Y. Yesilce, "Free and forced vibrations of an axially-loaded Timoshenko multi-span beam carrying a number of various concentrated elements," *Shock and Vibration*, vol. 19, no. 4, pp. 735–752, 2012.
- [36] Y. Yesilce and O. Demirdag, "Effect of axial force on free vibration of Timoshenko multi-span beam carrying multiple spring-mass systems," *International Journal of Mechanical Sciences*, vol. 50, no. 6, pp. 995–1003, 2008.
- [37] Y. Yesilce, O. Demirdag, and S. Catal, "Free vibrations of a multi-span Timoshenko beam carrying multiple spring-mass systems," *Sadhana*, vol. 33, no. 4, pp. 385–401, 2008.
- [38] Z. Zhao, S. Wen, and F. Li, "Vibration analysis of multi-span lattice sandwich beams using the assumed mode method," *Composite Structures*, vol. 185, pp. 716–727, 2018.
- [39] Z. Zhao, S. Wen, F. Li, and C. Zhang, "Free vibration analysis of multi-span Timoshenko beams using the assumed mode method," *Archive of Applied Mechanics*, vol. 88, no. 7, pp. 1213–1228, 2018.
- [40] H.-Y. Lin and Y.-C. Tsai, "Free vibration analysis of a uniform multi-span beam carrying multiple spring-mass systems," *Journal of Sound and Vibration*, vol. 302, no. 3, pp. 442–456, 2007.
- [41] Y. Yesilce, "Effect of axial force on the free vibration of reddy-bickford multi-span beam carrying multiple spring-mass systems," *Journal of Vibration and Control*, vol. 16, no. 1, pp. 11–32, 2010.
- [42] Y. Yesilce, "Free vibrations of a Reddy-Bickford multi-span beam carrying multiple spring-mass systems," *Shock and Vibration*, vol. 18, no. 5, pp. 709–726, 2011.
- [43] F. Z. Pang, C. Gao, J. Cui, Y. Ren, H. Li, and H. C. Wang, "A semianalytical approach for free vibration characteristics of functionally graded spherical shell based on first-order shear deformation theory," *Shock and Vibration*, vol. 2019, Article ID 7352901, 18 pages, 2019.
- [44] D. Shi, Q. Wang, X. Shi et al., "An accurate solution method for the vibration analysis of Timoshenko beams with general elastic supports," *Journal of Mechanical Engineering Science*, vol. 203–210, pp. 418–424, 2014.
- [45] Q. Wang, K. Choe, J. Tang et al., "Vibration analyses of general thin and moderately thick laminated composite curved beams with variable curvatures and general boundary conditions," *Mechanics of Advanced Materials & Structures*, vol. 27, pp. 1–15, 2019.
- [46] F. Pang, H. Li, J. Cui, Y. Du, and C. Gao, "Application of flügge thin shell theory to the solution of free vibration behaviors for spherical-cylindrical-spherical shell: a unified formulation," *European Journal of Mechanics—A: Solids*, vol. 74, pp. 381–393, 2019.
- [47] H. Li, F. Pang, and H. Chen, "A semi-analytical approach to analyze vibration characteristics of uniform and stepped annular-spherical shells with general boundary conditions," *European Journal of Mechanics—A: Solids*, vol. 74, pp. 48–65, 2019.
- [48] M. e. S. Sari and E. A. Butcher, "Free vibration analysis of non-rotating and rotating Timoshenko beams with damaged boundaries using the Chebyshev collocation method," *International Journal of Mechanical Sciences*, vol. 60, no. 1, pp. 1–11, 2012.

Research Article

Investigating the Effect of Viscous Yield Dampers on Concrete Structure Performance

Nima Marzban ¹ and Parisa Esmaeiltabar Nesheli²

¹Department of Civil Engineering, Tabari Non-Profit Higher Education Institute, Babol, Iran

²Department of Civil Engineering, Babol University of Technology, Babol, Iran

Correspondence should be addressed to Nima Marzban; nima.marzban@tabari.ac.ir

Received 30 April 2021; Revised 1 June 2021; Accepted 23 June 2021; Published 12 July 2021

Academic Editor: S. Mahdi S. Kolbadi

Copyright © 2021 Nima Marzban and Parisa Esmaeiltabar nesheli. This is an open access article distributed under the Creative Commons Attribution License, which permits unrestricted use, distribution, and reproduction in any medium, provided the original work is properly cited.

Viscous dampers are one of the most effective devices in the energy consumption of the buildings. The passive hybrid system progressive applications cause each of the dampers to compensate for the weakness of the other system, thus increasing the efficiency of passive control of the structure. Speed-based viscous dampers will adjust the amount of depreciation force based on the acceleration and velocity entering the system. On the other hand, displacement-based surge dampers adjust the amount of depreciation force based on the displacement required. Therefore, considering the different performances of these two dampers, the effect of using both of them in one structure can be investigated. In this study, by combining these two dampers, the seismic behavior of concrete structures has been evaluated. To study them, 5- and 10-story structures have been designed using FE method and have been subjected to earthquake records. Historical analysis shows that the use of hybrid dampers reduces the amount of seismic input force to the structure and also the amount of floor drift is reduced due to the use of dampers and also the capacity of structures for these structures is increased. The results of the study show that the presence of dampers in the structure increases energy absorption and improves performance in the structure.

1. Introduction

In conventional methods, the building demonstrates earthquake resistance by using a combination of hardness and ductility as well as energy dissipation. An efficient method used to improve seismic performance and damage control in structures is the use of energy consuming systems. In this method, mechanical energy dissipation tools are placed in the structure and deplete the energy. As a result, there is no need to use the high ductility of the structure and the nonlinear behavior of the main members to deplete the input energy. One of the most important mechanical tools is the energy consumption of viscous dampers. The location of these tools and the methods of their placement in the structure have a great impact on their efficiency and

effectiveness. Tsai et al. in 1998 [1], using analytical models, showed that the combination of speed-dependent and nonspeed-dependent devices in a structure is a powerful tool to increase seismic protection. They used a combination of a TPEA metal delivery device (triangular sheet energy absorbing device) as a hysterical element with a viscoelastic (VE) damper. Chen et al. in 2002 [2] used a six-span frame with four floors, and the results proved the strengths of different devices in counteracting each other's weaknesses.

Ibrahim et al. in 2009 [3] studied about the elastomeric damping material formed using VDP devices; the VPD increases the damping by increasing the displacement of the tire, and the energy absorption capacity increases as soon as the steel elements are delivered. The damper has a hyperelastic effect when it undergoes large displacement,

increasing the stiffness by stiffening the structure during severe seismic events to prevent the structure from collapsing. Murthy in 2000 [4], studied about VHD devices including concentric steel rims which are connected to the center of the structural opening using four braces. It is a multistage device similar to the VPD device, which has a large capacity for energy loss due to the delivery of steel and the geometry of the device. Recent research into composites or composite devices has included the addition of viscous dampers to a rugged lateral system with metal dampers. The goal is to add dampers and small displacements, as well as reduce nonstructural failure and acceleration. Brunea in 2015 [5], in an analytical study of a degree of freedom, found that viscous dampers reduce the effect of metal dampers. They also found that class accelerations were likely to increase for systems with small strain stiffness ratios. In 2014, Amadio et al. [6] analytically and experimentally investigated a hybrid system using PR joints and viscoelastic dampers. The advantage of a PR connection is that the damage is minimal, at least to a frame instrument with a connection hysteresis cycle. Viscoelastic dampers were used in conjunction with Chevron braces. The test results showed a significant reduction in displacement demand and instrument failure. This type of system is also able to meet the performance criteria based on the performance. The analysis proved that the best performance is obtained with the lowest cost, with an attenuation ratio of 11% or less.

So far, researchers have reviewed the hybrid passive control devices mentioned above. The idea of a combined HPCD passive control system was first proposed by Justin Marshall in 2013 [7]. The original HPCD demonstrated the phased behavior and energy dissipation of the system, which has the expected properties and behavior of the system, and the finite element models demonstrated its phased behavior and energy dissipation. Seismic structure and hazard provide an exceptional tool for performance-based seismic design. Investigation of the performance of structures under lateral loads, especially earthquake loads, is of great importance. Earthquake control, conduction, and energy dissipation can be a great help in the economic design of structures being designed and built. Therefore, in a study, the performance of structures in the state with and without two-level dampers has been investigated. In this research, three frames 5, 10, and 15 with and without dampers are examined. The results of this study show that the use of two-level dampers in 5-story structures increases the capacity of the structure by 4.7% and in 10- and 15-story structures, it improves the performance of the structure by 7.72% and 8.1%, respectively. In fact, the damper has been able to increase the capacity of the structure by absorbing lateral forces, and the structure, while enduring many stresses, also leaves acceptable displacement [8]. Few studies have been performed on passive control composite devices, and the combination of speed-dependent devices due to their ability to reduce

small vibrations with metal or friction devices (displacement-dependent) due to their high energy absorption capacity has considerable potential for future research [9].

In this study, four concrete structures in the form of two-dimensional frames are numerically modeled. In order to evaluate them under earthquake, the shear force and drift displacement of the floors have been used, which can indicate the seismic response of the structure. Regarding the structural cover diagram, it can be said that the structural cover diagram with damper is higher than the structural cover diagram without damper [10].

2. Material and Methods

In this research, four concrete structures in the form of two-dimensional frames in the number of 5 and 10 floors with a floor height of 3.2 meters and a distance of openings of 6 meters are considered. The structures are once equipped with a damper and once equipped with a viscous damper and a submersible damper. It should be noted that both dampers are used simultaneously in the concrete frame [9]. After modelling, the frames are analysed and designed. Also, the position of the dampers is in the second and fifth openings, which are specified in the following figures. The view of the modeled concrete frames is given in Figure 1.

Damper-exponential and multilinear plastic nonlinear elements have been used to model the dampers for modelling viscous and yield dampers, respectively [11]. The behavioral model of these elements is shown in Figure 2. The models are subject to earthquake records and dynamic analysis. The records used are shown in Table 1.

3. Numerical Simulation

In order to evaluate the samples under earthquake records, the basic shear and drift parameters of the floors have been used, which can indicate the seismic response of the structure. Figures 3–6 show the base section of 5- and 10-story structures with dampers and without dampers separately and the average base section of structures under 7 earthquake records. As can be seen, with the installation of dampers, the shear base has been significantly reduced in both height levels.

Figures 7–10 show the maximum drift of classes. To determine the drift of the floors, the drift history of each floor is specified and then the maximum drift obtained from them is selected as the maximum drift. It can be seen that despite the damper, the maximum drift of the floors has also decreased.

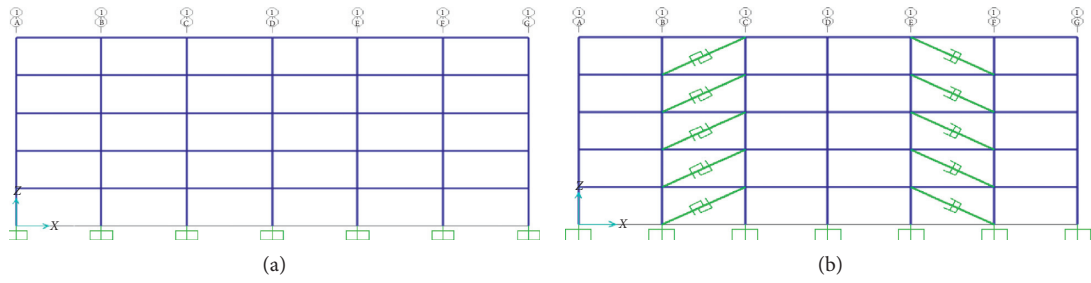
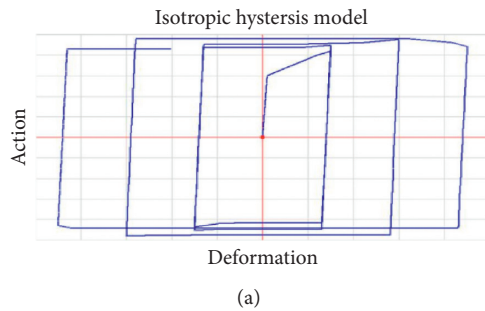


FIGURE 1: View of a 5-story concrete frame without and with dampers.

Hysteresis definition sketch



Hysteresis definition sketch

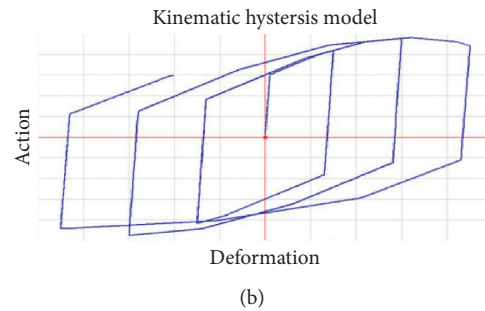


FIGURE 2: Models of nonlinear behavior of viscous and yield dampers.

TABLE 1: Characteristics of earthquakes.

Input time steps (s)	Maximum acceleration (g)	The magnitude of the earthquake	Distance from fault (km)	Date	Earthquake	Row
02/0	59/0	1/7	51/4	25/04/1992	Ala	1
02/0	59/0	7/6	71/4	17/01/1994	Bam	2
0.02	46/0	4/7	19	21/06/1990	Manjil	3
0.02	395/0	7/6	11.4	17/01/1994	Northridge	4
005/0	339/0	5/6	3/9	6/08/1979	Imperial	5
0.005	0.53	4/7	6/5	17/08/1999	Tur	6
005/0	452/0	3/7	8/8	15/06/1994	Kobe	7

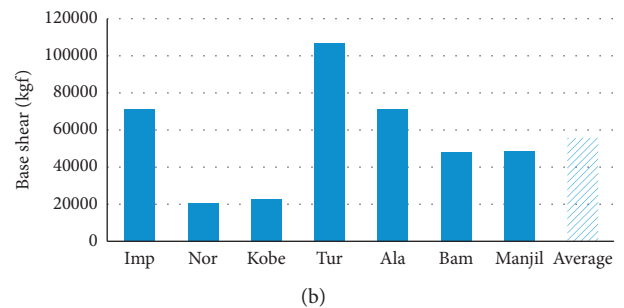
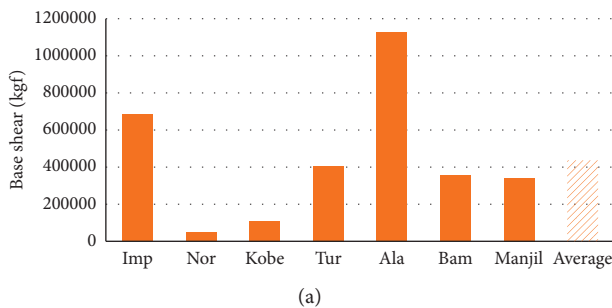


FIGURE 3: Maximum shear base diagram of a 5-story structure without and with damping. (a) Base shear without damper. (b) Base shear with damper.

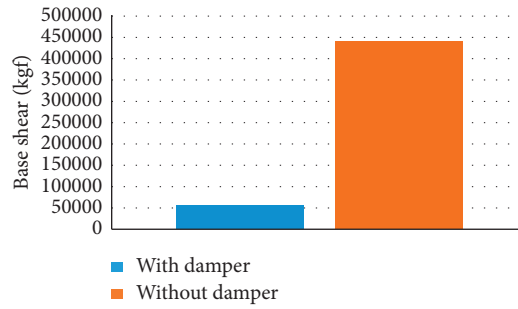


FIGURE 4: Diagram of the average shear base of the maximum of 5-story structures.

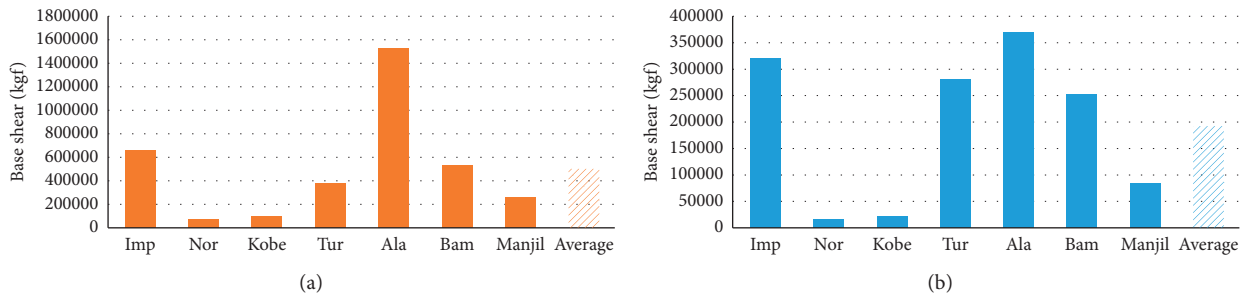


FIGURE 5: Maximum shear base diagram of a 10-story structure without and with damping. (a) Base shear without damper. (b) Base shear with damper.

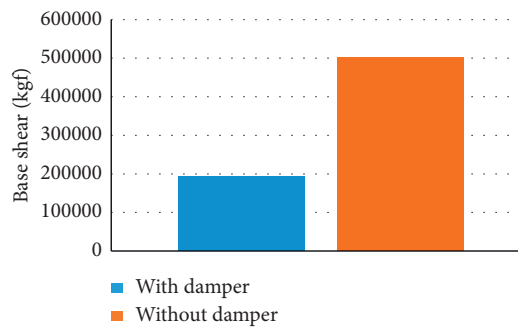


FIGURE 6: Diagram of the average shear base of the maximum of 10-story structures.

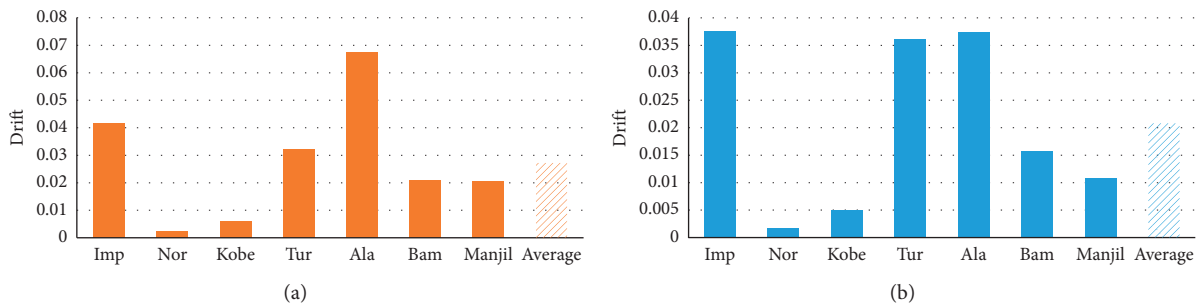


FIGURE 7: Maximum drift diagram of a 5-story structure without and with damping. (a) Drift without damper. (b) Drift with damper.

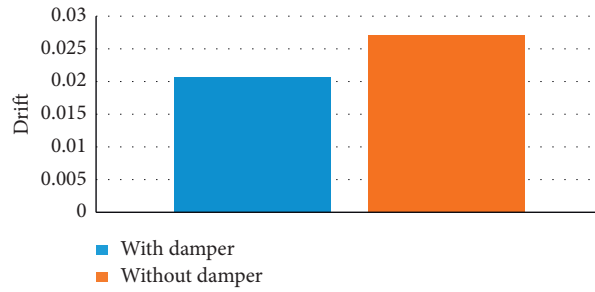


FIGURE 8: Average drift diagram of 5-story structures.

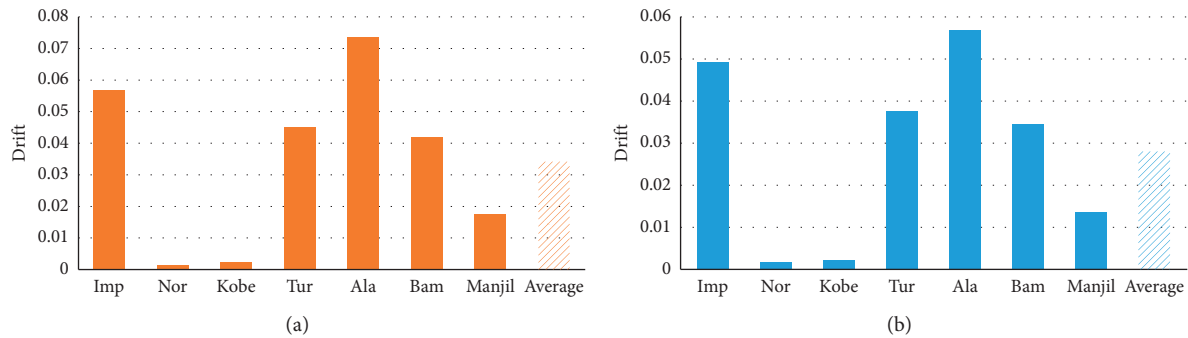


FIGURE 9: Diagram of the maximum drift of a 10-story structure without and with damping. (a) Drift without damper. (b) Drift with damper.

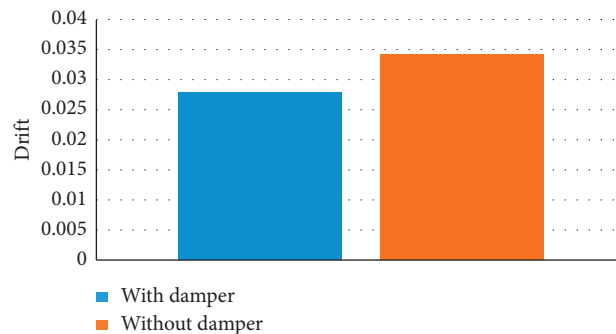


FIGURE 10: Graph of maximum drift average of 10-story structures.

4. Conclusion

Regarding the amount of shear base, it can be concluded that the amount of shear base of 5- and 10-story structures under the influence of dampers has decreased significantly compared to structures without dampers. According to the average values of the shear base, it can be concluded that the amount of shear base in the structure with dampers in the 5-story structure is about 86% and in the 10-story structure is about 62% compared to the structure without dampers. The maximum drift rate of 5- and 10-story structures under the influence of dampers has decreased significantly compared to structures without dampers. According to the average values of drift, it can be concluded that the maximum drift rate in the 5-story structure with dampers is about 62% and in the 10-story structure is about 17% compared to the

structure without dampers. Regarding the structural cover diagram, it can be said that the structural cover diagram with damper is higher than the structural cover diagram without damper. The presence of dampers in the structure has increased the amount of energy absorption in the 5-story structure by about 64% and in the 10-story structure by about 60%, which has increased the data. Therefore, it can be concluded that the presence of dampers in the structure increases energy absorption and improves performance in the structure.

Data Availability

Requests for access to these data should be made to the corresponding author via e-mail address: nima.marzban@tabari.ac.ir.

Conflicts of Interest

The authors declare that there are no conflicts of interest regarding the publication of this paper.

References

- [1] J. Tsai, L. Li, J. Dai, and J. Ou, "A single-degree-of-freedom system using a time-delayed control algorithm: principle and experimental study," *Journal of Vibration and Control*, vol. 17, pp. 1840–1850, 1998.
- [2] W. Zhe, C. Liang, U. Filippo, and L. Simon, "Numerical investigation and design of reinforced concrete shear wall equipped with tuned liquid multiple columns dampers," *Shock and Vibration*, vol. 2021, Article ID 6610811, 19 pages, 2021.
- [3] L. Chen, G. Song, and J. Ou, "A genetic algorithm-based two-phase design for optimal placement of semi-active dampers for nonlinear benchmark structure," *Journal of Vibration and Control*, vol. 16, pp. 1379–1392, 2002.
- [4] P. J. Ibrahim, S. A. Neild, and D. J. Wagg, "Semi-active damping using a hybrid control approach," *Journal of Intelligent Material Systems and Structures*, vol. 23, pp. 2103–2116, 2009.
- [5] M. J. L. Murthy, J. V. Calvo, B. L. Boada, and V. Díaz, "Modeling of a magneto rheological damper by recursive lazy learning," *International Journal of Non-linear Mechanics*, vol. 46, pp. 479–485, 2000.
- [6] C. Xuansheng, J. Chuansheng, and Z. Yue, "Seismic responses of an added-story frame structure with viscous dampers," *Mathematical Problems in Engineering*, vol. 20149 pages, Article ID 468672, 2014.
- [7] C. Ho and C. K. Ma, "Active vibration control of structural systems by a combination of the linear quadratic Gaussian and input estimation approaches," *Journal of Sound and Vibration*, vol. 301, pp. 429–449, 2015.
- [8] S. Hong, M. T. Nguyen, N. M. Kwork, Q. P. Ha, and J. Li, "Hysteresis model for magneto rheological fluid dampers using a curve fitting approach," *Journal of the Japan Society of Applied Electromagnetics and Mechanics*, vol. 15, pp. 176–179, 2004.
- [9] D. Marshall, S. Justin, and T. Engin, "Modeling and testing of a field-controllable magneto rheological fluid damper," *International Journal of Mechanical Sciences*, vol. 52, pp. 1036–1046, 2013.
- [10] W. Manisha, M. Suhasini, and M. Vasant, "Influence of nonlinear fluid viscous dampers on seismic response of RC elevated storage tanks," *Civil engineering journal*, vol. 1, pp. 12–25, 2020.
- [11] W. Xiaoli, G. Wei, H. Ping, B. Dan, X. Xu, and H. Yao, "Seismic performance evaluation of building-damper system under near-fault earthquake," *Shock and Vibration*, vol. 2020, Article ID 2763709, 21 pages, 2020.

Research Article

Performance Evaluation of CFRP Strengthened Corrosion-Proof Columns

Mohammadamin Mirdarsoltany , **Alireza Rahai** , and **Mohammad Zaman Kabir**

Department of Civil Engineering, Faculty of Civil Engineering, Amirkabir University of Technology, Tehran, Iran

Correspondence should be addressed to Mohammadamin Mirdarsoltany; amin.st@aut.ac.ir

Received 28 April 2021; Revised 25 May 2021; Accepted 23 June 2021; Published 10 July 2021

Academic Editor: S. Mahdi S. Kolbadi

Copyright © 2021 Mohammadamin Mirdarsoltany et al. This is an open access article distributed under the Creative Commons Attribution License, which permits unrestricted use, distribution, and reproduction in any medium, provided the original work is properly cited.

The application of FRP composites in recent years has attracted much attention. Lightweight, high strength, and corrosion resistance are among the properties that make this material available in various forms in construction engineering. The present study analyzed the performance of carbon fiber-reinforced accelerated corrosion-proof box. Nine columns without corrosion and cross-corrosion reinforcement were tested in laboratory and software. Syntax reinforcement was applied locally to the damaged area with respect to a transverse and longitudinal layer. The results of the axial test showed that, due to corrosion, the damaged site was weakened by the loading and severe resistance decreased, and the range of damage points due to the axial load was highly deformed compared to the initial state. The damage caused on both sides of the steel column had a significant effect on reducing the hardness and deformation of the steel columns; it is worth noting that the corrosion on both sides of the steel column had the most variations among the samples. Application of CFRP with 2 layers in the damaged steel columns resulted in increased bearing capacity and hardness in the affected area due to corrosion so that reinforcement of these columns by carbon fibers improved the axial strength.

1. Introduction

Today, due to the expansion and importance of oil and maritime transport activities and attention to mining in the seabed, construction activities such as the construction of piers, platforms, and similar structures in coastal and oceanic areas have increased significantly. Although concrete is considered a durable material in the sea environment, many breakdowns of concrete structures along the coast have been reported. When designing concrete and metal structures that are located in the vicinity of seawater, it is necessary to consider the effect of destructive environmental factors to which concrete is exposed during the long years of operation and it seems that the designs based on the criterion of strength for such structures are not enough. In addition to the strength criterion, the durability of concrete in these areas should also be considered.

FRP composites are relatively new materials that are not widely used [1]. Today, high-rise buildings are constructed

with steel and concrete structures, and each of the concrete and steel structural systems has its advantages and disadvantages, which cannot be expressed in this article, and employers, according to their needs, one of the two. They choose the type of structural system. However, what is less considered when choosing the structural system of buildings is their ability to resist accelerated corrosion. In this study, the focus is on accelerated corrosion in incomplete steel structures. In general, steel structures, with advantages of high strength and good ductility, also have disadvantages that have limited their use in some structures. Steel can be considered vulnerable in two ways, including its vulnerability to heat and corrosive environmental factors. Accelerated corrosion is one of the deadliest hazards that structures may face during their lifetime [2].

In recent years, attention has been paid to the reinforcement of damaged structures, seismic improvement, and increasing the flexural capacity of steel members. Moreover, to improve and modify traditional methods, new

reinforcement methods have been replaced in order to facilitate reinforcement and increase the capacity of structures, making structural engineers use polymer systems reinforced with polymer reinforcing fibers. Most research has been done on reinforcing steel structures with FRP. Reinforcement of steel members with less axial load has been studied. Therefore, in this research, the compressive load capacity of a short steel column reinforced with FRP has been investigated. The use of FRP can be used not only to restore the lost strength of the steel section due to corrosion but also to increase the bearing capacity of healthy sections, increase the fatigue life, and prevent the growth of cracks, provided that conditions such as adhesion resistance are met [3].

Contrary to popular belief, the parameters of load and strength in the design of structural members are not definite quantities and are random variables, so it is impossible to design completely safe structures and using a probabilistic approach to calculate the performance of structural members in design is inevitable. In building corrosion safety regulations, there is always a classification in terms of building use, and the level of requirements in each group of buildings varies depending on their importance. Once the level of corrosion safety expectations for a building is determined, the designer must use materials with good properties and behavior against accelerated corrosion. Therefore, it is necessary for building designers and engineers to provide a classification (or classifications) of the behavior and characteristics of materials and materials against corrosion [4].

2. Literature Review

Kitada et al. investigated the behavior of a circular steel column filled with ordinary concrete and recycled concrete reinforced with CFRP. Carbon fiber-reinforced circular columns were studied in the laboratory. The use of CFRP increases the ductility and bearing capacity, and increasing the number of layers increases the bearing capacity, and to increase the strength of steel columns, FRP and concrete jacket methods can be used. This study showed that the use of CFRP materials for reinforcement increases the compressive capacity and loading and the use of these materials in a semitorsional manner has less axial compressive strain than a complete torsion [5].

Harries et al. worked on reinforcing steel columns filled with concrete by CFRP; they tested a number of sections of steel filled with mortar and reinforced with FRP. For 22 samples, they examined the performance such as reinforcement method, concrete type, and cross-sectional shape and concluded that CFRP screw circumference on solid and hollow circular columns has a better effect than square-shaped sections after reinforcement of middle failure [6]. This article presents a reinforcement method to improve the vibration resistance of steel in compression, while a FRP tube filled with mortar is rolled out of the steel member and wrapped in FRP fabric at the end of the tube. Through axial compression tests in 18 specimens with two-way symmetrical cross-section, load-strain expansion and failure modes were obtained and the bearing capacity and flexibility were

increased. The cross-sectional effects of the steel layers reinforced with the FRP layer wrapped at the end of the samples were investigated. It was found that after reinforcement, the failure modes of midheight steel produced from the steel member changed to local damage at the end of the steel due to global bending. As a result, load-bearing capacity increased by 44 to 215 percent. A segmentation model was developed for the reinforced specimens, with a calculated load-bearing capacity consistent with the test results [7].

Bambak et al. examined the periodic performance of circles and squares, so-called double-walled hollow columns, and placed the columns under a fixed load and a reverse bending load. Column failure was characterized by longitudinal carbon fiber rupture following peripheral fiber rupture. The test results showed that increasing the axial load level of the columns increases the flexural ductility, while increasing the carbon fiber layers in the outer tube increases the strength but decreases the flexural ductility of the column. The mechanical model in this article is completed for HSS split columns. The integrated theory is as follows: this introduces a confidential factor to describe the performance of a composite steel pipe and aerated concrete. The predicted load to deformation ratio was in good agreement with the test results. The theoretical model is used to investigate the effect of important parameters that determine the final strength of composite columns. Parametric and experimental studies provide information for the development of formulas for calculating the ultimate strength and axial load relative to the axial pressure curves of composite columns [8].

Jama and Bambak conducted a laboratory study of stress-strain behavior, final bearing capacity, and fracture modes of steel section filled with concrete and reinforced with CFRP fibers transversely. They wrapped the carbon fibers in strips around the column, taking into account factors such as the thickness and distance of the strips. As the distance between the CFRP strips increases, buckling occurs in the fiber-free part, and the greater the number of layers, the better the control of axial deformation. Proper spacing between CFRP strips is essential to delay buckling and increase ultimate bearing capacity and axial strain stress behavior. CFST concrete pipe members are very popular in the construction industry, and at the same time, structural aging and member failure are often reported. Measures such as the implementation of new materials and reinforcement techniques are necessary to deal with this problem. This research aims to investigate the structural progress of CFST sections with ordinary external concrete bonded with fiber-reinforced polymer (FRP) composites. For this study, mildly pressed mild steel pipes with the main variable having FRP properties are used. Carbon fiber-reinforced polymer fabrics (CFRP) are used as horizontal strips (lateral relations) with several other parameters such as the number of layers and width and spacing of strips. Among the 30 specimens, twenty-seven were grafted outside the 50 mm wide strip of CFRP tapes at intervals of 20, 30, and 40 mm, and the remaining three specimens were unbounded. Experiments were performed before column failure to fully understand

the impact of FRP parameters on the compressive behavior of square CFST sections, including their failure mode, axial stress pressure behavior, and load-carrying capacity. From the test results, it was found that the external connection of CFRP strips effectively causes external thrust pressure, accelerates the local delay of the steel pipe, and also increases the load-carrying capacity. Finally, an analytical model is proposed to predict the axial load capacity of reinforced CFST sections under compression [9].

Haedir et al. analyzed the behavior of a concrete steel bridge reinforced with CFRP sheets; the connection was made to the bottom and the beams. The test results showed that the strength and stiffness of the steel-concrete composite bridge increased up to 45% compared to the main strength of the beam. The use of advanced composite materials to rehabilitate declining infrastructure is accepted worldwide. Conventional techniques for reinforcing unsuitable bridges are costly, time-consuming, and labor-intensive. Many new techniques use lightweight, high strength, and corrosion resistance polymers reinforced with FRP laminate for repairs and application completion. The load-carrying capacity of a composite steel box is significantly wrapped with carbon fiber-reinforced polymers laminate to its tension flange. In this article, the results of a study on the behavior of reinforced concrete steel composite columns with CFRP sheets under static loading are presented. A total of three large composite columns made of steel sheet with a thickness of 75 mm have been prepared and tested with 910 mm concrete. Constant CFRP leaf thickness and a number of other layers 1, 3, and 5 were used in the samples. The test results showed that the CFRP epoxy bond sheet increased the final bearing capacity of steel composite channels and the behavior can be predicted by traditional methods [10].

By examining the failure of thin-walled steel columns at the pier, Kalavakunta et al. determined that most of the failures were of the local buckling type, which reduced the load-bearing capacity and increased the deformation. This article describes (1) some computer programs for the analysis of fixed plastic/dynamic elastoplastic displacement used in the design of steel bridges; (2) final strength and design methods for steel sheets, sheets, and columns made of compression-resistant steel; (3) seismic design and completion methods for new and existing postearthquake Hyogo-Ken Nambu bridges; (4) friction-type joints and tension-type joints with strong bolts and nuts and development of high-performance fins in Japan. These are the topics that the authors discuss: the new technologies of steel bridges under development in Japan are as follows: the development of high-performance steel, new fiber materials, new types of bridges, performance-based design methods, seismic design methods against Level 2 earthquakes like the Hyogo-Ken Nambu earthquake, and the bridge management system [11].

Hadianfard et al. showed that the use of CFRP to reinforce short canned steel sections under axial impact showed that the use of these materials increases energy absorption and strength. Moreover, studies on steel sections showed failure energy and cross-section strength. Steel-short

boxes depend on the type of steel and the ratio of CFRP thickness to CFRP width. The use of CFRP increases the ultimate bearing capacity and specific energy; the reinforcement of CFRP structures has increased, traditionally in use with concrete structures, and more recently in applications with steel structures. This article presents experiments and analyzes of the mechanism of plastic square hollow square reinforced steel using CFRP external bonding reinforcement by deformation in axis-symmetric collapse mode under large static-like axial compression. The process of forming the empty column delay was such that the flat sides formed the known structure of the roof. The collapse was done gradually by folding around the hinged lines and producing four corners. The expression for the plastic axial load of a falling plastic is obtained by equating the total energy absorbed in the bending and the external work done during the deformation of the composite pipe. It has been shown that the loaded values and loads of the predicted loads are instantaneously well compared with the test results [12].

Liu et al. evaluated the effect of transverse and longitudinal reinforcement with CFRP in ten short columns in the laboratory. This article presents the design and experimental design of CFRP external carbon fiber-reinforced polymer sheets for the reinforcement of short circular tubular columns. In addition to ease of handling due to being lightweight, a high-strength CFRP sheet box is somehow limited for thin steel wall retardation. Ten circular hollow columns composed of cold steel with external CFRP columns (adjacent outer and longitudinal rectangles) were tested under compressive pressure. Laboratory results show that fiber-reinforced steel pipe reinforcement increases the capacity of the axial section. The design variables considered to evaluate the reinforcement efficiency are the strength of the steel performance, the modulus of elasticity of the carbon fiber, and the amount and configuration of the fiber reinforcement. The results indicate the ease of using such a curve in FRP reinforcement or redesign of tubular columns to increase section capacity [13].

Teng et al. studied the CFRP-reinforced edged canal column under axial load. They studied the channel-shaped column in two ways: gluing the fibers to the whole column and gluing to the core in the laboratory and found that the bearing capacity increased up to 16.75% in the reinforced channel section and up to 10.26% in the reinforced sample. Due to the layering and separation of CFRP, our capacity reduction and sudden failure were considered and the use of CFRP increased the bearing capacity. It was concluded that surface and temperature preparation are two important factors to achieve proper adhesion between steel and fibers; carbon fiber-reinforced polymer composites (CFRP) are of high performance and potential for use in reinforcement, completion, and reconstruction of parts. In this article, design methods for the axial load capacity of cold steel reinforced steel column reinforced polymer with carbon fiber-reinforced polyester (CFRP) are proposed. For validation purposes, the results are based on a proposed design criterion of North American specifications for the design of steel and euro-shaped steel structures for cold members, and the sheet is compared with experimental test data. The test

results showed that the capacity of the columns is close to the theoretical values predicted by the regulations. Some of the samples tested had reduced capacity and premature failure due to peeling and depletion of CFRP from steel. Various experimental studies have been proposed to carry out future work to validate and update the design equations. From experimental studies, it has been seen that there is a significant increase in strength due to the enhancement of CFRP [14, 15]. Tanabandeh and Gardoni used probabilistic capacity models for estimating the fragility of structural components [16].

3. Materials and Methods

In order to investigate corrosion or structural defects on the capacity of steel columns, a number of laboratory samples are first made and placed under axial load. The results of these experiments, including the displacement curve of the column tip and the axial force created in the column, will be quantitatively evaluated along with the shape and mode of failure of the members. The results of this study, including the material and its mechanical properties, support conditions, and loading methods, will be used to simulate the finite elements of the samples and calibrate the parameters used. After extracting the simulation results and validating them with the values obtained from the laboratory, the calibrated parameters are used to make more samples with more diverse variables. Due to the application of the finite element method along with laboratory studies in the analysis of models used in research, the obtained information will be presented and studied in the form of graphs and tables. In this research, the first samples of incomplete steel columns (9 samples) are designed and after construction, according to the research requirements in the laboratory, they are subjected to accelerated corrosion. Then, according to the results obtained from experimental samples, computer models are simulated and calibrated and the same number of samples will be prepared and studied for parametric study. Therefore, the method used in this research will be the laboratory method along with computer analysis methods (finite element method).

4. Finite Element Model

Before any research, to ensure the validity of the software used, we must model an example of past research by the software. For this purpose, the results of a laboratory sample, conducted by Bombach et al. [17] according to Figure 1, have been studied and modeled. In this experiment, a box-shaped member with dimensions of $2 \times 100 \times 100$ mm, a height of 300 mm with a modulus of elasticity of 200 GPa, a Poisson coefficient of 0.3, CFRP fibers with a modulus of elasticity of 230 GPa, and final strength of 3790 MPa has been used. According to Figures 2(a) and 2(b), the degree of adaptation of the force-displacement curve in the sample is modeled and compared with the laboratory sample being very accurate, which indicates the correct choice of grid size, application of optimal boundary conditions, and appropriate analysis and modeling. It was a software example. As it is

known, for simple and reinforced columns, mesh size with a score of 10.5 is the best case in validation [18]. Moreover, with this mesh score, we were faced with the best answer and the lowest percentage difference compared to the laboratory sample. Table 1 compares the results of steel box member analysis with the number of different FRP layers, the critical load, and the percentage difference of the final load in the sample. In Figures 2(a) and 2(b), *F0* means no reinforcement, *F1* means coating with one layer of CFRP, and *F2* means coating with two layers of CFRP. NU means modeled sample and EX means laboratory sample. All modeled elements were considered solid and modeled using FEM according to Figure 3.

5. Mechanical Properties

In this study, the reinforced specimens were reinforced in two layers (longitudinal and transverse) with a twist at the injury site and a 20 mm overlap (Table 2).

The steel used in this research has a final strength of 336 MPa and a final strain of 12%, which is modeled nonlinearly in the software, with an elasticity of 200 GB and a Poisson's ratio of 0.3. In this research, in order to strengthen and improve the performance of the defective box steel column, carbon fibers have been used to achieve the initial performance of the compression member. The method of using carbon fibers was twisted in the defect area. The adhesive used in this study was used to enhance the performance of box columns with CFRP carbon fibers (Tables 3 and 4).

Compression-loaded box steel columns have nine specimens, including one intact specimen, four specimens with (horizontal) defects, and four specimens reinforced with CFRP carbon layers. To name the steel column columns with horizontal defects, a horizontal defect in the center has been applied as follows. The horizontal parameters were H, the lateral S, the middle M, and the defect D.

Dimensions of the defect: the length and width of the defect are equal to 40×40 mm, respectively [20, 21]. Moreover, the number 2 indicates the number of defects; it should be noted that the length of the defect on both sides decreases to 20 mm on both sides (Table 5). The first word M indicates a defect in the middle of the surface of the steel column (Middle). Second word S indicates a defect with a side position (Side); third word H indicates that the defect is horizontal (Horizontal). The fourth word D indicates the word defect (Defect).

FEM provides extensive capabilities for simulation in linear and nonlinear applications. Problems with multiple components and different materials can be simulated by defining the geometry of each component, assigning its constituent materials, and then defining the interaction between these components [22, 23]. The present study shows the high capability of FEM that the simulation of the samples provided the ability to examine structures with a suitable graphical environment. The selection of the appropriate element and mesh size and the specifications of the studied materials were expressed in this chapter. Examination of the results of the modeled samples showed defects in the steel

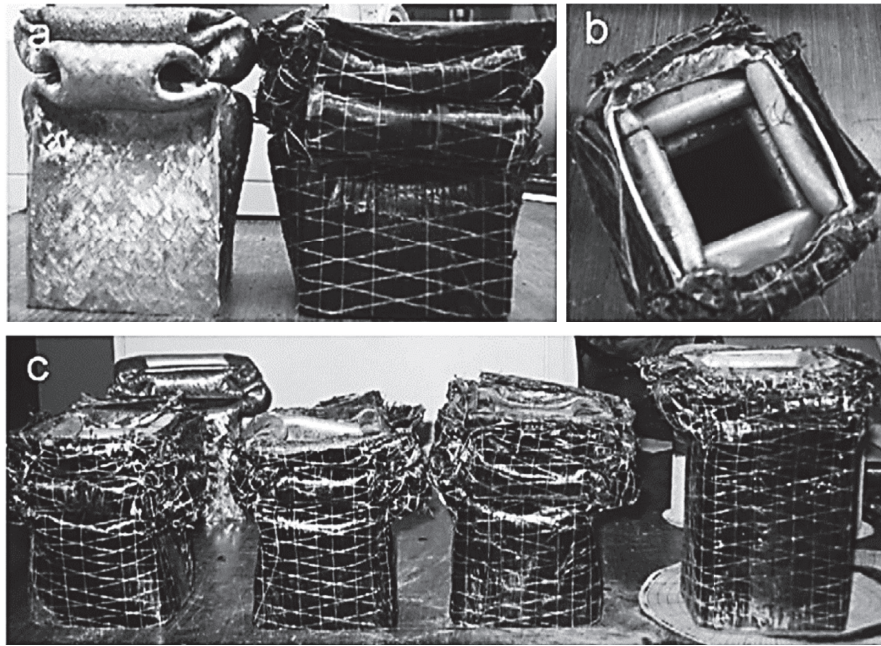


FIGURE 1: Laboratory sample of Bombach et al. [17].

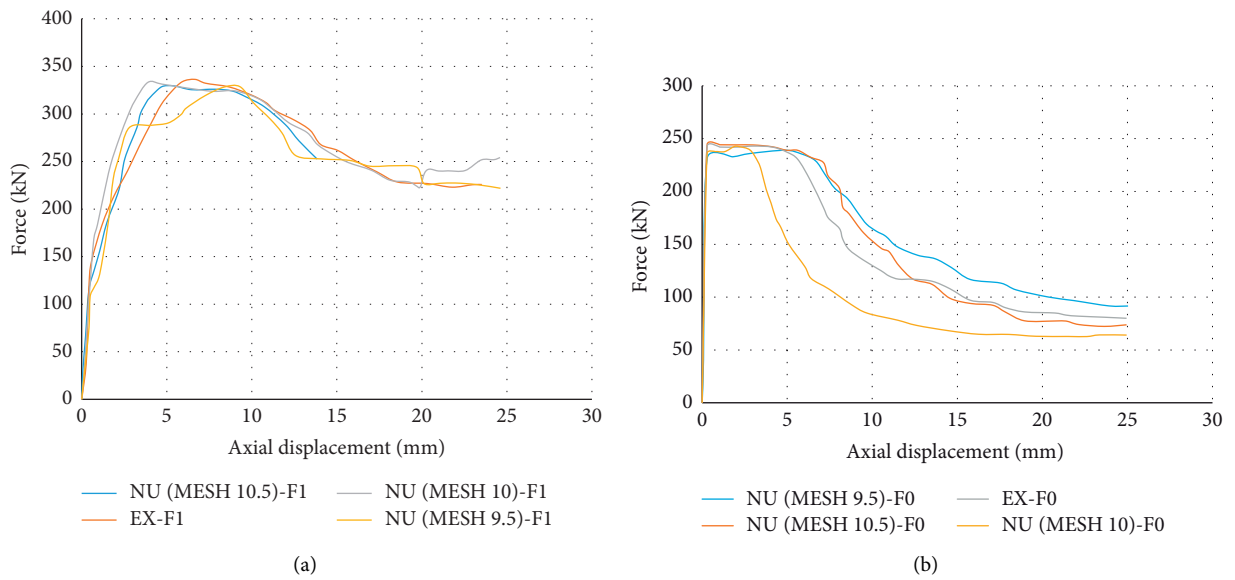


FIGURE 2: Validation results of modeling. (a) Retrofitting sample. (b) Nonretrofitting sample [17].

TABLE 1: Comparison of results obtained from laboratory samples and numerical modeling.

Number	Cross-section dimensions (mm)	Height (mm)	Layers of CFRP	Critical load from the laboratory (kN)	Critical load from numerical modeling (kN)	Percentage error
1	2 * 100 * 100	300	0	238.2	239.59	0.5
2	2 * 100 * 100	300	1	338	337.1	0.27
3	2 * 100 * 100	300	2	425	427.31	0.55

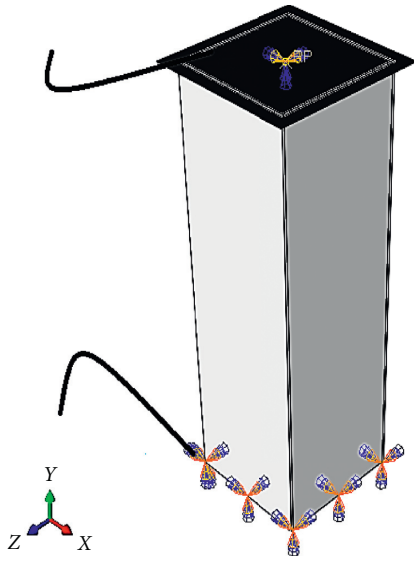


FIGURE 3: Sample validation modeling of Bombach et al. [17].

columns under axial load, reduced loads, stiffness, and increased deformation in the area of damage. Defects in steel columns will increase the rate of deformation and drop in strength. High-strength CFRP fibers increased the stiffness of the injured limbs, and the placement of the CFRP fibers transversely and longitudinally helped repair the damaged element.

6. Examination of Laboratory Samples

6.1. Laboratory Results. In this section, the results of experiments performed on 9 samples are reviewed. Figure 4 shows the force-displacement diagram of the laboratory samples. It can be seen that the control sample has surrendered due to the force of 158 kN and its maximum displacement at the yield point was 8.8 mm [24].

6.2. Comparison of Modeling and Laboratory Results. Figure 3 shows the force-displacement diagram of laboratory and modeled specimens. It can be seen that in Figure 5, in terms of sample MHD2-40*40, the two diagrams are in good agreement with each other. It is also clear from the laboratory diagram that the maximum bearing capacity occurred up to 112 kN. We were in the plastic range and the maximum displacement continued up to 4.9 mm [25].

Figure 6 shows that in the SHD2-40*40 sample, the two diagrams fit well together. It is also clear from the laboratory diagram that the maximum bearing capacity occurred up to 95 kN. Then, we saw the displacement behavior in the plastic range and the maximum displacement continued up to 7.5 mm [26].

It can be seen that in Figure 4 and in the SHD40*40 sample, up to a force of 128 kN, the two diagrams are in good agreement with each other. Then, we saw the displacement behavior in the plastic range and the maximum displacement continued up to 6.5 mm.

It can be seen that in Figure 7 and in the sample MSHD2-40*40, the two diagrams were in good agreement

with each other. It is also clear from the laboratory diagram that the maximum load capacity occurred up to 107 kN. The displacement behavior was in the plastic range and the maximum displacement continued up to 6.9 mm. In Figure 8 and in the sample MHD2-40-1T1L, the two diagrams are in good agreement with each other [28, 29].

It can be seen that, in Figure 9 and in the sample SHD2-4*40-1T1L, the two diagrams are in good agreement with each other. It is also clear from the laboratory diagram that the maximum load capacity occurred up to 129 kN. We saw the displacement behavior in the plastic range and the maximum displacement continued up to 6.8 mm. It can be seen that in Figure 10 and in the SHD40*40-1T1L sample, the two diagrams fit well with each other. The maximum carrying capacity occurred up to 140 kN. On the other hand, this sample witnessed the displacement behavior in the plastic range, and the maximum displacement continued up to 8.2 mm [30].

In Figure 11, it can be seen that in the sample MSHD2-40*40-1T1L, the two diagrams are in good agreement with each other. It is also clear from the laboratory diagram that the maximum load capacity occurred up to the limit of 125 kN. The displacement behavior was in the plastic range and the maximum displacement continued up to 11.1 mm.

It can be seen that in Figure 12 and in the control sample, the two diagrams are in good agreement with each other. It is also clear from the laboratory diagram that the maximum load capacity occurred up to 158 kN. This was in the plastic range and the maximum displacement continued up to 8.8 mm (Table 6).

6.3. Investigation of Rupture Modes. To study the fracture modes of canned steel columns, we first examine the column with horizontal defects. As can be seen from Figure 13, specimens with a horizontal defect created in the steel column wall experienced local buckling during loading. The location of the defects caused by loading underwent axial deformation of the local buckling type, and the damaged areas reduced the axial strength in the samples [32].

As it is clear from the injury sites, the concentration of stress and the reduction of stiffness occurred in the defective areas. The position of the carbon fiber reinforcement proved that these fibers increased the hardness and ductility by completely covering the steel column. According to the samples reinforced with two layers of carbon fibers, it was determined that these fibers, by completely surrounding the damaged area, delayed the rupture around the defect.

Figures 13 and 14 show the final deformations of short steel columns with defects in two walls. Axial failure on these members was investigated until complete failure because the axial load of the column without carbon layer on the side sides suffered local buckling and complete failure. CFRP composites, as suitable materials for strengthening steel columns, played an effective role in improving the compression member so that

TABLE 2: Dimensions and characteristics of box steel column [17].

Specifications of box steel column				Modulus of elasticity (GPa)	Tensions (MPa)		Strain (%) Final strain
Length * width (mm)	Thickness (mm)	Height (mm)	Cross-section (mm)		Cross tension F_y	Final tension	
70 * 70	2	300	2.7	200	250	336	12

TABLE 3: CFRP carbon fiber [17].

Thickness (mm)	Density (g/cm ³)	Tensile strength (MPa)	Modulus of elasticity (MPa)	Final strain
0.17	1.76	3790	230000	1.2

TABLE 4: Properties of epoxy resin [17].

Tensile strength (MPa)	Modulus of elasticity (MPa)	Final strain (%)
75	3	3-4.5

TABLE 5: Bearing capacity of the models modeled in ABAQUS program.

Carrying capacity (kN)	Sample name	Number
139	Control	1
98	MHD2-40 × 40	2
84	SHD2-40 × 40	3
115	SHD-40 × 40	4
98	MSHD2-40 × 40	5
112	MHD2-40 × 40-1T1L	6
115	SHD2-40 × 40-1T1L	7
127	SHD-40 × 40-1T1L	8
119	MSHD2-40 × 40-1T1L	9

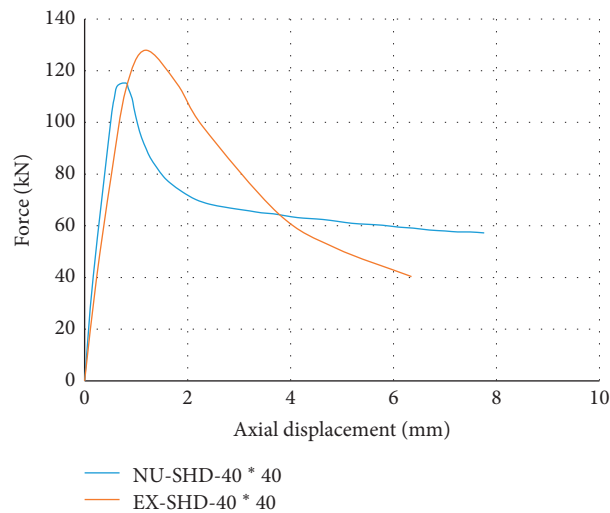


FIGURE 4: Force-displacement diagram of model and laboratory sample [27].

these fibers, by covering the entire length of the column with two transverse and longitudinal layers, increase the stiffness and strength of the samples. Moreover, the effect of using these fibers has been very effective in controlling buckling. Figures 15 and 16 show the effect of using CFRP fibers.

As investigated, the effect of carbon layers on box steel columns is very good and strengthening these members with two layers of CFRP will help to control axial rupture and increase ductility and energy absorption. Examination of the deformations obtained from the laboratory and its adaptation to

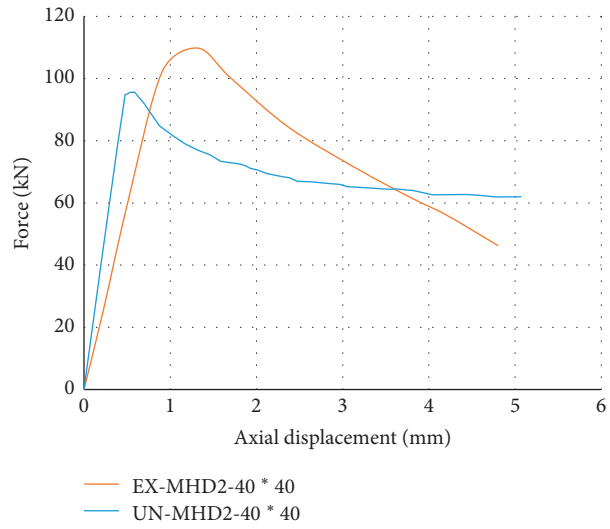


FIGURE 5: Force-displacement diagram of model and laboratory sample.

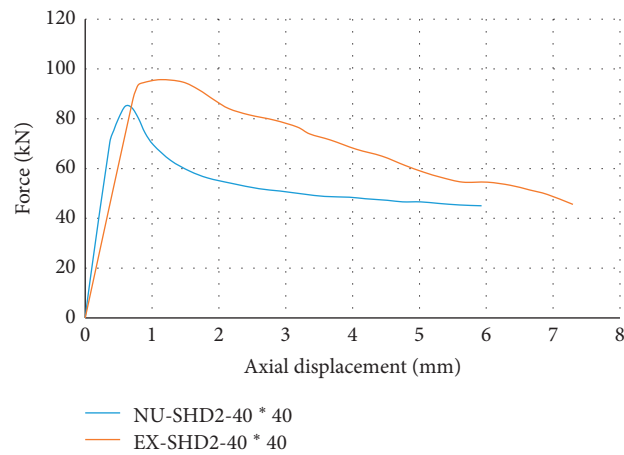


FIGURE 6: Force-displacement diagram of model and laboratory sample.

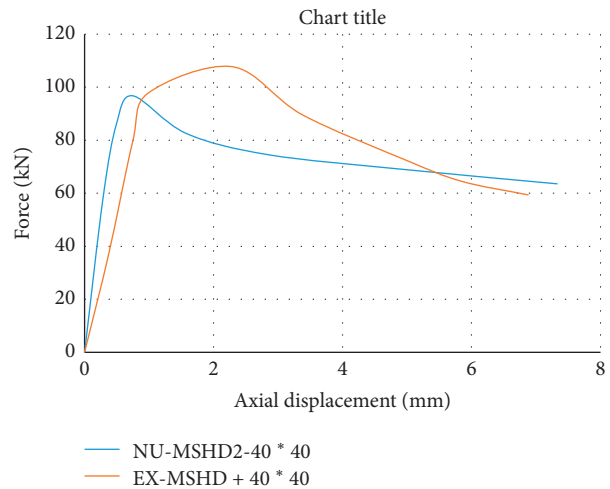


FIGURE 7: Force-displacement diagram of model and laboratory sample [27].

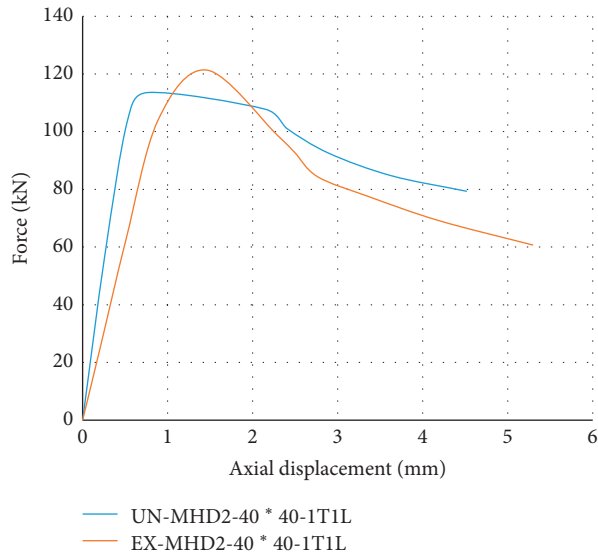


FIGURE 8: Force-displacement diagram of model and laboratory sample.

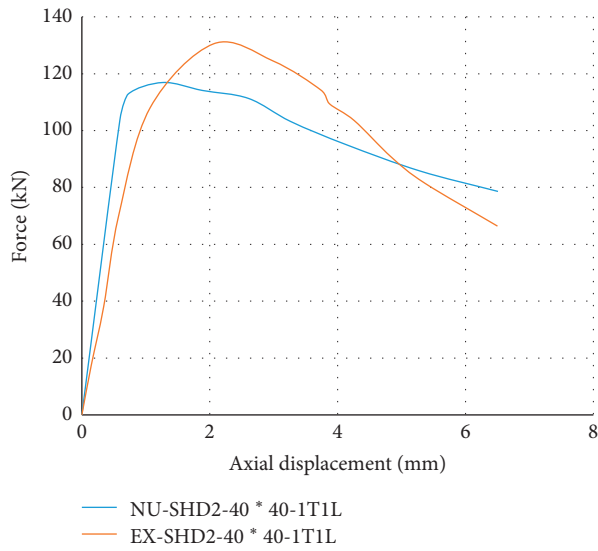


FIGURE 9: Force-displacement diagram of a modeled and laboratory sample.

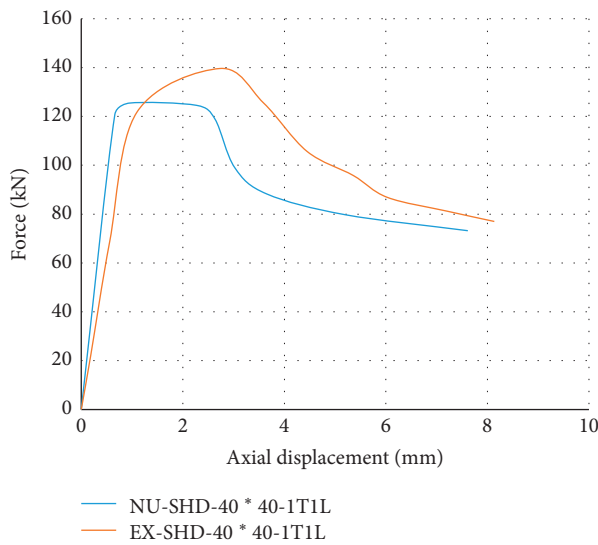


FIGURE 10: Force-displacement diagram of model and laboratory sample.

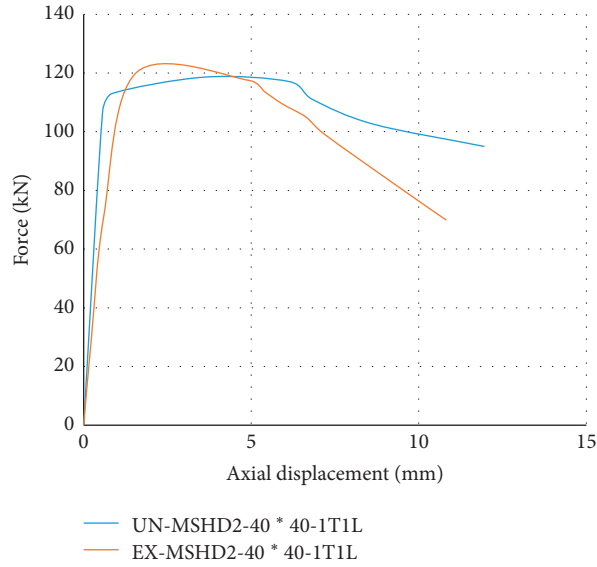


FIGURE 11: Force-displacement diagram of model and laboratory sample.

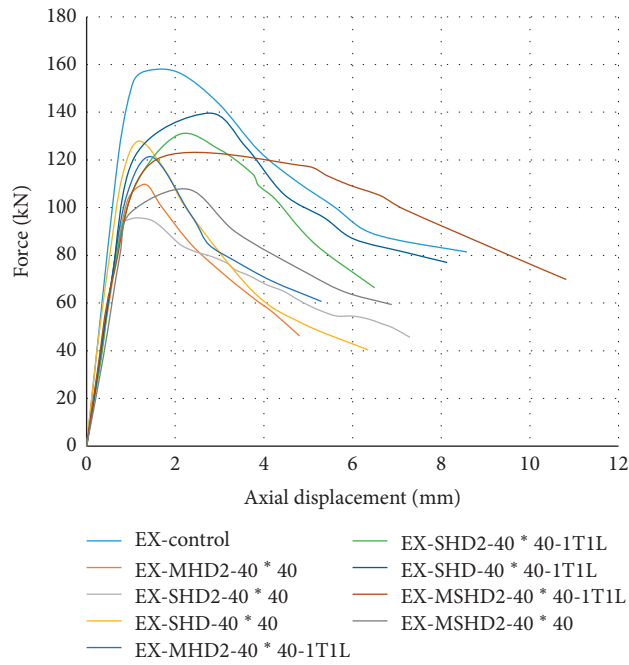


FIGURE 12: Comparison of force-displacement diagram of laboratory samples.

TABLE 6: Specifications of laboratory samples and modeling [31].

Percentage difference	Laboratory bearing capacity (kN)	Carrying capacity modeling (kN)	Sample name	Number
12.03	158	139	Control	1
12.5	112	98	MHD2-40 × 40	2
13.02	84	95	SHD2-40 × 40	3
10.21	128	115	SHD-40 × 40	4
8.32	107	98	MSHD2-40 × 40	5
7.12	121	112	MHD2-40 × 40-1T1L	6
10.25	129	115	SHD2-40 × 40-1T1L	7
9.28	140	127	SHD-40 × 40-1T1L	8
5.35	125	119	MSHD2-40 × 40-1T1L	9

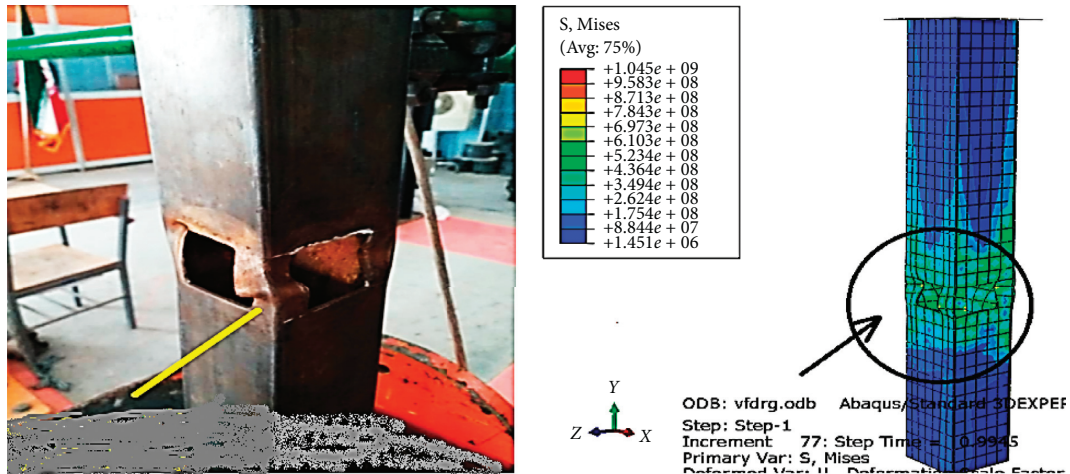


FIGURE 13: Comparison of a defective sample in two adjacent walls of a short steel column.

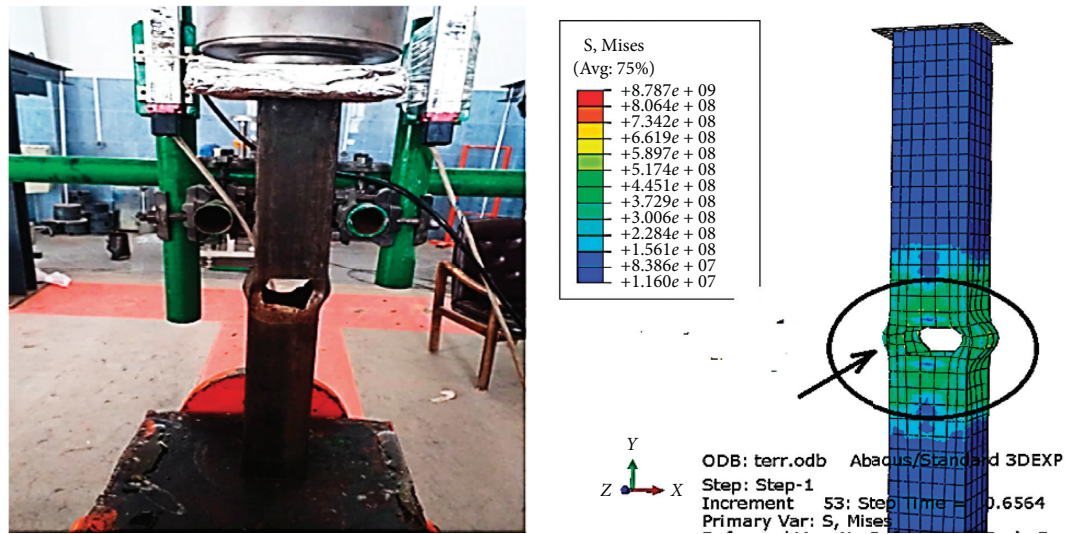


FIGURE 14: Comparison of a sample with defects in two walls in front of a short steel column [33].

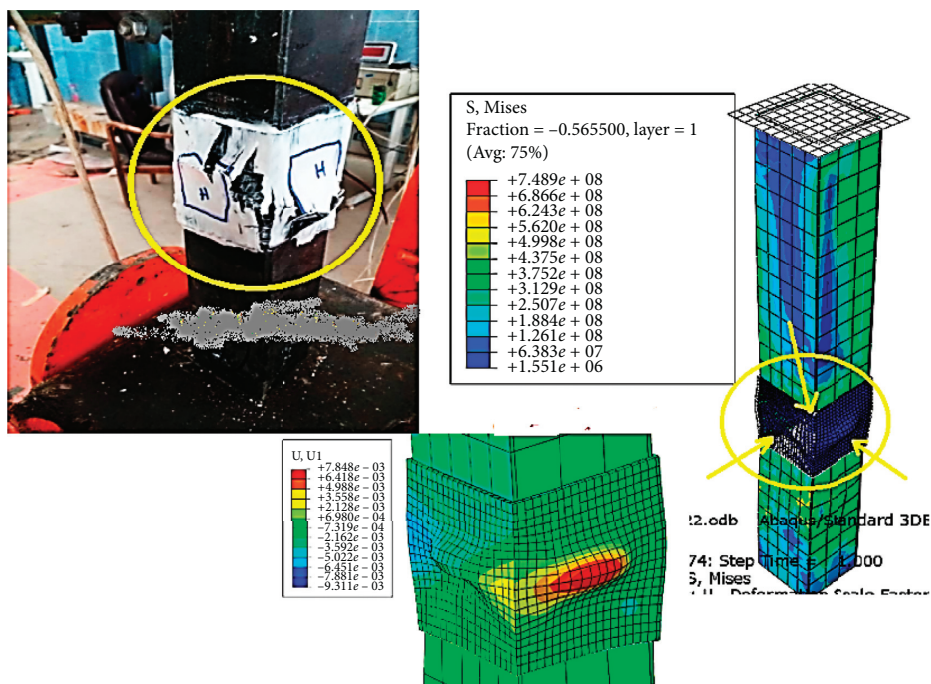


FIGURE 15: Comparison of the reinforcement of a defective sample in two adjacent walls of a short steel column.

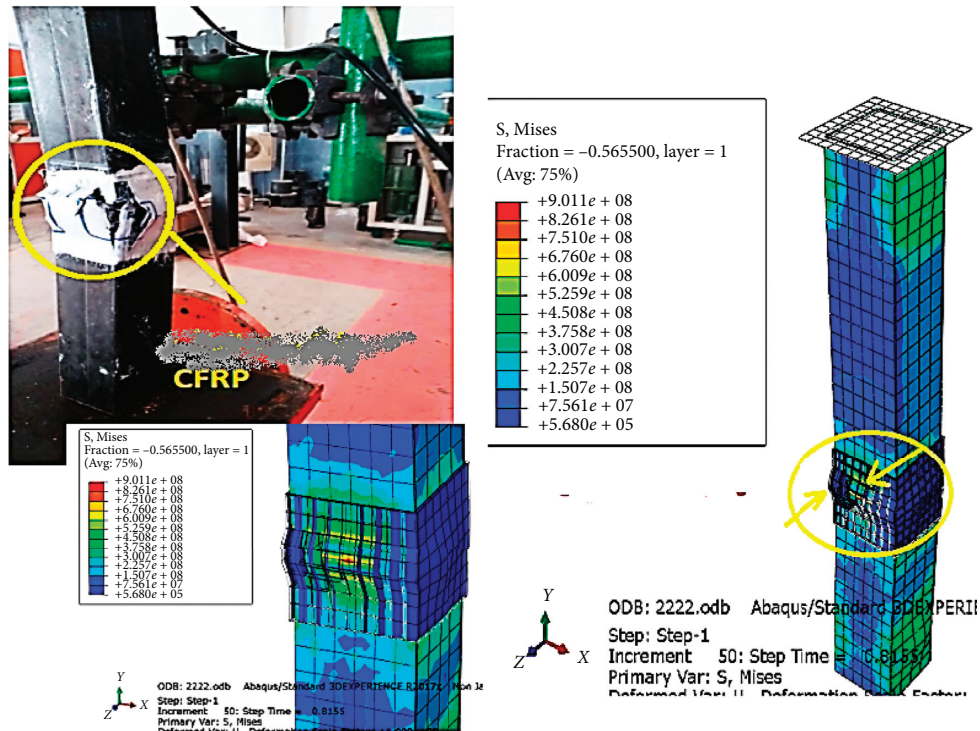


FIGURE 16: Comparison of the reinforcement of a defective sample on the two sides of a box steel column.

TABLE 7: Bearing capacity of laboratory samples.

Carrying capacity (kN)	Sample name	Number
158	Control	1
112	MHD2-40 × 40	2
95	SHD2-40 × 40	3
128	SHD-40 × 40	4
107	MSHD2-40 × 40	5
121	MHD2-40 × 40-1T1L	6
129	SHD2-40 × 40-1T1L	7
140	SHD-40 × 40-1T1L	8
125	MSHD2-40 × 40-1T1L	9

the modeling indicated that FEM will have a high ability to simulate sections under axial load [17].

7. Conclusion

Damage to short steel columns increased deformation and rupture in the defect area during axial loading. Increasing the longitudinal dimensions of the defect showed that due to the compressive load, the resistance would decrease and the lateral deformations increase. The effect of corrosion (defect) on the two sides was much greater than the other samples and the deformation in this sample occurred significantly. A horizontal defect created on one side of the center of the box steel column reduced the bearing capacity to 128 kN. Also, this reduction in bearing capacity with two layers of CFRP up to 140 kN equal to 8.57% led to compensation. The horizontal defect created on both sides of the steel column

reduced the bearing capacity to 95 kN, and this reduction in bearing capacity with the two layers of CFRP increased to 129 kN. Longitudinal and transverse dimensions of the corrosion site in box steel columns have reduced the stiffness of the axial member. The use of two layers of CFRP sheet strengthened the metal column damaged by corrosion due to axial load. The stress distribution in all software models, in the place of force application and in the place of failure, was consistent with laboratory samples. The results of software and laboratory analysis were well matched and different from each other. Among the defects created in the reinforced sample, the highest resistance is related to sample No. 8 of Table 7, with a length and width of the defect of 4 mm, which increased the bearing capacity to 140 kN. The use of CFRP carbon fibers to increase the stiffness of the steel column has controlled local buckling and reduced rupture in the defective area.

Data Availability

The data used to support the findings of this study are available from the corresponding author upon request.

Conflicts of Interest

The authors declare that there are no conflicts of interest regarding the publication of this manuscript.

References

- [1] S. M. S. Kolbadi, H. Davoodian, and S. M. S. Kolbadi, "Evaluation of nonlinear behavior of reinforced concrete frames by explosive dynamic loading using finite element method," *Civil Engineering Journal*, vol. 3, no. 12, pp. 1–10, 2017.
- [2] G. Minafò, "A practical approach for the strength evaluation of RC columns reinforced with RC jackets," *Engineering Structures*, vol. 85, pp. 162–169, 2005.
- [3] M. Seyed, K. Seyed, M. Safi, K. Ayoub, S. M. S. Kolbadi, and M. Mirtaheeri, "Explosive performance assessment of buried steel pipeline," *Advances in Civil Engineering*, vol. 2021, Article ID 6638867, 24 pages, 2021.
- [4] K. G. Vandoros and S. E. Dritsos, "Concrete jacket construction detail effectiveness when strengthening RC columns," *Construction and Building Materials*, vol. 22, no. 3, pp. 264–276, 2008.
- [5] T. Kitada, T. Yamaguchi, M. Matsumura et al., "New technologies of steel bridges in Japan," *Journal of Constructional Steel Research*, vol. 58, no. 1, pp. 21–70, 2002.
- [6] K. A. Harries, A. J. Peck, and E. J. Abraham, "Enhancing stability of structural steel sections using FRP," *Thin-Walled Structures*, vol. 47, no. 10, pp. 1092–1101, 2009.
- [7] K. A. Harries, A. Peck, and E. J. Abraham, "FRP-stabilised steel compression members," in *Proceedings of the Fourth International Conference on FRP Composites in Civil Engineering*, Zurich, Switzerland, July 2008.
- [8] M. R. Bambach and M. Elchalakani, "Plastic mechanism analysis of steel SHS strengthened with CFRP under large axial deformation," *Thin-Walled Structures*, vol. 45, no. 2, pp. 159–170, 2007.
- [9] M. Bambach, H. H. Jama, and M. Elchalakani, "Static and dynamic axial crushing of spot-welded thin-walled composite steel—CFRP square tubes," *International Journal of Impact Engineering*, vol. 36, no. 9, pp. 1083–1094, 2010.
- [10] J. Haedir and X.-L. Zhao, "Design of short CFRP-reinforced steel tubular columns," *Journal of Constructional Steel Research*, vol. 67, no. 3, pp. 497–509, 2011.
- [11] S. Kalavagunta, S. Naganathan, and K. N. Bin Mustapha, "Proposal for design rules of axially loaded CFRP strengthened cold formed lipped channel steel sections," *Thin-Walled Structures*, vol. 72, pp. 14–19, 2013.
- [12] M. A. Hadianfard, S. Malekpour, and M. Momeni, "Reliability analysis of H section steel columns under blast loading," *Structural Safety*, vol. 75, pp. 45–56, 2018.
- [13] M. Liu and M. Dawood, "Reliability analysis of debonding in steel beams strengthened with externally bonded CFRP composites," *Journal of Composites for Construction*, vol. 23, no. 1, pp. 65–70, 2019.
- [14] J. G. Teng, T. Yu, and D. Fernando, "Strengthening of steel structures with fiber-reinforced polymer composites," *Journal of Constructional Steel Research*, vol. 78, pp. 131–143, 2012.
- [15] J. G. Teng and Y. M. Hu, "Enhancement of seismic resistance of steel tubular columns by FRP jacketing," in *Proceedings of the 3rd International Conference on Composites in Construction*, pp. 11–13, Lyon, France, July 2005.
- [16] A. Tanabandeh and P. Gardoni, "Probabilistic capacity models and fragility estimates for RC columns retrofitted with FRP composites," *Engineering Structures*, vol. 74, pp. 13–22, 2014.
- [17] M. R. Bambach and M. Elchalakani, "Plastic mechanism analysis of steel SHS strengthened with CFRP under large axial deformation," *Thin-Walled Structures*, vol. 45, no. 2, pp. 159–170, 2007.
- [18] D. Zhang, Q. Wang, and J. Dong, "Simulation study on CFRP strengthened reinforced concrete beam under four-point bending," *Computers and Concrete*, vol. 17, no. 3, pp. 407–421, 2016.
- [19] H. Yang and A. Wang, "Dynamic stability analysis of pipeline based on reliability using surrogate model," *Journal of Marine Engineering & Technology*, vol. 12, no. 2, pp. 75–84, 2014.
- [20] S. M. Seyed Kolbadi, H. Piri, K. Ali, S. Mahdi Seyed-Kolbadi, and M. Mirtaheeri, "Nonlinear seismic performance evaluation of flexural slotted connection using endurance time method," *Shock and Vibration*, vol. 2020, Article ID 8842230, 15 pages, 2020.
- [21] K. Ha, "Innovative blade trailing edge flap design concept using flexible torsion bar and worm drive," *Hightech and Innovative Journal*, vol. 1, no. 3, pp. 12–20, 2020.
- [22] A. P. Pinheiro, "Architectural rehabilitation and sustainability of green buildings in historic reservation," *Hightech and Innovative Journal*, vol. 1, no. 4, pp. 26–44, 2020.
- [23] N. Kabashi, B. Avdyli, E. Krasniqi, and A. Këpuska, "Comparative approach to flexural behavior of reinforced beams with GFRP," *CFRP and Steel Bars, civil engineering Journal*, vol. 6, no. 1, pp. 32–50, 2020.
- [24] D. He, J. Dong, Q. Wang, and X. Chen, "Mechanical behaviour of recycled concrete filled steel tube columns strengthened by CFRP," in *Proceedings of the Paper presented at the 2nd International Conference on Multimedia Technology*, Hangzhou, China, March 2001.
- [25] P. Feng, Y. Zhang, Y. Bai, and L. Ye, "Strengthening of steel members in compression by mortar-filled FRP tubes," *Thin-Walled Structures*, vol. 64, pp. 1–12, 2013.
- [26] T. Georgia, P. Vassilis, and K. Andreas, "Flexural behaviour of reinforced concrete jacketed columns under reversed cyclic loading," *Engineering Structures*, vol. 50, pp. 432–443, 2014.
- [27] L. H. Han, G. H. Yao, and X. L. Zhao, "Tests and calculations for hollow structural steel (HSS) stub columns filled with self-consolidating concrete (SCC)," *Journal of Constructional Steel Research*, vol. 61, pp. 1241–1269, 2015.
- [28] H. Karagah, C. Shi, M. Dawood, and A. Belarbi, "Experimental investigation of short steel columns with localized corrosion," *Thin-Walled Structures*, vol. 87, pp. 191–199, 2015.
- [29] N. Metropolis and S. Ulam, "The Monte Carlo method," *Journal of the American Statistical Association*, vol. 44, no. 247, pp. 335–341, 1949.
- [30] A. S. Nowak and K. R. Collin, *Reliability of Structures*, McGraw-Hill, New York, NY, USA, 2000.
- [31] M. R. Ghaemdoust, K. Narmashiri, and O. Yousefi, "Structural behaviors of deficient steel SHS short columns strengthened using CFRP," *Construction and Building Materials*, vol. 126, pp. 1002–1011, 2016.
- [32] J. F. Dong, Q. Y. Wang, and Z. W. Guan, "Structural behaviour of recycled aggregate concrete filled steel tube

columns strengthened by CFRP,” *Engineering Structures*, vol. 48, pp. 532–542, 2013.

- [33] G. G. Prabhu and M. C. Sundararaja, “Behaviour of concrete filled steel tubular (CFST) short columns externally reinforced using CFRP strips composite,” *Construction and Building Materials*, vol. 47, pp. 1362–1371, 2013.

Research Article

Groundwater Single- and Multiobjective Optimization Using Harris Hawks and Multiobjective Billiards-Inspired Algorithm

AbdolGhafour Gerey , Amirpouya Sarraf , and Hassan Ahmadi 

Civil Engineering Department, Roudehen Branch, Islamic Azad University, Roudehen, Iran

Correspondence should be addressed to Amirpouya Sarraf; sarraf@riau.ac.ir

Received 30 May 2021; Revised 9 June 2021; Accepted 14 June 2021; Published 30 June 2021

Academic Editor: S. Mahdi S. Kolbadi

Copyright © 2021 AbdolGhafour Gerey et al. This is an open access article distributed under the Creative Commons Attribution License, which permits unrestricted use, distribution, and reproduction in any medium, provided the original work is properly cited.

This is the first attempt to combine the Multiobjective Billiards-Inspired Optimization Algorithm (MOBOA) with groundwater modelling to determine pumping rates within a well-distributed range of Pareto options. In this study, in order to determine an optimum solution for groundwater drawdown, pumping rates were selected accompanied by three minimization objectives: minimizing shortage influenced by inability to supply, adjusted shortage index, and minimizing the degree of drawdown within predefined areas. To optimize hydraulic conductivity and specific yield parameters of a modular three-dimensional finite-difference (MODFLOW) groundwater model, the Harris Hawks optimization algorithm was used to minimize the sum of absolute deviation between observed and simulated water-table levels. MOBOA was then utilized to optimize pumping rate variables for an Iranian arid to semiarid groundwater environment using these parameters. As the study results, when the maximum and minimum aquifer drawdown was specified in the range of -40 to $+40$ cm/year, the Pareto parameter sets produced satisfactory results. Overall, the “Simulation-Optimization-Modelling” protocol was able to generate a series of optimal solutions that were shown on a Pareto front. The study concluded to an optimum approach that provides policy makers in the Iranian water stressed zones with safe groundwater management alternatives.

1. Introduction

Groundwater behaviour modelling is one of the critical mechanisms that hydrogeologists have been attempting to measure since long time ago in order to solve evolving groundwater issues [1]. Due to the dynamic and multi-objective nature of the groundwater system, simulation of the groundwater system is challenging, especially in arid to semiarid zones. In the issue of rising groundwater demand, new models are desperately needed to develop novel decision-making tools and improve aquifer system drawdown [2]. Groundwater simulations have traditionally been conducted with the use of simulation/optimization algorithms [3, 4]. These models have been used to address construction and process issues of groundwater hydraulic control, water supply, and remediation [5, 6]. Professional experience with groundwater mechanism calibration shows which the single-objective functions are often insufficient to accurately

quantify all dimensions and features of a groundwater system. Since sustainability managing is inherently a multi-objective issue, no optimum solutions can be determined in the conventional context, and policy makers can articulate their favourites through a collection of nondominated solutions [7].

To consider the multiobjective existence of groundwater systems, one approach is to specify multiple optimization objective functions that quantify different characteristics of system action. They employ a multiobjective optimization tool to find a collection of nondominated solutions named as Pareto best approaches [8, 9]. The Pareto solutions reflect trade-offs among various incommensurable and often competing goals, with the property that switching from one solution to another improves one while deteriorating one or more others [10]. In groundwater research, there are many literature studies relating to the use of either deterministic or stochastic optimization approaches. Linear programming,

nonlinear programming, and dynamic programming are examples of deterministic optimization approaches. Several academics have followed these approaches [11, 12]. The standard part of optimization techniques, known as meta-heuristic algorithms, comprises genetic algorithms (GA), particle swarm optimization (PSO), simulating annealing, and others. These approaches were applied to extremely nonlinear or multimodal issues with a variety of dynamic constraints in order to improve groundwater characteristics in various regions [13].

Many attempts have been made in the literature to address multiobjective optimization of groundwater management issues. Park and Aral [14] proposed a multiobjective optimization method for determining coastal well positions that enhances pumping rates while minimizing the distance between the sensitive stagnation point and the reference coastline position. Reed et al. [15] developed a multiobjective strategy to cost-effective long-term groundwater monitoring using an Elitist nondominated sorted GA. In Italy, Giustolisi and Simeone [5] devised a method for assessing the complicated relationship between precipitation and water level in shallow unconfined aquifers. Siegfried et al. [16] proposed a multiobjective algorithm for optimizing pumping facility positioning and operation over time.

Saafan et al. [17] optimized pumping rates in Egypt's El-Farafra oasis by combining a multiobjective genetic algorithm optimization model with MODFLOW. They forecast maximum pumping rate and minimum operation costs, as well as potential improvements in both variables. The above algorithms have concentrated on using a single genetic algorithm technique to calculate groundwater properties, which cannot be appropriate for large-scale groundwater systems. While working with a large-scale and complex structure, multiple competing priorities can occur, resulting in a rapid increase in the number of decision variables based on the problem scale. In such cases, single-objective approaches can produce unsatisfactory results for decision makers, necessitating the search for multiple optimization solutions. Many optimization domains include multidimensional problems that can only be solved concurrently by constructing different optimization algorithms.

El-Ghandour and Elsaid [12] suggested a steady-state analytical solution in a homogeneous unconfined aquifer using the particle swarm optimization (PSO) method to optimize and solve the groundwater management problem. They tested the proposed model on a popular hypothetical example to maximize the total pumping rate from located well system at steady-state condition. The results showed the superiority of the proposed model to obtain the maximum pumping rate compared with other methods of previous work.

It is the first research to combine a new multiobjective optimization algorithm called as Multiobjective Billiards-Inspired Optimization Algorithm (MOBOA) developed by Kaveh et al. [18] with MODFLOW to optimize pumping rates within a well-distributed range of Pareto approaches. The aim of the study was to determine the optimum approaches to meet the highest demand for arid

to semiarid groundwater managing. Three minimization objectives were employed to optimize the pumping rates: minimizing the amount of drawdown within predefined Pareto zones, decreasing the shortage caused by an inability to supply, and decreasing the Modified Shortage Index (MSI).

Sadeghi-Tabas et al. [19] tried to link the multialgorithm genetically adaptive search method (AMALGAM) with a groundwater model to define pumping rates within a well-distributed set of Pareto solutions. The pumping rates along with three minimization objectives, i.e., minimizing shortage affected by the failure to supply, modified shortage index, and minimization of extent of drawdown within prespecified regions, were chosen to define an optimal solution for groundwater drawdown and subsidence in an arid groundwater system, Iran. The result was that the "Modeling-Optimization-Simulation" procedure was capable to compute a set of optimal solutions displayed on a Pareto front. In addition, the proposed optimal solution provides sustainable groundwater management alternatives to decision makers in arid region.

In addition, combination of MODFLOW with an advanced swarm-intelligence-based algorithm as the Harris Hawks optimization algorithm (HHO) developed by Abdel-Basset et al. [20] to calculate aquifer hydrodynamic parameters using an automated search process was the first innovation issue of this study. Therefore, The HHO approach's capability resulted in more reliable calculations in error variance. In addition, it assisted in characterizing groundwater processes at each zone. Therefore, the aquifer properties were optimized in a highly parameterized model by developing the HHO approach within the groundwater numerical model.

The second aspect of innovation developed in this research (i.e., as the second step) was to identify optimal Pareto solutions for groundwater drawdown using a novel multiobjective algorithms named as the Billiards-Inspired Multiobjective Optimization Algorithm (MOBOA) model.

The recent optimization algorithm application guaranteed the groundwater control over an arid to semiarid area in Northeast of Iran.

In Figure 1, the procedure used in this research is illustrated graphically.

2. Material and Methods

2.1. Geographical Location of the Research Field. The Gorgan Plain is located in the arid to semiarid zone of Golestan Province, Iran. The Gorgan Plain aquifer system is located in the latitude and longitude of $36^{\circ} \text{ W } 37'$ to $37^{\circ} \text{ W } 27'$ North and $53^{\circ} \text{ W } 51'$ to $54^{\circ} \text{ W } 51'$ East (Figure 2). It encompasses an area of around 4393 km^2 . The Gorgan Plain is categorized as an arid to semiarid zone by the DoMarton climatic classification, with mean annual rainfall and temperature of 254 millimeters and 19°C , respectively. According to the mean sea level, the maximum and minimum elevations are 150 and -26 meters, respectively. The plain's slope is steep in the south and mild in the north [21] Figure 1 illustrates the Gorgan Plain aquifer's geographical location.

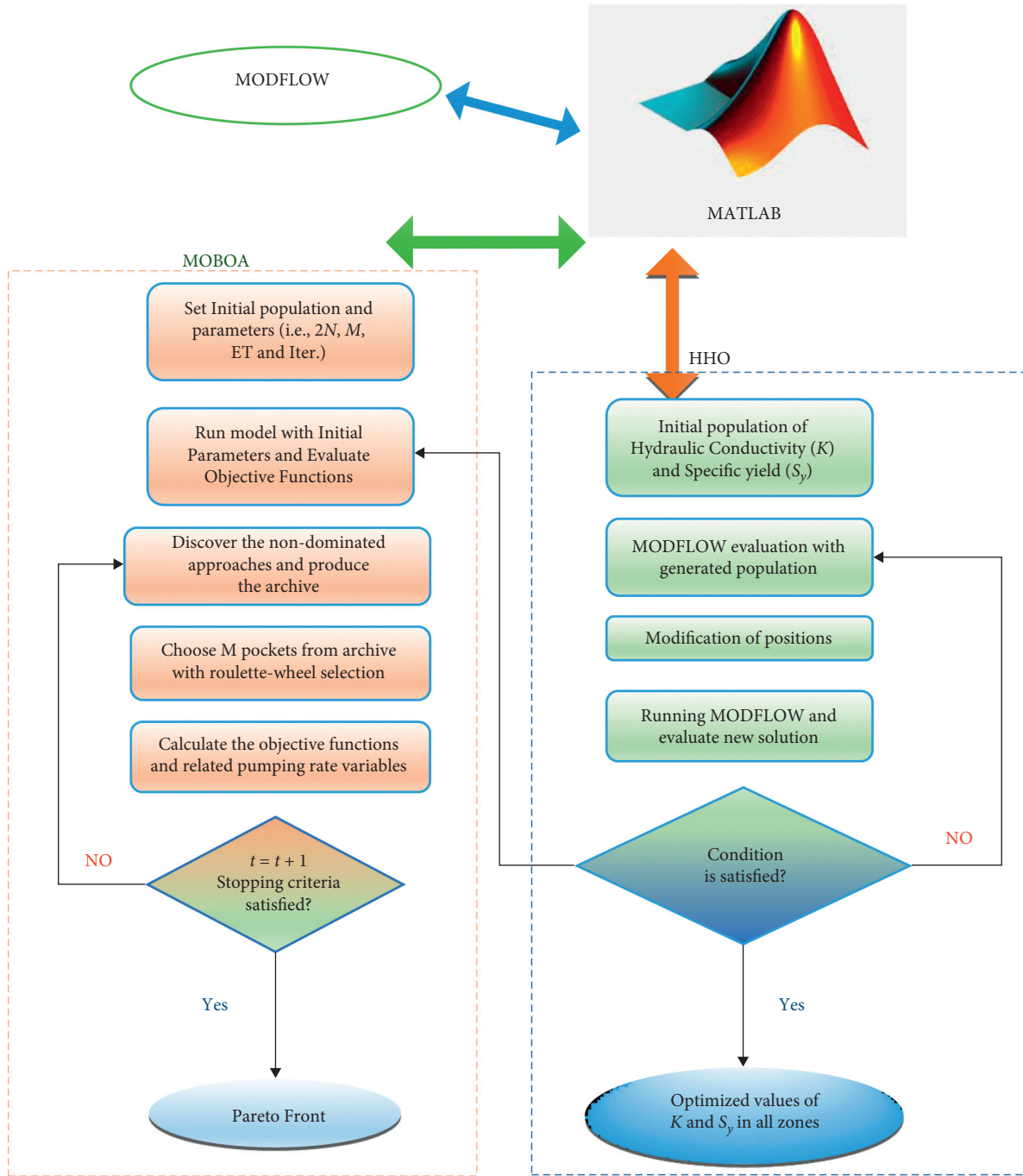


FIGURE 1: The flowchart of research methodology.

The aquifer’s bedrock is mainly hard rock in the south and saline water in the middle and northern parts. The majority of the land in the north is young alluvial fans, and clay flat stretches from the south to the north. The study area is mountainous in the south, and deserts and fine Caspian Sea sediments cover the western and northern regions. Agriculture tends to have the largest demand for water from March to July, with a subsequent decrease in demand. Furthermore, throughout the summer, drinking demand increases moderately, while industrial demand remains nearly steady during the year.

2.2. *Groundwater Modelling.* The mathematical solution of the groundwater model solves the math form of the mass balance equation in one area and generates a generally continuous approach to the surrounds. Every parameter value in terms of surface, volume, or time is represented by a distinct portion of the mass balance equation. In summary, a groundwater simulation mathematical model consists of a set of numeric value for different indicators in the balance equation. In other words, the balance equation is constructed for a specific aquifer zone, but it is generalized to the entire field [21]. Moreover, the results of groundwater

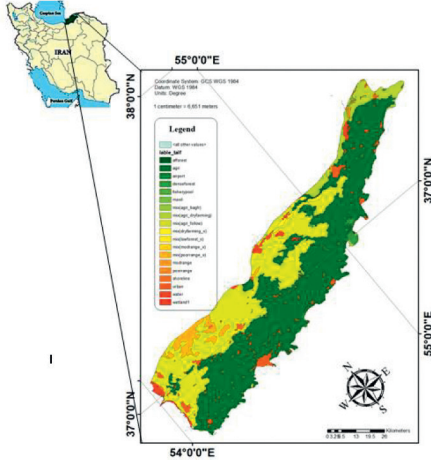


FIGURE 2: The Gorgan Plain aquifer's geographical location.

modelling can be influenced by numerous mistakes, such as those caused by the groundwater conceptual model, the estimated solution of groundwater factors, and unexplained interactions between numerous factors and features. In fact, establishing a groundwater computational model necessitates the collection of various parameters such as hydraulic conductivity (k), transmissivity, and storage coefficient (or specific yield (S_y)). Groundwater modelling can produce a range of errors and misfits due to the scarcity of hydrogeology data (particularly in groundwater stressed regions), the heterogeneity of parameters in space and time, inaccurate configuration of aquifer characteristics (location, type, number of layers, distribution, etc.), and the scaling impact of variables. Since the numerical model is based on a conceptual model, therefore, the groundwater conceptual models frequently simplify real-world hydrogeology settings improperly [22]. Physical stability in groundwater mass and energy flows, which is a continuity mechanism, is usually described to allow predictions at discrete time points. All of these variables and complexity contribute to simulation bias and error, posing a challenge to modelling the groundwater problems, especially in arid to semiarid regions as the most groundwater stressed areas.

2.3. Governing Flow Equations of Groundwater Modelling. In groundwater simulation, the governing equation takes the following general form [22]:

$$\frac{\partial}{\partial x} \left(k_x \frac{\partial h}{\partial x} \right) + \frac{\partial}{\partial y} \left(k_y \frac{\partial h}{\partial y} \right) + \frac{\partial}{\partial z} \left(k_z \frac{\partial h}{\partial z} \right) = S_s \frac{\partial h}{\partial t} \pm R. \quad (1)$$

In which, k_x , k_y , and k_z are hydraulic conductivity tensors and h , S_s , and R are pressure head, specific storage, and recharge or discharge (positive and negative) aquifer elements, respectively. The thickness of the saturated layer of an unconfined aquifer correlates with groundwater level. Dupuit [22] considered that the horizontal flow should be governed in the whole aquifer as well as proportionality of the hydraulic gradient to the slope of the free surface [23]. The equation is based on Dupuit's assumption if the flow is

two-dimensional and transient, and the continuity equation is as follows [24]:

$$\frac{\partial}{\partial x} \left(k_x h \frac{\partial h}{\partial x} \right) + \frac{\partial}{\partial y} \left(k_y h \frac{\partial h}{\partial y} \right) + \frac{\partial}{\partial z} \left(k_z h \frac{\partial h}{\partial z} \right) = S_y \frac{\partial h}{\partial t}. \quad (2)$$

In which S_y represents the specific yield. The MODFLOW software was introduced in 1984 and has since been updated and improved to simulate in both steady and unsteady circumstances. A distributed hydrogeology model was developed in this study through using numerical data needed for simulating a functional relationship between prediction and observation data in order to model steady and unsteady-state conditions in the Gorgan Plain aquifer under various drawdown and control conditions.

2.3.1. Mathematical Representation of Aquifer Models. Izady et al. [24] suggested the method applied to construct the groundwater mathematical model in this analysis. The groundwater model, according to their approach, consists of the six following phases:

- (a) Acquiring all possible data;
- (b) Verifying and configuring control observations;
- (c) Identifying the geometry of the aquifer;
- (d) Primary estimate of the hydrodynamic parameters of the aquifer;
- (e) Description of the recharge and discharge values of the aquifer; and
- (f) Integrating the effects of previous phases producing the final conceptual model.

A one-layered unconfined aquifer with thicknesses ranging from 5 m to 55 m was examined as a conceptual groundwater model for the Gorgan Plain groundwater modelling. Surface elevation data, well logs, well locations and measurements, a geology map, hydrography, and recharge data were used to build the groundwater model. To identify the plain boundary situation, topography and geology maps were first used. The single optimization approach was then used to approximate the spatially distributed hydrodynamic characteristics. The temporal discharge difference was calculated in this analysis by pumping 33999 wells located inside the aquifer boundary (Figure 3). In Figure 3, the pumping well drilled in and distributed on Gorgan Plain aquifer has been shown. It should be noticed that this pumping well discharges the aforementioned aquifer.

In this analysis, seven data coverages were integrated into the MODFLOW model to create a groundwater numerical model, consisting of aquifer boundary circumstances, piezometers, pumping wells, surface recharges, drainage data, hydraulic conductivity, and specific yield. MODFLOW's boundary conditions are determined by using a constant head boundary, a head based flux (river, drain, and general-head boundaries), and a known flux (recharge, evapotranspiration, wells, and stream). Because of the differential hydraulic gradients across multiple areas, the

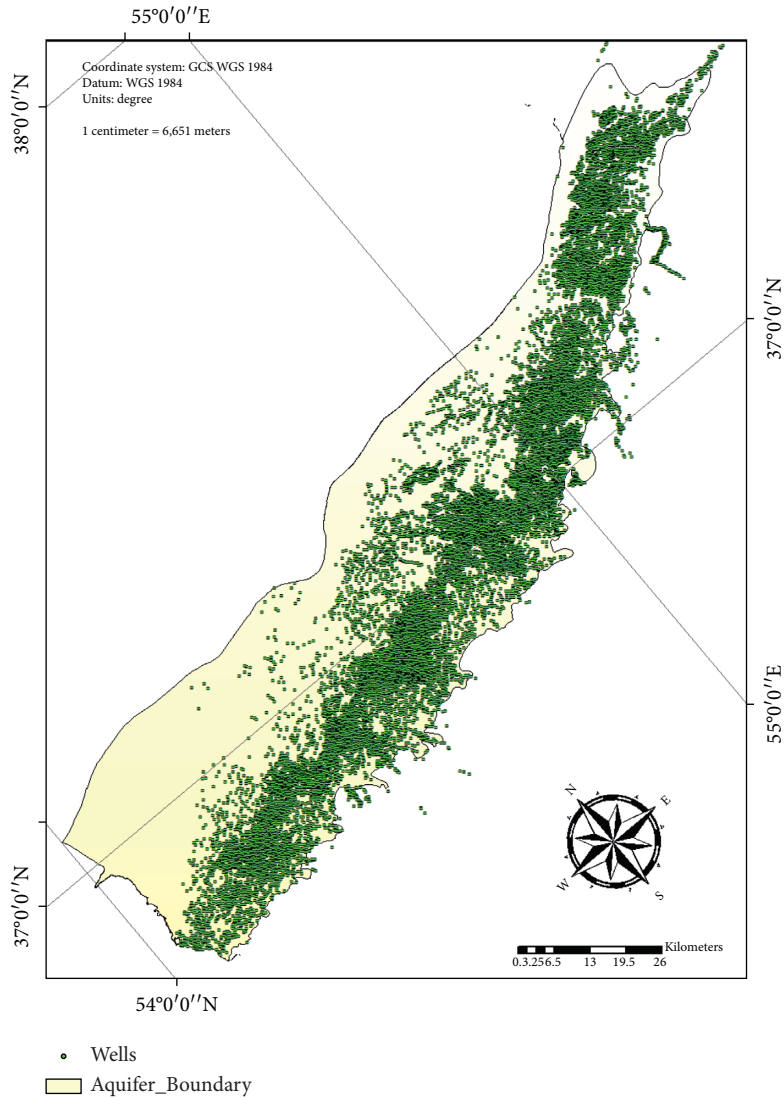


FIGURE 3: Pumping well drilled and distributed on Gorgan Plain aquifer and discharging it.

Gorgan Plain aquifer functions as a transient aquifer. In addition, this aquifer is recharged/discharged at inflow/outflow limits by adjacent aquifers, resulting in conditional and temporary results. In this research, water front entry cells or grids were used to identify recharge and discharge sites at inflow and outflow boundaries. For all of those borders, a specific-head-boundary state was considered to remain constant at each cell number in the model. As illustrated in Figure 3, only 281 of the 1340 observational wells with validated data, as monthly observed water-table level data, were utilized for calibration (Figure 4).

The number of pumping wells was 33999 pumping wells that consists of agricultural, drinking water, and industrial pumping wells. Furthermore, the aquifer contains 2764 springs and 336 Qantas, which entered in the MODFLOW. MODFLOW was originally simulated in steady state to describe homogeneous zones before being used to construct the aquifer model. The aquifer was separated into 30 homogeneous zones to determine hydraulic conductivity and specific yield values. In order to develop and construct a

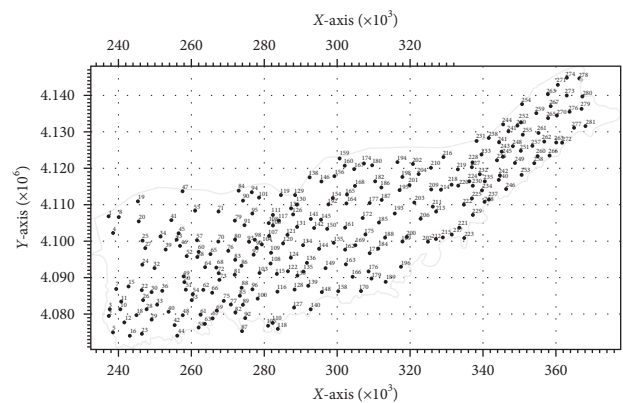


FIGURE 4: 281 observational wells used for simulation of the Gorgan Plain aquifer's water level.

groundwater model, numerous settings were given, including model network architecture, stress cycle and time step selection, determination of starting position, boundary

condition, and shape and number of saturated zones. To solve partial differential equation, the aquifer was separated into 7208 cells or grids due to geological heterogeneity. The plain's gridding was constructed with 60 rows and 140 columns such that each layer cell is squared to $250\text{ m} \times 250\text{ m}$ (Figure 5).

Cells outside of the aquifer boundary were then given a zero code, indicating that they have no influence on the simulation analysis. While individual model cell features may be set, combining cells with the same attributes into homogeneous zones significantly enhanced and simplified the modelling procedure. Figure 4 shows the modelled structure of the Gorgan Plain aquifer used by the MODFLOW model.

In this research, the modelling of groundwater flow in the Gorgan Plain was carried out over a one-year cycle, from October 2018 to September 2019 as the calibration period and from October 2019 to September 2020 as the validation period. 12-month tension cycles with a ten-day time phase were defined and used in the modelling methodology (i.e., for each stress cycle, three time measures were taken into account). To complete the numerical model, absolute values of bed rock depths, topography, and beginning water level data were interpolated by using the Kriging method and assigned to the network's cells.

2.4. Harris Hawks Optimization Algorithm as the Single-Objective Optimization Approach. Modeling the Harris Hawks hunting technique yielded the Harris Hawks optimization (HHO) algorithm [25], a novel nature-inspired method. The algorithm's operative and exploratory stages involve looking for prey, making a sudden pounce, and attacking in a variety of ways. The hunt is conducted at random using two exploring approaches. In the first way, Harris Hawks perch on a position that takes into account the positions of other family members and prey, whereas in the second way, the hawks wait on selected tall trees. Both strategies may be represented with the same probability of q as follows [20]:

$$x(t+1) = \begin{cases} x_r(t) - x_1 |x_r(t) - 2r_2 x(t)| & q \geq 0.5, \\ x_{\text{rabbit}}(t) - x_{\text{mean}}(t) - r_3(Lb + r_4(Ub - Lb)) & q < 0.5, \end{cases} \quad (3)$$

where $x(t)$ and $x(t+1)$ imply hawks' position vectors in the present and subsequent iteration, respectively. $x_r(t)$ is mentioned to a random hawk picked from the population. $x_{\text{rabbit}}(t)$ is the rabbit position. q , r_1 , r_2 , r_3 , and r_4 are the numbers that was arbitrarily produced. Ub and Lb are higher and lesser bounds to generate accidental positions of the hawks' habitat. $x_{\text{mean}}(t)$ implies the average position of hawks in the population which can be capable of being computed as follows [20]:

$$x_{\text{mean}}(t) = \frac{1}{h} \sum_{i=1}^h x_i(t), \quad (4)$$

where $x_i(t)$ implies the i -th position vector of each hawk at t -th iteration and $i = 1, \dots, h$. h is mentioned as the number of

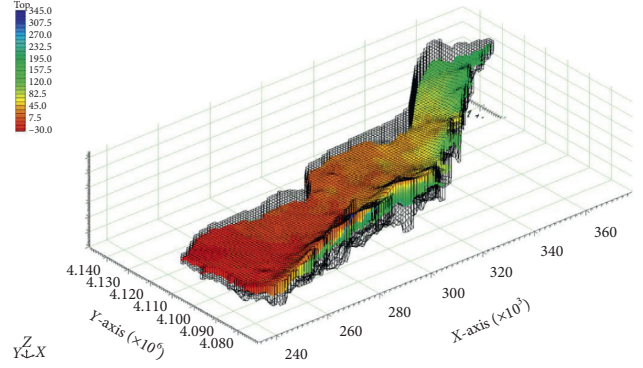


FIGURE 5: Gorgan Plain aquifer modelled by MODFLOW.

Harris Hawks' population. According to escape energy E or fleeing of the rabbit, the algorithm's transition from exploring to operation is possible as follows [20]:

$$E = 2E_0 \left(1 - \frac{t}{\text{Max_iter}} \right), \quad (5)$$

where E_0 denotes the primary rabbit energy randomly generated in $[-1, 1]$. Max_iter specifies the maximum number of iterations. When $E \geq 1$, hawks look for more regions to explore the rabbit's locations as the exploration phase; otherwise, the exploitation phase is activated. The description of the failure ($p < 0.5$) or success ($p \geq 0.5$) of the rabbit escape is accomplished in the algorithm, when the probability p is the same. Furthermore, a forceful ($E < 0.5$) or gentle ($E \geq 0.5$) besiege will be accomplished by hawks according to the rabbit energy. The gentle besiege can be expressed as follows [20]:

$$\begin{aligned} x(t+1) &= \Delta x(t) - E|J \times x_{\text{rabbit}}(t) - x(t), \\ \Delta x(t) &= x_{\text{rabbit}}(t) - x(t), \\ J &= 2(1 - \text{rand}), \end{aligned} \quad (6)$$

where $\Delta x(t)$ implies the dissimilarity between hawk and the rabbit positions, and the draw of the accidental strength of rabbit jump J is completed by employing an arbitrary amount of rand . The definition of the forceful besiege, on the other hand, is as follows [19]:

$$x(t+1) = x(t) - E|\Delta x(t)|. \quad (7)$$

If ($p < 0.5$) and ($E \geq 0.5$) and as the rabbit can effectively flee, gentle besiege with advance rapid dives is done. The best possible dive can be selected by the hawks.

2.5. Multiobjective Billiards-Inspired Optimization Algorithm.

This section provides an explanation of the basic principle of this novel physics-based metaheuristic. The mechanism of the Billiards-Inspired Multiobjective Optimization Algorithm is then outlined in the following section. The physics' natural laws and the Billiards game embedded in the clash of balls are the major genesis of the BOA. Vector algebra and conservation laws govern when the balls collide with other balls. The kinetic energies of balls are preserved during

collisions in perfectly elastic collisions, in addition to the sum of all angular velocity. Therefore, the following ultimate velocities of balls after crash in perpendicular and parallel directions to the impact line will be calculated as follows [18]:

$$\begin{aligned}
 \vec{v}'_1 &= v_{1,\parallel} \vec{e}' + \vec{v}'_{1,\perp}, \\
 \vec{v}'_2 &= v_{2,\parallel} \vec{e}' + \vec{v}'_{2,\perp}, \\
 v'_{1,\parallel} &= \frac{m_1 - m_2}{m_1 + m_2} v_{1,\parallel} + \frac{2m_2}{m_1 + m_2} v_{2,\parallel}, \\
 v'_{2,\parallel} &= \frac{2m_1}{m_1 + m_2} v_{1,\parallel} + \frac{m_2 - m_1}{m_1 + m_2} v_{2,\parallel},
 \end{aligned} \tag{8}$$

where v_1 and v_2 are the velocities of the first and 2nd balls during the collision and v'_1 and v'_2 are their velocities after the colliding. In addition, the symbols \parallel and \perp symbolize parallel and perpendicular elements, respectively. The masses of the balls are represented by the parameters m_1 and m_2 . The linking vector's unit vector is often denoted by \vec{e}' . It is worth noting that the velocities' perpendicular components stay constant, so the forces are merely directed to the collision axis, resulting in the perpendicular components of the angular velocities being preserved for balls. Therefore, the aforementioned equations indicate that if the masses of the balls are identical, the balls just transfer the parallel component of their velocities. The balls' velocity components during the crash are shown in Figure 6 [18]:

$$\begin{aligned}
 v'_{1,\parallel} &= v_{2,\parallel}, \\
 v'_{2,\parallel} &= v_{1,\parallel}.
 \end{aligned} \tag{9}$$

The final positions of bodies defined in this algorithm using the equations of kinematics in the event of continuous accelerating are as follows [18]:

$$\begin{aligned}
 x(t) &= x_0 + v_0 t + \frac{1}{2} a t^2, \\
 |v|^2 &= |v_0|^2 + 2|a||x - x_0|.
 \end{aligned} \tag{10}$$

2.6. Billiards-Inspired Multiobjective Optimization Algorithm. All of the solution approaches that comprise multiple decision variables are modelled as the multidimensional balls in this algorithm. These balls are the MOBOA's searching factors, and every dimension indicates a variable. In summary, the procedure begins with a random distribution of balls, and after that, it transfers nondominated strategies into an outside archive. Any members of the archive are chosen as pockets in each iteration. Following that, the balls are split into two collections: regular and cue balls. Every cue ball strikes its targeted ball, causing it to travel into a pocket. Whenever cue balls collide with each other, collision rules and vector algebra take over determining the movement of collided balls as well as their final status. MOBOA's phases are illustrated below, and its pseudocode is shown in Figure 7 [18].

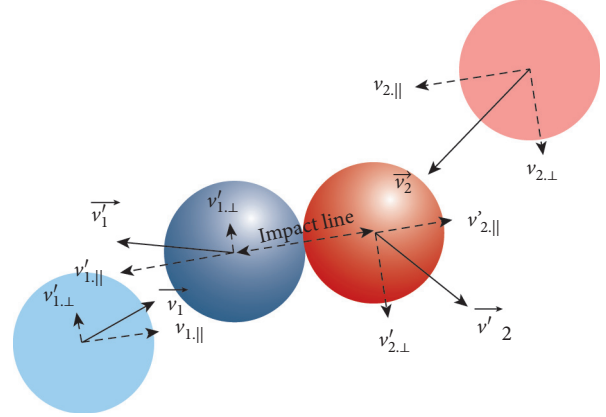


FIGURE 6: Velocity components of the balls during the crash [18].

```

Set      2N = number of balls;
         M = number of pockets;
         ET = escaping threshold;
         iter = 0;
Initialize 2N random bodies by equation (11);
Evaluate all balls according to objective functions;
Find the non-dominated solutions and create the repository;
Select M pockets from repository using roulette-wheel selection;
while (iter < Maximum number of iterations)
    iter = iter + 1;
    Sort the population based on maximum fitness values;
    Create ordinary ball and cue ball groups;
    for each pair ball
        for each pocket
            Calculate shot score by equation (14);
        end
        Assign the best pocket to current pair ball;
        Update the position of current ordinary ball by equation (16);
        Regenerate the violated dimensions of the ordinary ball;
        Calculate the velocities of current pair ball by equations (17) and (18);
        Update the position of current cue ball by equation (19);
        Regenerate the violated dimensions of the cue ball;
    if (rand < ET)
        Regenerate a random dimension of current pair ball by
        equation (20);
    End
end
Evaluate all the bodies according to the objective functions;
Extract non-dominated solutions and Update the repository;
Update the pockets using roulette-wheel selection;
end
Return the repository as the optimal Pareto front.

```

FIGURE 7: The MOBOA pseudocode [18].

2.6.1. Phase 1: Initialization. In the search space, the initial population of multidimensional balls is generated at random as follows [18]:

$$x_i^0 = x_{\min} + \text{rand}_{[0,1]} (x_{\max} - x_{\min}), \quad i = 1, 2, 3, \dots, 2N. \tag{11}$$

In which, x_i^0 is the i th ball initial value. The vectors of variables x_{\max} and x_{\min} represent the maximum and minimum permissible values. $\text{rand}[0,1]$ is an arbitrary variable, ranged by $[0, 1]$, as well as the population number is defined by $2N$.

2.6.2. Phase 2: Evaluation of Population. The objective functions each ball $[f(x) = f_1(x), f_2(x), \dots, f_k(x)]$ T should be evaluated [18].

2.6.3. Phase 3: Use an External Archive. The archive's first mission is to save the best nondominated approaches discovered till now. All existing nondominated solutions are added to the archive in each iteration, whereas dominated solutions are deleted. To keep the archive size limit, a gridding process is being contemplated, which divides the objective space into hypercubes. When the archive capacity exceeds the maximum size limit, certain approaches in the packed hypercube are removed and some new solutions are added. This procedure broadens the range of the estimated Pareto front. The repository's 2nd job is to include any candidates that deserve to be pockets [18].

2.6.4. Phase 4: Identifying the Pockets. Any representatives of the archive are chosen as pockets by means of the roulette-wheel selection approach. Equation (12) defines the suggested chance for selecting a hypercube to randomly draw a pocket [18]:

$$P_i = \frac{e^{-\beta n_i}}{\sum_j e^{-\beta n_j}}, \quad (12)$$

where β is the greater-than-zero selection pressure and n_i defines the amount of solutions in the i th hypercube. As a result, staying in a less populated region enhances the chances of getting a hypercube. It should be noted that the user determines the amount of pockets, and these pockets increase the algorithm's exploiting potential.

2.6.5. Phase 5: Arranging the Balls. In each iteration, the solution candidates are ordered in ascending order using the maximum strategy. An approach having a lower maximum value of fitness is more suitable because it is found in sparse regions. For the j th solution, the maximum fitness value is determined as follows [18]:

$$\text{fitness}^j = \max\{\min\{f_k(x_i) - f_k(x_j)\}, k = 1, 2, \dots, k\}, \quad i = 1, 2, \dots, 2Ni \neq j. \quad (13)$$

Following that, the ordered population is split into two equivalent classes (N pairs): (1) the upper and (2) the lower half as the regular and cue balls, respectively. Every cue ball corresponds to its pair in the regular balls category. This clustering approach creates the ideal situation for cue balls to exploit good-positioning regular balls.

2.6.6. Phase 6: Assigning Pockets to Balls. The lengths and cut angles between the balls and the pockets are used to assign the pockets to each pair of balls. These factors are taken into account while calculating the regarded shot score, which is calculated as follows [18]:

$$\text{Shot}_i^m = \frac{\cos \theta}{\overrightarrow{x_{(i+N)} x_i} \cdot \overrightarrow{x_i P_m}}, \quad i = 1, 2, 3, \dots, N, \quad m = 1, 2, \dots, M. \quad (14)$$

The shot score between the i th pair of balls and the m th bag is defined by Shot_i^m . $\overrightarrow{x_{(i+N)} x_i}$ and $\overrightarrow{x_i P_m}$ are the i th regular ball and i th cue ball positions, correspondingly. In addition, P_m denotes the location of the m th bag, and M denotes the number of pockets. And the cosine of the cut angle is determined by $\cos \theta$, and it is measured using the following equation:

$$\cos \theta = \frac{\overrightarrow{x_{(i+N)} x_i} \cdot \overrightarrow{x_i P_m}}{\|\overrightarrow{x_{(i+N)} x_i}\| \|\overrightarrow{x_i P_m}\|}. \quad (15)$$

In which the dot product is denoted by the symbol “.”; based on the measured scores, all pair of balls is assigned to the highest scoring pocket. Another choice is to use the roulette-wheel selection method to calculate the pockets for every pair of balls [18].

2.6.7. Phase 7: Population Updating. Finally, a collision occurs between cue balls and regular balls. Regular balls are then driven into pockets by cue balls. As indicated by the equations below [18], the new locations of regular balls following collisions are near their pockets:

$$x_{i,j}^{\text{new}} = P_{m,j}^i + \text{rand}_{[-\text{EROR}, \text{EROR}]}(x_{i,j}^{\text{old}} - P_{m,j}^i), \quad (16)$$

$$\text{EROR} = 1 - \frac{\text{iter}}{\text{iter}_{\text{max}}}.$$

In which $x_{i,j}^{\text{new}}$ and $x_{i,j}^{\text{old}}$ are the new and old values of the i th regular ball's j th vector, respectively. The $P_{m,j}^i$ vector is the j th variable of the m th pocket belonging to the i th pair of balls. The error rate is denoted by EROR; in addition, the iteration number and maximum iteration number are denoted by iter and iter_{max} , respectively. $\text{rand}[-\text{EROR}, \text{EROR}]$ is an arbitrary number between $[-\text{EROR}, \text{EROR}]$ [18]. Determining the ultimate location of cue balls following a collision is dependent on certain prerequisites, such as calculating the velocity of regular and cue balls. The velocity of the regular balls following the impact is shown as follows [18]:

$$\overrightarrow{v}_i = \sqrt{2a \cdot \overrightarrow{x_{i,j}^{\text{old}} x_{i,j}^{\text{new}}} \cdot \overrightarrow{x_{i,j}^{\text{old}} x_{i,j}^{\text{new}}}}. \quad (17)$$

In which \overrightarrow{v}_i is the velocity of the i th normal body following the crash, and $\overrightarrow{x_{i,j}^{\text{old}} x_{i,j}^{\text{new}}}$ is the i th body's displacement vector. It is worth noting that the symbol “ \cdot ” denotes a corresponding unit vector. The acceleration rate is defined by the parameter a , which is set to one. Cue ball velocities are calculated as follows [18]:

$$\vec{v}_{(i+N)} = \frac{\vec{v}_i}{x_i^{\text{old}} x_i^{\text{new}} \cdot x_{(i+N)}^{\text{old}} x_i^{\text{old}}}, \quad (18)$$

$$\vec{v}_{(i+N)} = \vec{v}_{(i+N)} - \vec{v}_i.$$

In which $\vec{v}_{(i+N)}$ and \vec{v}_i are the i th cue ball's velocities during the crash, correspondingly. In conclusion, the changed positions of the cue balls are calculated as follows [18]:

$$\vec{x}_{(i+N)}^{\text{New}} = \vec{x}_i^{\text{old}} + \omega \frac{\vec{v}_{(i+N)}}{2a} \vec{v}_{(i+N)}. \quad (19)$$

In which the factor ω determines a reducing variable that controls the movement of cue balls and has an initial value in the range [0, 1]. Figure 8 depicts the ball updating process.

2.6.8. Phase 8: Breaking Free from Local Optima. An escape limit, such as EL inside (0, 1), is known to avoid trapping in local optima. EL is compared to rand for each updated ball that is an arbitrary number regularly spread within (0, 1). If rand EL, the updated ball's random dimension is regenerated as [18]

$$x_{i,j} = x_{\min,j} + \text{rand}(x_{\max,j} - x_{\min,j}), \quad i = 1, 2, 3, \dots, 2N. \quad (20)$$

2.6.9. Phase 9: Evaluate the Boundary Restrictions. The ultimate location of balls may be put outside of the permissible ranges during the method of updating the location of balls. The dimensions of the balls that have been violated must be regenerated in this situation [18].

2.6.10. Phase 10: Evaluating the Termination Criteria. After a certain number of iterations, the search process will be terminated. If the condition is not met, the procedure is restarted at phase 2 [18]. This study used 5,000 function evaluations of 50 population sizes for optimization reasons. Then, to provide a reliable and computationally effective method to multiobjective optimization problems, 12 monthly discharge parameters were employed. After about 3,000 simulation cycles, the model met the convergence criterion. Pumping rates, as well as three minimization objectives, namely, minimizing shortages caused by a failure to supply, MSI, and minimizing the drawdown amount within predefined areas, were afterward selected to identify the best result for groundwater drawdown.

2.7. Developing the MODFLOW-HHO-MOBOA Structure. The MODFLOW-HHO-MOBOA framework is established. A simulator-optimizer model in the MATLAB software was used to evaluate and calculate aquifers' properties. The simulator model (i.e., MODFLOW) and the optimizer algorithms (HHO-MOBOA) should be coupled in order to calibrate the aquifer's hydrodynamic parameters and

calculate pumping rates, and therefore, simulator model and the optimizer algorithms were linked by developing the interface subfunction in MATLAB that contributes to the simulator-optimizer model. In this research, Theo Ols-thoorn's [26] MODFLOW simulator model was used throughout the MATLAB platform (mfLab program). The MF2005NWT (MODFLOW-2005, Newton-Raphson formulation) software, which includes the Newton-Raphson solver to improve the outcome of unconfined groundwater-flow problems, as well as the Upstream Weighting Package (UPW), was also employed in this investigation for numerical solutions. UPW was used to determine aquifers' features governing flow movement between cells in the MF 20005-NWT and MF-OWHM (MODFLOW-2005, One Water Hydrologic Flow Model) methods.

The MOBOA algorithmic was run by introducing an initial population and setting the algorithm parameters. This population is spread through a set of calculation nodes, which run the simulation model and calculate the objective function of the points obtained. The optimization process will be accomplished according to the flowchart proposed until the stopping criteria are encountered (Figure 1).

2.8. Evaluation of Model Results. Mean error (ME), mean absolute error (MAE), root mean square error (RMSE), and normalized root mean square error (NRMSE; nondimensional variants of the RMSE) were all utilized as criteria throughout the calibration procedure. ME, MAE, and RMSE/NRMSE all indicate error in the units (or squared units) of the constituent of interest, which aids in data interpretation [27, 28, 29]. The following equations (equations (21)–(24)) were used to estimate error:

$$\text{ME} = \frac{\sum_{t=1}^m \sum_{i=1}^m (h_{oi}^t - h_{si}^t)}{n * m}, \quad (21)$$

$$\text{MAE} = \frac{\sum_{t=1}^m \sum_{i=1}^m |h_{oi}^t - h_{si}^t|}{n * m}, \quad (22)$$

$$\text{RMSE} = \sqrt{\frac{\sum_{t=1}^m \sum_{i=1}^m (h_{oi}^t - h_{si}^t)^2}{n * m}}, \quad (23)$$

$$\text{NRMSE} = \sqrt{\frac{\sum_{t=1}^m \sum_{i=1}^m (h_{oi}^t - h_{si}^t)^2}{\sum_{t=1}^m \sum_{i=1}^m (h_{oi}^t - \bar{h}_o)^2}}. \quad (24)$$

In which h_{oi}^t , h_{si}^t , and \bar{h}_o denote the observed head, simulated head, and mean value for observed head, respectively, n denotes the number of observational wells, and m denotes the number of monthly time stages (i ranges from 1 to 11 months, while t ranges from 1 to 12 months). The optimization model's decision variables are dependent on the number of the aquifer discharge volumes (33999 wells) over 12 months. The three objective functions employed in this analysis are mentioned below. Minimizing the amount of shortage was considered as the first objective function [30]:

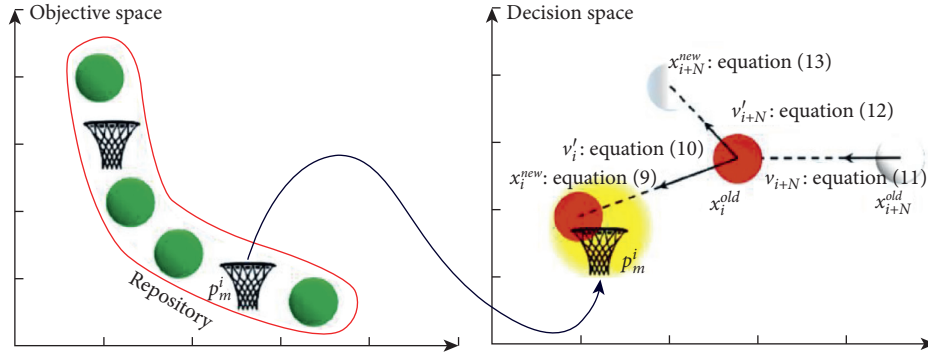


FIGURE 8: The procedure of updating a pair of balls [18].

$$\text{MIN} \left\{ \text{shortage} = \sum_{i=1}^n (TD_t - TW_t) \right\}. \quad (25)$$

In which, TW_t denotes the aquifer discharge volume in the time span t (MCM), TD_t denotes the demand volume in the time period t (MCM), and n determines the cumulative number months. An MSI (equation (26)) was selected as the second objective function because it simply minimizes the total of shortages over time and avoids the spread of shortages over time. This index is critical for developing economic and social strategies [31]:

$$\text{MIN} \left\{ \text{MSI} = \frac{100}{n} \sum_{i=1}^n \left(\frac{TS_t}{TD_t} \right)^2 \right\}. \quad (26)$$

In which, TS_t and TD_t represent the amount of shortage and demand in period t , respectively. In addition, n indicates the total number months. It is worth noting that drinking demand is calculated by subtracting the shortfall volume of other needs (such as agricultural and industrial) from discharge values. Finally, the third objective function was to minimize the drawdown of water-table level [32]:

$$\text{MIN} \{ \text{Drawdown} = \bar{H}_0 - \bar{H}_{\text{end}} \}, \quad (27)$$

In which, \bar{H}_0 and \bar{H}_{end} are the mean aquifer water levels (meters) at the start and end of the simulation time, correspondingly.

3. Discussion and Results

3.1. Optimizing Parameters Using the HHO Algorithm. Over 5,000 simulation runs, the HHO model was optimized, with the model achieving the convergence condition after around 3,000 iterations. For each zone, the specific yield and hydraulic conductivity of groundwater were then optimized. Figures 9 and 10 depict optimal hydraulic conductivity (k) and specific yield (S_y) values for geological units. The aquifer's hydraulic conductivity and specific yield varies significantly, indicating a geologically nonhomogeneous groundwater system. The corresponding hydraulic conductivity field is greatest in blue-coloured zone and lowest in red-coloured one (Figure 11). It means that the central to the north western parts of the aquifer have the lowest hydraulic conductivity. Only two spots (i.e., blue spots) have the

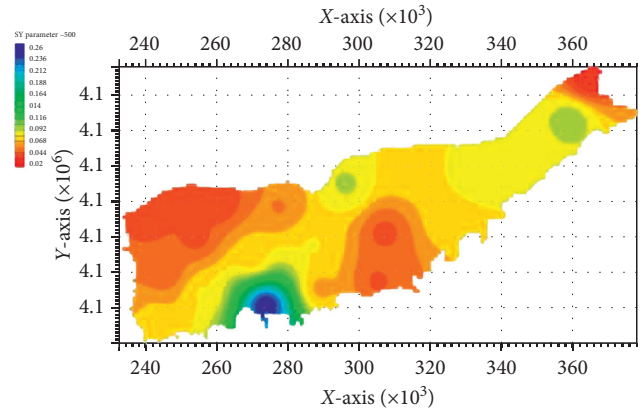


FIGURE 9: Specific yield pattern resulted in MODFLOW modelling.

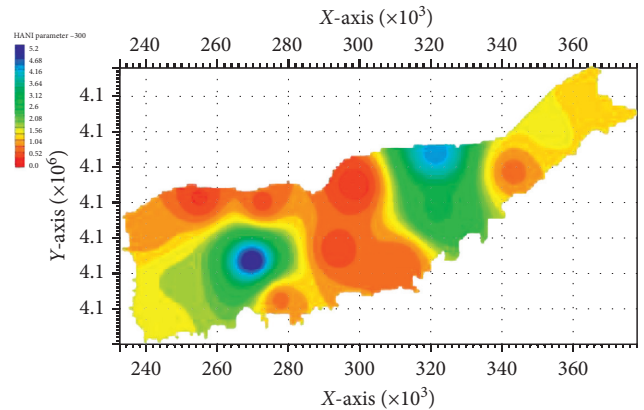


FIGURE 10: Hydraulic conductivity pattern resulted in MODFLOW modelling.

highest amount of hydraulic conductivity. In other words, the eastern parts of the Gorgan Plain aquifer have higher amount of hydraulic conductivity. As a matter of fact, this is due to the heterogeneity spread all over the aquifer. Although, due to the sever nonhomogeneity of the Gorgan Plain aquifer, the interpretation of hydraulic conductivity all over the study area is difficult, discussion about the specific yield can be more convenient. As it is obvious from Figure 9, the specific yield amount reduces to the northwest and northeast. Its highest amount located in the south with the

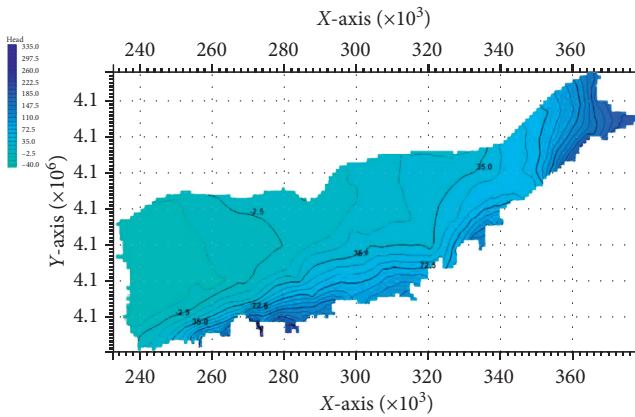


FIGURE 11: Groundwater water-table levels at the start of the simulation phase.

blue colour as the blue spot. It means that the spreading pattern of specific yield would be concordant to the aquifer's hydraulic conductivity except for the blue and green spots toward the east. Therefore, the before mentioned heterogeneities can be the main cause of this variation pattern.

High hydraulic conductivity regions can be permanently limited to the groundwater regime to modify aquifer properties. Considering the broad range of variations in both parameters across the entire aquifer, it seems that the aquifer's hydraulic reaction to recharging and pumping operations is extremely volatile. To put it another way, there cannot be a steady-state pattern in the groundwater regime. The vertical range of the aquifer can be further disrupted by variations in hydraulic conductivity (hydraulic conductivity multiplied by saturated aquifer thickness). Hydraulic characteristics or other elements that have a significant positive or negative influence on groundwater modelling are of higher importance in the modelling [8]. The specific yield ranges between 0.02 and 0.2. In general, variations in specific yields can cause fluctuations in the aquifer's hydraulic response to transient stress. This instability represents the groundwater regime's extremely nonlinear characteristics.

After simulating each time, the mflab software was slightly changed to display the volumetric specific yield. The specific yield values were separated by the research area to get equal water thicknesses. A variety of MATLAB commands were developed in this study to facilitate algorithmic runs and produce MODFLOW input files. All of the tests were performed on a PC using an Intel Core i7, 7700HQ CPU running at 2.8 GHz to 2.81 GHz and 12 GB of RAM. Depending on the algorithm setup, the overall running time was about 37 minutes that was much faster than using the internal optimization method supplied in MODFLOW software (i.e., Newton-Raphson optimization subfunction).

3.2. HHO Calibration and Validation Results. During the calibration process, aquifer water-table level was simulated across 30 zones, as seen in Figures 9 and 10. Using 12-month tension data from October 2019 to September 2020, the model was validated by predicting observed water-table level

(each cycle includes three ten-day time scales). The contribution of different locations within the model domain to the estimated value of the particular parameter being measured is represented by the estimated values in distinct zones for a specific groundwater parameter. Table 1 shows and reports the error indices for simulated and observed head values. The error calculation indicates that the model is well calibrated. The calculated error is also low during the validation process, suggesting a good calibration. The MODFLOW simulation's validity and the HHO's efficiency in computing groundwater properties are also verified by the model calibration and validation results. Any ambiguity, such as measurement error, specified initial and boundary conditions, or the overall conceptual model, has a significant influence on modelling. Although Hamraz et al. [3] examined the parameter uncertainty associated in identifying the recharging ground water parameters; the emphasis of our study is on optimization approaches (by reducing error and misfit). According to the error indices, the HHO significantly decreased error and misfit by indicating the lowest error throughout the calibration and validation phases as well as reducing the CPU time. The HHO algorithm yielded RMSE and NRMSE in the ranges of 0.7–0.9 m and 0.02–0.025, respectively (Table 1).

The HHO approach discussed here will afford modellers with a simple technique that can be applied to complicated activities. As shown in Figures 10 and 12, the groundwater water-table levels were calculated at the start and end of the simulation phase for the whole aquifer.

The head values reveal a distinct pattern when comparing groundwater water-table levels. The effects of local pumping operations (drinking or agricultural wells) at the start of the simulation phase (which starts in October) and the subsequent restoration of flow can be used to explain this phenomenon (mostly by neighbouring aquifers). These aggressive pumping operations might smooth out the design of the simulated head curve at the aquifer's centre. In other words, the values at the cell or grid's centre are reflected in the simulated groundwater level, and piezometers are frequently found there. The aquifer's groundwater level decreased from south to north and northwest, as seen in Figures 12 and 13, indicating that groundwater flow is largely in the same route. We can see from Figures 12 and 13 that if present withdrawals continue, groundwater levels in the west would almost certainly decline. In addition, the groundwater gradient decreases from south to north (and east to west in the eastern parts). This is due to the flow direction which is concordant to the groundwater gradient.

3.3. Pumping Rate Optimization. The optimized parameters collected by the HHO optimization algorithm were used to optimize predefined objective functions in MOBOA (5,000 iterations). Three policy analysis possibilities are examined to analyze the influence of different fundamental assumptions on the results. Scenario A: under this situation, the highest pumping rate is considered with reducing the sum of shortages while having the aquifer water-table drops maximally. Scenario B: in this situation, pumping rates are

TABLE 1: Performance criteria of the HHO algorithm in calibration/validation phases.

Phase	MAE	RMSE	ME	NRMSE
Calibration	0.49	0.71	0.18	0.019
Validation	0.65	0.85	0.33	0.024

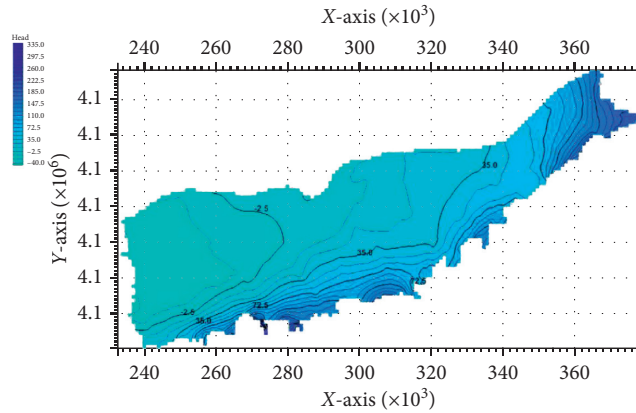


FIGURE 12: Groundwater levels at the end of the simulation phase.

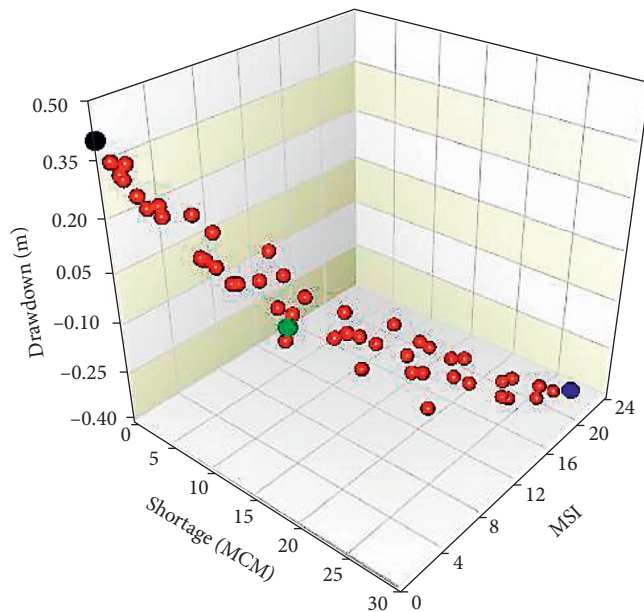


FIGURE 13: Pareto-optimum solution using the three objective functions values (i.e., drawdown, shortage, and MSI).

permitted to supply demand with no drop in aquifer water-table level and no volatility in the aquifer water table at the start and end of the year (October to September). Scenario C: pumping rates are expected to be the minimum values in order to minimize drawdown and raise the aquifer water level at the start and end of the period. Therefore, the MOBOA was optimized using 12-month discharge values as decision parameters according to the predetermined objective functions (Scenarios A, B, and C) as the alternative optimum approaches situated in separate areas of the Pareto solutions.

So, the MODFLOW framework is used to simulate and explain optimum solutions. Figure 13 depicts the Pareto-optimal solution using the three predefined objective functions values (i.e., drawdown, shortage, and MSI). As the distribution of shortages in different months is defined by MSI values, it (i.e., MSI) is considered to decline while shortage amounts reduce, and the drawdown amounts increase. Therefore, as drawdown increases, the shortage amount decreases, until all needs are supplied with no shortage when drawdown reaches 0.4 meter. Furthermore, 2D Pareto fronts (two objective functions) were evaluated to a better explanation and to analyze the best solutions (Figure 14). Drawdown and shortage are inversely related; because of the decreasing trend in the aquifer, discharge causes a drop in drawdown, as seen in Figure 14(a). The relation between shortage and drawdown is nearly linear, and it might be explained by the same amount for aquifer hydrodynamic characteristics at different flow depths. MSI has a straight association with shortage. As a result, MSI is projected to be inversely proportional to drawdown amounts (Figure 14(b)).

The total of optimum discharge amounts across the simulation time is shown as the decision variables for the three samples of optimum solution from various regions of the Pareto front. Therefore, the black, green, and blue dots in Figures 13 and 14, respectively, show the solutions A, B, and C.

According to Figures 13 and 14, if the first scenario (A) is considered, the total amount of shortages will be reduced and the aquifer will experience high values of drawdown. It will be accompanied by the total amount of MSI reduction as the highest pumping rate applied to the aquifer. It is well-known if Scenario C is considered, the aquifer water level rises upward due to declination in drawdown amount. This situation will not be obtained unless the aquifer pumping rates are expected to be at the minimum values.

Based on Scenario B, there will be no drop and instability in aquifer water level due to permitting the pumping rates to supply demands at the start and end of the year.

Figure 14 determines the solutions A and C that express zero, and 27.3 MCM shortages are decided to supply the first and third objective functions so as to minimize the sum of shortages and drawdown, respectively. The best solution would be one that all three objective functions contribute equally to the optimization procedure. The ideal solution is represented by the green point as solution B, when shortage and MSI are nearly zero. According to Figure 14, when drawdown is near 0.4 m, the aquifer can meet all demands. Moreover, in Scenario B, the pumping rate at existing wells is allowed to fluctuate over time (but not the water-table depth at the start and end of the period), resulting in a more arrangement that can respond to possible changes such as water needs or periodic recharges. Every value in the nondominated collections acquired for all options represents a distinct strategy that must be weighed against the others when making management choices. These options contrast from groundwater management viewpoints, which hold that no improvement can be made to one goal without decreasing satisfaction with the others. Figure 15 shows the

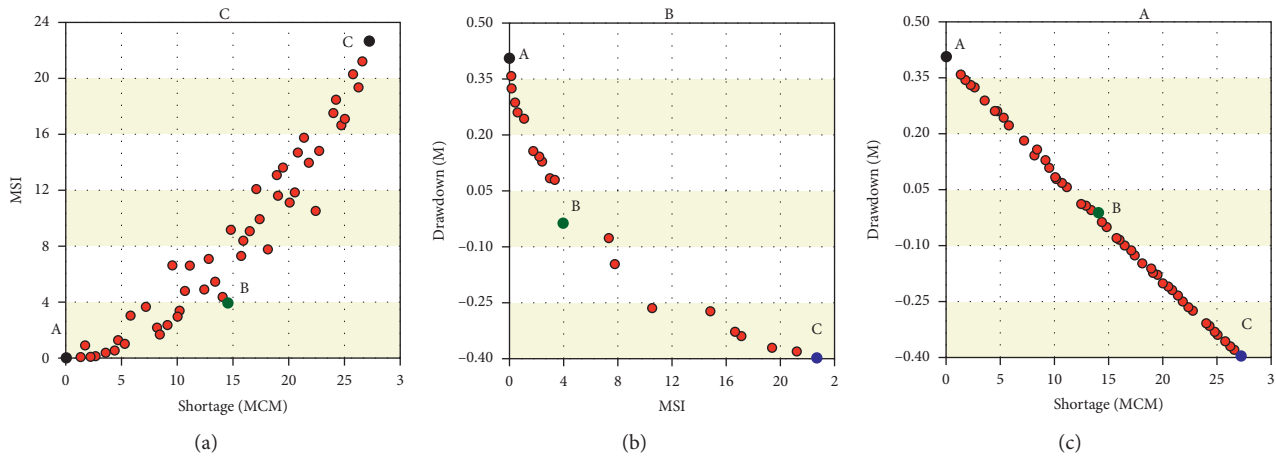


FIGURE 14: Mutual relationships of Pareto fronts in a two-dimensional model. (a) Drawdown (m) versus shortage (MCM); (b) drawdown (m) versus MSI; and (c) MSI vs shortage (MCM).

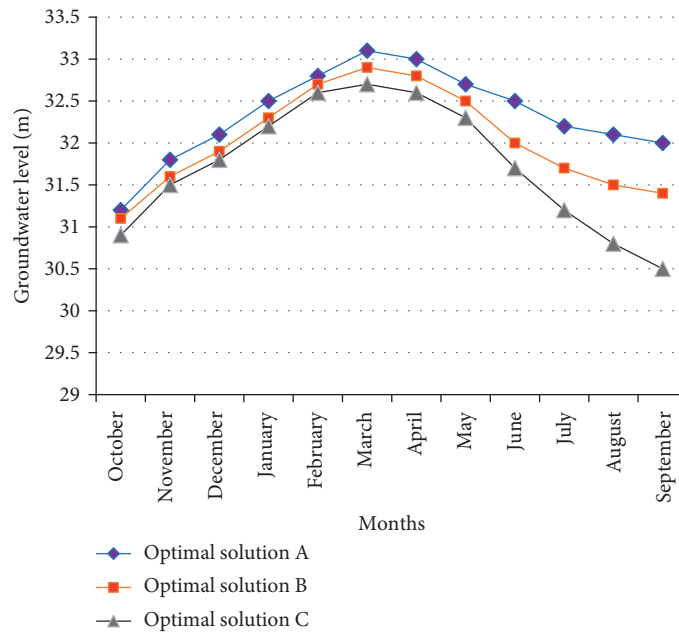


FIGURE 15: Groundwater level variations for all scenarios across the simulation period.

amount of water-table level variations for the three chosen solutions across the simulation period. During February, these three best solutions are fairly near, but they are far apart in September.

February is an appropriate month since demand and drawdown are almost equal or have minimal variations. Although, throughout the spring and summer, once the aquifer water level drops steadily according to numerous pumping operations, the aquifer recovers significantly from October to February. The aquifer’s water-table level ranges from 32.6 to 32.8 meters in February but drops to 30.5 meters in September as the aquifer maximum discharge. During various options, the minimum and maximum limits of groundwater levels were 30.5 m and 32.9 m, respectively, according to the evaluation of all optimum solutions (Figure 15). As decision makers have three ideal alternatives for

the Gorgan Plain aquifer based on the findings, they can choose any (drawdown) option that is within the ideal range of -40 to $+40$ cm/year. During maximum and minimum drawdown amounts over the aquifer, there are considerable changes in water-table levels. If one of the optimum management strategies, A, B, or C, is selected, it should be assured that the area’s maximum needs are satisfied. However, the challenge of deciding the best option stays open and may vary over time, based on management policies. It is worth noting that optimum solution B, as a transitional scenario, performed well in terms of decreasing the objective functions under consideration in this research. It demonstrates that the created technique was able to converge on an intermediate solution for the case study. Furthermore, optimal solution B could meet the supplying demand fairly while also reducing decline in the aquifer system.

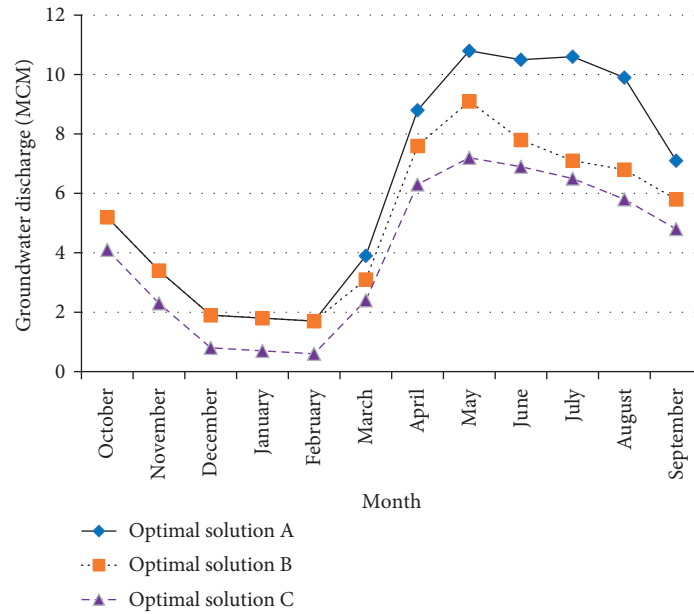


FIGURE 16: Groundwater discharge for all scenarios across the simulation period.

The Pareto front's optimal solution performances suggest that the assistances of the 281 wells might meet the requirements and quality standards. The best contributions produced the highest (+40 centimetres) and lowest (-40 centimetres) drawdown in the 281 wells at the end of the optimization phase. Figure 16 determines that the agricultural demand for water is the primary cause of water level fluctuations in the Gorgan Plain aquifer. In addition, the summer agricultural demand for water has been highlighted as the main discharge water.

It should be mentioned that the results of this research are in line with the Sadeghi-Tabas et al. [19] research. In other words, the results obtained in this study are similar to their study results.

4. Conclusion

In this research, the HHO method was used to optimize the estimation of MODFLOW hydrodynamic parameters, and the optimized parameters were then utilized in the MOBOA multiobjective algorithm to construct Pareto-optimum approaches and groundwater-managing scenarios. The suggested multiobjective problem design included reducing the shortage caused by a supply failure, MSI, and reducing the amount of drawdown within predefined zones within three alternatives as Scenarios A, B, and C. Under Scenario A, the total amount of shortages will be reduced and the aquifer will experience high values of drawdown. In addition, it will be accompanied by the total amount of MSI reduction as the highest pumping rate applied to the aquifer. However, if Scenario C is considered, the aquifer water level rises upward due to declination in drawdown amount. This situation will not be obtained unless the aquifer pumping rates are expected to be at the minimum values. Moreover, in Scenario B, there will be no drop and instability in aquifer water level due to permitting the pumping rates to supply demands at

the start and end of the year. The results determined that considering the Scenarios A and C expresses zero and 27.3 MCM shortages, in order to supply the first and third objective functions so as to minimize the sum of shortages and drawdown, respectively. And the best solution would be one that all three objective functions contribute equally to the optimization procedure. However, the ideal solution is represented by Scenario B, when shortage and MSI are nearly zero. It is worth noting that, when drawdown is near 0.4 m, the aquifer can meet all demands. Moreover, in Scenario B, the pumping rate at existing wells is allowed to fluctuate over time (but not the water-table depth at the start and end of the period), resulting in a more arrangement that can respond to possible changes such as water needs or periodic recharges. In addition, the groundwater level variations for the three scenarios across the simulation period indicated that during February, these three best solutions are fairly near, but they are far apart in September. The aquifer's water-table level also ranges from 32.6 to 32.8 meters in February but drops to 30.5 meters in September as the aquifer maximum discharge. During various options, the minimum and maximum limits of groundwater levels were 30.5 m and 32.9 m, respectively, according to the evaluation of all optimum solutions. When two separate algorithms were combined with the MODFLOW model, it was discovered that the created method could produce a set of optimum approaches for the groundwater system represented on a Pareto front. It should be noted that using the HHO algorithm as a new optimization method instead of the traditional optimization method supplied in the MODFLOW model makes the MODFLOW software more applicable and much faster in groundwater modelling by shortening the CPU time of the computers up to 37 minutes running time. Therefore, this research calculated optimal solutions for the whole aquifer of the Gorgan Plain, evaluating those approaches for each groundwater zone might

give important data for the groundwater-managing policies. Although both the HHO and MOBOA algorithms are effective in quantifying groundwater features, the computation time for a broader aquifer system may grow considerably as the number of cells and stress periods rise. Therefore, the idea of fuzzy set theory [33] or using multiprocessor computers [34] can also be utilized to evaluate each of the efficient approaches to optimize objective functions depending on objective conditions. The HHO-MOBOA method described in this research can be regarded as an optimum solution producer, and its connection to the MODFLOW framework allows for the simulation of optimum groundwater scenarios that can be readily combined with the other conceptual models such as hydrology and water quality models. The integration of the optimization capabilities of HHO and MOBOA to the MODFLOW environment created a more applicable looping “Simulation-Optimization-Modelling” method valuable for decision makers dealing with groundwater management issues in the arid to semiarid regions.

Data Availability

The data used to support the findings of this study are available from the corresponding author upon request, e-mail address: sarraf@riau.ac.ir.

Conflicts of Interest

The authors declare that there are no conflicts of interest regarding the publication of this paper.

Acknowledgments

The authors are grateful to Dr. Alireza Donyaii for his kind recommendations. He is one of the best scientists in water resources managing in the Golestan Regional Water Company, Gorgan, Iran.

References

- [1] A. R. Donyaii and A. P. Sarraf, “Optimization of reservoir operation using a bioinspired metaheuristic based on the COVID-19 propagation model,” *Numerical Methods in Civil Engineering*, vol. 5, no. 1, pp. 15–28, 2020.
- [2] A. Donyaii, A. Sarraf, and H. Ahmadi, “Water reservoir multiobjective optimal operation using grey wolf optimizer,” *Shock and Vibration*, vol. 2020, Article ID 8870464, 10 pages, 2020.
- [3] B. Hamraz, A. Akbarpour, M. P. Bilondi, and S. S. Tabas, “On the assessment of ground water parameter uncertainty over an arid aquifer,” *Arabian Journal of Geosciences*, vol. 8, no. 12, pp. 10759–10773, 2015.
- [4] S. Afkhamifar and A. P. Sarraf, “Prediction of groundwater level in Urmia plain aquifer using hybrid model of wavelet transform-extreme learning machine based on quantum particle swarm optimization,” *Water Engineering and Management*, vol. 12, no. 2, pp. 351–364, 2020, in Persian.
- [5] O. Giustolisi and V. Simeone, “Optimal design of artificial neural networks by a multi-objective strategy: groundwater level predictions,” *Hydrological Sciences Journal*, vol. 51, no. 3, pp. 502–523, 2006.
- [6] S. Afkhamifar and A. P. Sarraf, “Comparative study of groundwater level forecasts using hybrid neural network models,” *Proceedings of the Institution of Civil Engineers–Water Management*, 2021.
- [7] A. Donyaii, A. Sarraf, and H. Ahmadi, “A novel approach to supply the water reservoir demand based on a hybrid whale optimization algorithm,” *Shock and Vibration*, vol. 2020, Article ID 8833866, 15 pages, 2020.
- [8] A. R. Donyaii, A. P. Sarraf, and H. Ahmadi, “Comparison of meta-heuristic algorithms in optimum operation of a single-reservoir dam system,” *Proceedings of the Institution of Civil Engineers–Engineering Sustainability*, 2021.
- [9] H. V. Gupta, S. Sorooshian, and P. O. Yapo, “Toward improved calibration of hydrologic models: multiple and non-commensurable measures of information,” *Water Resources Research*, vol. 34, no. 4, pp. 751–763, 1998.
- [10] P. O. Yapo, H. V. Gupta, and S. Sorooshian, “Multi-objective global optimization for hydrologic models,” *Journal of Hydrology*, vol. 204, no. 1, pp. 83–97, 1998.
- [11] D. P. Boyle, H. V. Gupta, and S. Sorooshian, “Toward improved calibration of hydrologic models: combining the strengths of manual and automatic methods,” *Water Resources Research*, vol. 36, no. 12, pp. 3663–3674, 2000.
- [12] H. A. El-Ghandour and A. Elsaid, “Groundwater management using a new coupled model of flow analytical solution and particle swarm optimization,” *International Journal of Water Resources and Environmental Engineering*, vol. 5, no. 1, pp. 1–11, 2013.
- [13] A. R. Donyaii, A. P. Sarraf, and H. Ahmadi, “Evaluation of whale, fruit fly and cuckoo search algorithms in optimizing multi-objective operation of golestan dam reservoir based on multi-criteria decision-making method,” *Water Resources Engineering*, vol. 13, no. 47, pp. 85–100, 2020.
- [14] C. H. Park and M. M. Aral, “Multi-objective optimization of pumping rates and well placement in coastal aquifers,” *Journal of Hydrology*, vol. 290, no. 1, pp. 80–99, 2004.
- [15] P. Reed, B. S. Minsker, and D. E. Goldberg, “A multiobjective approach to cost effective long-term groundwater monitoring using an elitist nondominated sorted genetic algorithm with historical data,” *Journal of Hydroinformatics*, vol. 3, no. 2, pp. 71–89, 2001.
- [16] T. Siegfried, S. Bleuler, M. Laumanns, E. Zitzler, and W. Kinzelbach, “Multiobjective groundwater management using evolutionary algorithms,” *IEEE Transactions on Evolutionary Computation*, vol. 13, no. 2, pp. 229–242, 2009.
- [17] T. A. Saafan, S. H. Moharram, M. I. Gad, and S. A. KhalafAllah, “multi-objective optimization approach to groundwater management using genetic algorithm,” *International Journal of Water Resources and Environmental Engineering*, vol. 3, no. 7, pp. 139–149, 2011.
- [18] A. Kaveh, M. Khanzadi, and M. Rastegar Moghaddam, “Billiards-inspired optimization algorithm; a new metaheuristic method,” *Structure*, vol. 27, no. 3, pp. 1722–1739, 2020.
- [19] S. Sadeghi-Tabas, S. Z. Samadi, A. Akbarpour, and M. Pourreza-Bilondi, “Sustainable groundwater modeling using single- and multi-objective optimization algorithms,” *Journal of Hydroinformatics*, vol. 11, no. 1, pp. 12–39, 2016.
- [20] M. Abdel-Basset, W. Ding, and D. El-Shahat, “A hybrid Harris Hawks optimization algorithm with simulated annealing for feature selection,” *Artificial Intelligence Review*, vol. 54, no. 3, pp. 593–637, 2020.

- [21] A. Donyaii and A. Sarraf, "Evaluation of hydro-climatic conditions of gorganroud catchment under the effect of climate change using MIROC-ESM model," *Hydrogeomorphology*, vol. 7, no. 25, pp. 204–183, 2021.
- [22] J. Dupuit, *EstudesTheoriques et Pratiques sur le MouvementdesEaux*, Dunod, Paris, France, 1863.
- [23] R. Rojas, L. Feyen, and A. Dassargues, "Conceptual model uncertainty in groundwater modeling: combining generalized likelihood uncertainty estimation and Bayesian model averaging," *Water Resources Research*, vol. 44, no. 12, pp. 1–16, 2008.
- [24] A. Izady, K. Davary, A. Alizadeh et al., "A framework toward developing a groundwater conceptual model," *Arabian Journal of Geosciences*, vol. 7, pp. 3611–3631, 2014.
- [25] S. L. Lim, *Social networks and collaborative filtering for large-scale requirements elicitation*, Ph.D. Dissertation, University of New South Wales, Sydney, Australia, 2011.
- [26] T. N. Olsthoorn, "mflab: environment for MODFLOW suite groundwater modeling," 2013, <http://code.google.com/p/mflab>.
- [27] D. N. Moriasi, J. G. Arnold, M. W. Van Liew, R. L. Bingner, R. D. Harmel, and T. L. Veith, "Model evaluation guidelines for systematic quantification of accuracy in watershed simulations," *Transactions of the ASABE*, vol. 50, no. 3, pp. 885–900, 2007.
- [28] H. Etemadi, S. Samadi, and M. Sharifikia, "Uncertainty analysis of statistical downscaling models using general circulation model over an international wetland," *Climate Dynamics*, vol. 42, pp. 2899–2920, 2014.
- [29] H. Etemadi, S. Samadi, M. Sharifikia, and J. M. Smoak, "Stationary an arid coastal region of southern Iran," *Theoretical and Applied Climatology*, vol. 126, no. 1, pp. 1–15, 2015.
- [30] N.-S. Hsu and K. W. Cheng, "Network flow optimization model for basin-scale water supply planning," *Journal of Water Resources Planning and Management*, vol. 128, no. 2, pp. 102–112, 2002.
- [31] F.-J. Chang, L. Chen, and L.-C. Chang, "Optimizing the reservoir operating rule curves by genetic algorithms," *Hydrological Processes*, vol. 19, no. 11, pp. 2277–2289, 2005.
- [32] M.-Y. Tu, N.-S. Hsu, F. T.-C. Tsai, and W. W.-G. Yeh, "Optimization of hedging rules for reservoir operations," *Journal of Water Resources Planning and Management*, vol. 134, no. 1, pp. 3–13, 2008.
- [33] L. A. Zadeh, "Fuzzy sets," *Information and Control*, vol. 8, no. 3, pp. 338–353, 1965.
- [34] S. Shadpoor, A. Pirouzi, H. Hamze, and D. Mazaheri, "Determination of Bodenstein number and axial dispersion of a triangular external loop airlift reactor," *Chemical Engineering Research and Design*, vol. 165, pp. 61–68, 2021.